SUPERCONDUCTING TRANSITION EDGE BOLOMETERS

by

MICHAEL SIDNEY FRANCIS DUNN

Department of Physics

Queen Mary College

A thesis submitted in accordance with the regulations

for the degree of Doctor of Philosophy

in the University of London

1981

CONTENTS

ABSTRACT

This report describes the development of a servo-controlled superconducting transition edge bolometer (STEB) intended for use as a sensitive broadband far infra-red (FIR), i.e. ≃ 1 mm to 100 μm wavelength, detector.

A STEB uses a constant current biased superconducting film held on its superconducting transition, where it has a very high temperature coefficient of resistance, as a temperature sensing element for the absorbing substrate. Radiation absorbed by the substrate can be detected by measuring the change in voltage across the superconductor. The STEB's described in this thesis have in addition a resistive heater mounted on the substrate which is used as part of a servo-regulating system maintaining the temperature of the bolometer at a fixed point on the superconducting transition. The potential advantages of this arrangement are higher frequency response, greater dynamic range, improved linearity and a STEB which can be more easily held on the superconducting transition. The STEB's described in this thesis used Sn films mounted on sapphire substrates as temperature sensors.

Following a general introduction and review of previous work, the principles of operation of the servo system are described together with the theory of the system response, noise and the radiation performance of the detector. A detailed description is given of the construction of the bolometer, the bolometer optics, cryogenic apparatus and the servo circuitry. Optimisation of the absorption of radiation by the bolometer substrate is studied using a transmission line analogue model. Experiments establishing the validity of the model are also included.

The measured performance of the constructed STEB's is given and compared with theoretical predictions. The measured noise performance was found to be considerably better than predicted. Finally, suggestions are made for future improvements in detector performance.

CHAPTER I

INTRODUCTION

The purpose of this work was to develop a broadband far infra-red (FIR) radiation, i.e. 1 mm → 100 μm wavelength, detector working on the superconducting transition edge bolometer (STEB) principle with a potential for development into a detector with greater sensitivity than other types of broadband FIR detector currently in use. Applications for such a detector would be in spectroscopy and FIR astronomy. High sensitivity is required for use in low background temperature observations, e.g. satellite-borne experiments, where the detection system is liable to be limited by detector noise rather than phonon noise from the relatively high temperature background seen at ground level. The work was supported by an SRC CASE award, the industrial co-sponsor being QMC Instruments Ltd.

The most commonly used FIR detectors are ^{4}He-cooled bolometers using semiconductors as the temperature sensing elements. At the time of writing, the best of these detectors have achieved electrical noise equivalent powers (NEP's) of 3×10^{-15} $W.Hz^{-\frac{1}{2}}(1)$ for ^{4}He-cooled and 6×10^{-16} $W.Hz^{-\frac{1}{2}}(1)$ for ^{3}He-cooled detectors. Only STEB's using ^{4}He cooling were produced for this thesis.

1.1 Basic principles

The bolometer element consists of an absorbing substrate on which is mounted a temperature sensing element and a resistive heater. The heater is a Bismuth (Bi) film of suitable impedance. A sapphire substrate is used to give a low thermal capacity element. Electrical and thermal connection to the bolometer mount is made using thin

nylon leads (for low thermal conduction) coated with a metal film (to provide electrical conduction). The temperature sensing element is a Tin (Sn) film which goes superconducting at $\simeq 3.7^{o}K$. Sn was chosen for the temperature sensor as it has a superconducting transition temperature which is easily reached by a pumped ^{4}He cryostat. However it is advantageous to use a superconducting film with as low a transition temperature as possible, because, as will be shown in Chapter II, the lower the operating temperature, the better the performance of the bolometer.

At the superconducting transition, the resistance of the Sn film disappears completely over a very narrow range of temperature (see Figure (1.1)). Hence it has a very high temperature coefficient of resistance in this temperature range, making it very suitable for use as a temperature sensor. The Sn thermometer is placed in one arm of a Wheatstone bridge. In the quiescent (no signal) conditions, the temperature of the element is maintained such that there is no out of balance signal across the bridge. Changes in temperature of the bolometer element therefore generate an out of balance signal. This signal is amplified and then fed into a phase sensitive detector (p.s.d.) producing an error voltage which regulates the d.c. current passing through the substrate heater. The temperature of the element is thus maintained so that the Sn thermometer is held at a particular point on the superconducting transition and changes in absorbed radiation power result in compensating changes in power supplied by the heater. Hence the change in heater power is a direct measure of the radiation power from the source.

The advantages of using a servo-controlled STEB are:-

(1) a more linear response

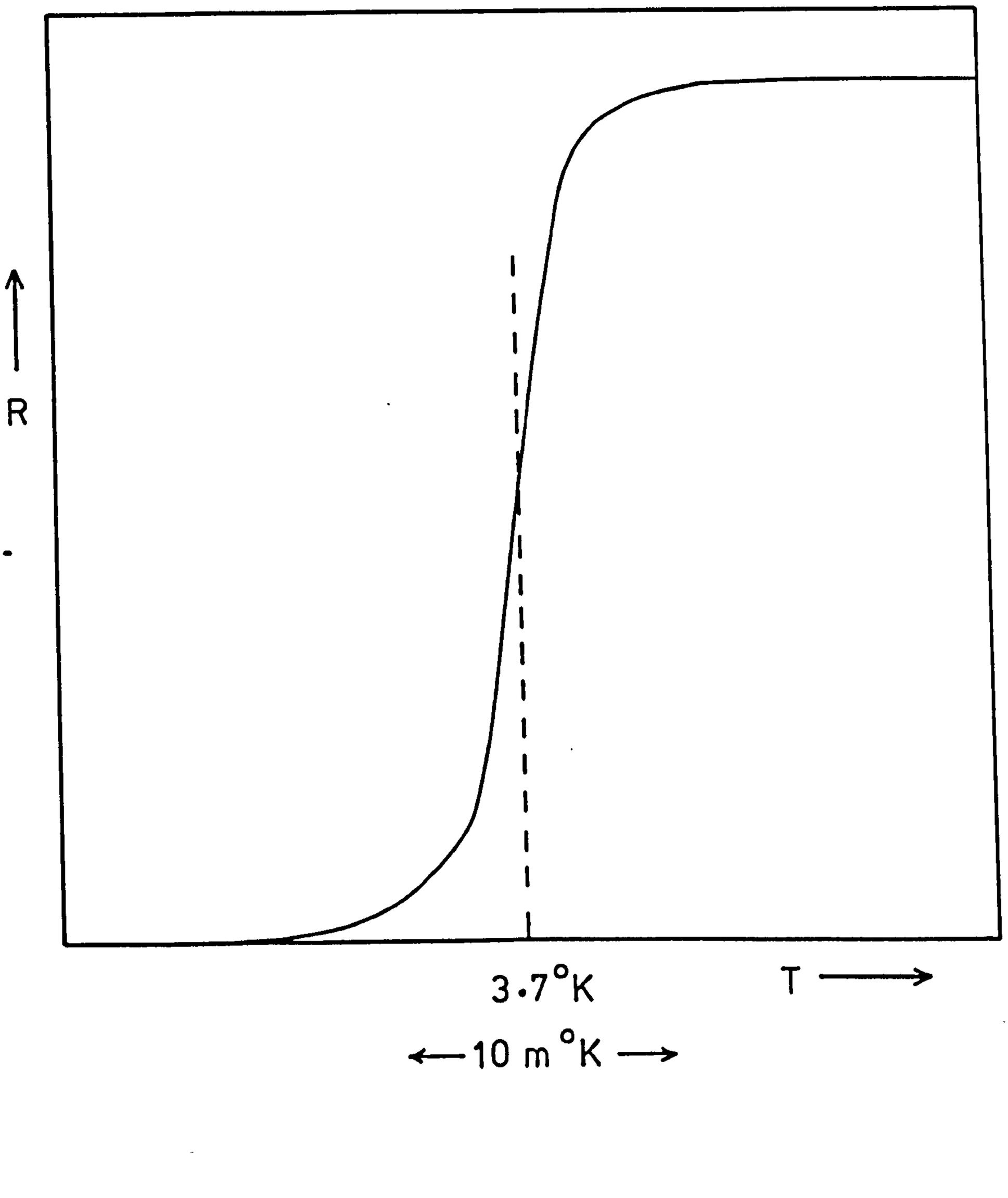

Figure 1.1. R-T characteristic of an Sn film at the superconducting transition.

(2) greater dynamic range

(3) better frequency response

(4) the operating point of the detector is unaffected by heat sink temperature drifts.

1.2 Bolometer theory

For a bolometer at temperature T, connected to a heat sink via a thermal conductance G, the responsivity r is given by (see Chapter II)

$$r = \frac{dV}{dP_r} = \frac{\alpha \beta V_D}{G_e (1+\omega^2 \tau_B^2)^{\frac{1}{2}}} \quad V.W^{-1} \qquad \ldots (1.1)$$

where α = fraction of incident power absorbed,

P_r = radiation signal power incident on the bolometer,

$\beta = \frac{1}{R_{Sn}} \frac{dR_{Sn}}{dT}$ = temperature coefficient of resistance of the temperature sensing element,

V_D = standing bias voltage across the Sn thermometer,

G_e = effective thermal conductance = $G - \beta W_D$ where W_D is the quiescent power developed in the bolometer due to the bias current through the temperature sensing element and G is the thermal conductance between the bolometer and the heat sink,

$\tau_B = C/G_e$ = effective time constant of the bolometer element

where C = element thermal capacity,

$\omega = 2\pi$ x chopping frequency of the incoming radiation signal.

From the above it will be seen that the smaller the thermal conductance G the higher the responsivity of the element. Also one of the fundamental noise limits of the detector, the phonon noise (see Chapter II), is proportional to $G_e^{\frac{1}{2}}$. Hence for optimum performance

G should be made as small as possible. Unfortunately as G is made smaller the element time constant τ_B becomes larger and therefore there is a minimum value of G that can be used in practice, this value being smaller the lower the thermal capacity C.

Hence for good performance C and G should be made as small as possible. Operation at He temperatures is essential therefore to achieve optimum performance, as well as making it possible to use a superconductive temperature sensor.

1.3 Previous work

The first practical STEB was produced by Martin and Bloor[2]. This detector did not use a servo mechanism to maintain the element at a fixed operating point. A servo loop was used however to control the temperature of the heat sink on which the bolometer was mounted. This heat sink was connected to the cryostat heat sink through a nylon washer which gave it a time constant of several seconds. Thus the bolometer was protected against drifts in cryostat heat sink temperature but was essentially operated open loop.

To obtain a low C and G for the detector, Martin and Bloor used 15 μm diameter nylon leads coated with Lead (which goes superconducting at ≃ 7.2°K) for the electrical and thermal connection to the heat sink and used a 3 μm thick mica substrate to support an Sn film (the temperature sensor) and a Bi film (a resistive heater element used for calibration purposes only). Electrical and mechanical connections between the leads and the films on the substrate were made using Indium "cold welding".

The detectors gave radiation NEP's of 10^{-12} $W.Hz^{-\frac{1}{2}}$. The performance of the detectors was limited by noise in the valve amplifiers used

to amplify the signal from the element. It was not possible to get over this problem by decreasing the operating frequency and thereby, from Equation (1.1), increasing the element responsivity, making pre-amp noise less significant, because of low frequency current noise produced by the Sn thermometer.

Clarke and Voss[3] have shown that low frequency noise in metal films deposited on dielectric substrates is caused by a thermal diffusion mechanism. Following on from this work, Clarke and Hsiang[4] have shown that the low frequency noise in Sn films at the superconducting transition can be substantially reduced by using a thin Aluminium (Al) film ≈ 100 Å thick as an underlay to improve the thermal coupling between the Sn film and the substrate.

Clarke et al.[5] have produced a STEB using an Al film as the temperature sensor. Al goes superconducting at a temperature somewhat lower than Sn, i.e. ≈ 1.2°K for the pure bulk material. Clarke used a 125 μm thick sapphire substrate and Indium (In) coated 15 μm nylon leads (In goes superconducting at ≈ 3.9°K). A Bi film was evaporated on the back surface of the substrate to increase the coupling efficiency to FIR radiation. The use of an Al thermometer helped to reduce low frequency noise substantially and, together with the very low values of G and C for the bolometer due to the low temperature of operation, enabled detectors with electrical NEP's of 1.7×10^{-15} $W.Hz^{-\frac{1}{2}}$ to be produced. These detectors did not use a servo-regulating mechanism to control the temperature of either the element or the bolometer mount.

This thesis describes an Sn-based STEB using a servo-regulated element where the radiation signal is measured by monitoring the change in servo power fed back to the element. Although the detector

gave a radiation NEP comparable to the best ^{4}He-cooled semiconducting bolometers in use, it is anticipated that further increases in performance could be achieved. Chapter VI describes a number of ways in which this could be attempted.

CHAPTER I

REFERENCES

(1) Nishioka, N.S., P. L. Richards, and D. P. Woody, 2nd International Conference and Winter School on Submillimetre Waves and their Applications, San Juan, Puerto Rico (New York, U.S.A.; I.E.E.E. 1976), pp. 66-7.

(2) Martin, D.H. and D. Bloor, Cryogenics 1, 159 (1961).

(3) Clarke, J. and R. F. Voss, Phys. Rev. Letts. 33, No. 1, 24 (1974).

(4) Clarke, J. and T. Y. Hsiang, Phys. Rev. Letts. 34, No. 19, 1217 (1975).

(5) Clarke, J., Third International Conference on Submillimetre Waves and Their Applications, 29th March - 1st April (1978).

CHAPTER II

BOLOMETER THEORY

2.1 The temperature sensing element and relevant aspects of superconductivity

Sn was chosen as the temperature sensing element because it has a convenient transition temperature (T_c = 3.72°K for the pure bulk material) and sharp normal-superconducting transitions can be obtained without critical attention to evaporation conditions or the need to use mechanical edge-trimming of the films. Nevertheless, for Sn films of the thickness used (≃ 500 Å) the transition width is significantly greater than for the pure bulk material, i.e. of order 10 m°K as opposed to less than 1 m°K for the pure bulk material. The following gives an outline of the reasons for this broadening of the transition:

According to the Pippard theory[1], the width of the transition is dependent upon a coherence length ξ_ℓ. The coherence length depends on the mean free path of the electrons (ℓ) in the following way:

$$\frac{1}{\xi_\ell} = \frac{1}{\xi_o} + \frac{1}{A\ell}$$

where ξ_o is the coherence length of the pure bulk material and A is a constant of order 1. It is therefore seen that, for films where ℓ is comparable to or less than ξ_o, the transition width will be broader than for the pure bulk material. Hence for sharp transitions, ℓ should be as large as possible. [2] gives experimental data showing increasing transition width with decreasing film thickness for Sn films. Additionally, through their effect on ℓ, impurities (structural as well as chemical) will also increase the transition width and consequently care must be taken in the film evaporation to

produce as pure a deposition as possible. [2] mentions that mechanical edge-trimming of Sn films is necessary to reduce the transition width to the minimum possible value for a given deposition.

The other property of the Sn sensor which could have a significant effect on the performance of the bolometer is the superconducting transition temperature T_c. Factors affecting the transition temperature of an Sn film are:

(1) decreasing film thickness gives an initial increase followed by a decrease in T_c [3],

(2) very narrow films (i.e. <1μm width) exhibit a depression in T_c inversely proportional to the width and thickness [4],

(3) decreasing film thickness also produces an increase in T_c due to thickness-dependent critical shear stress caused by thermal strains on cooling to He temperatures [2],

(4) impurity concentration [3].

All these factors have only a small effect on the T_c for the Sn films used as sensing elements in the bolometers, i.e. 100 μm wide, 500 Å thick deposited on sapphire substrates, and the effect on G and C, and therefore the performance of the detector is slight.

2.2 Sensing servo theory

2.2.1 Sensing servo - principles of operation

Physically, the bolometer servo-mechanism acts to keep the total input power to the bolometer element constant, increases in incident signal radiation resulting in decreases in heater power. The servo circuit is shown in Figure (2.1). The Sn sensing element R_{Sn} is placed in one arm of an a.c. Wheatstone bridge. The a.c. bias current to R_{Sn} and the cooled load resistor R_d is supplied by the two equal

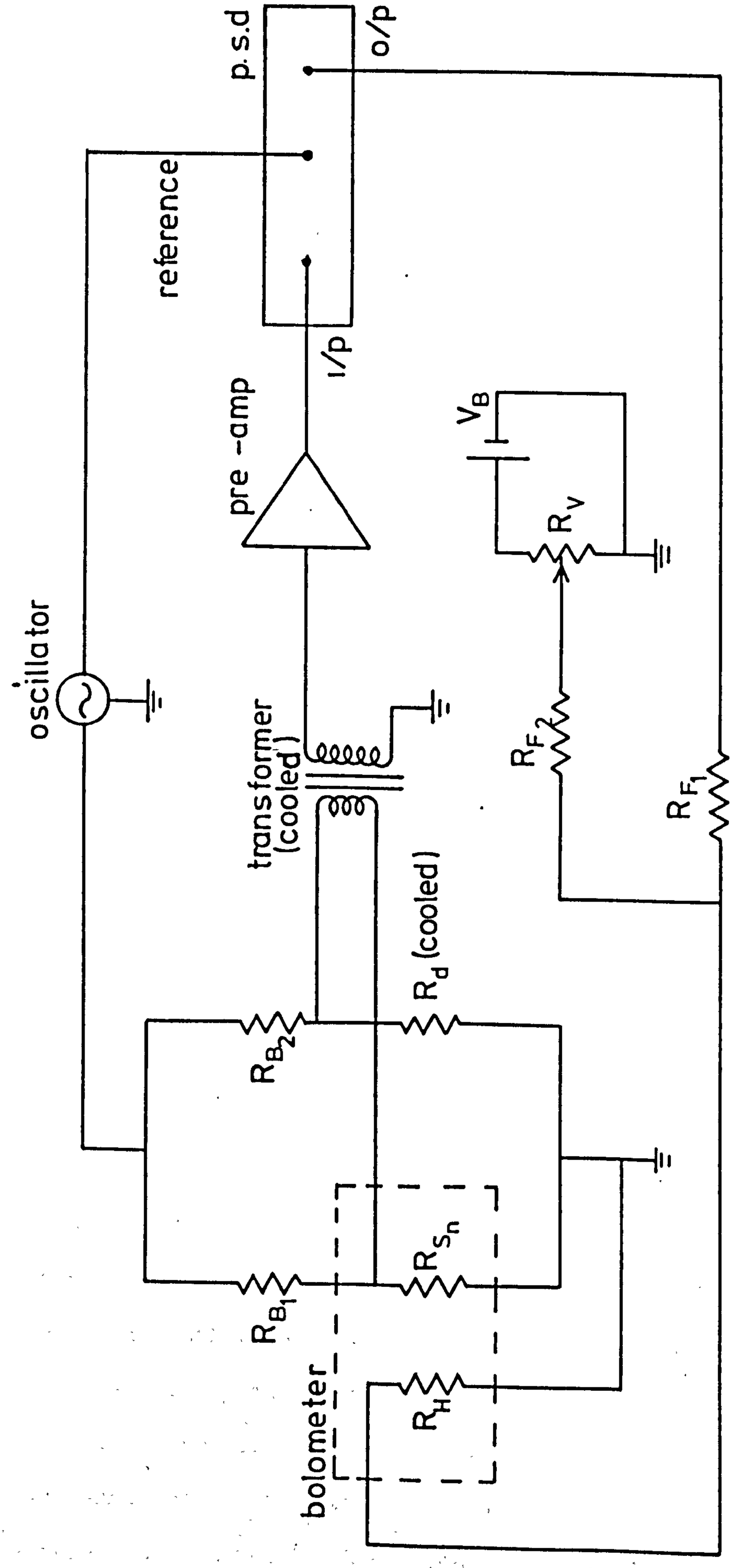

Figure 2.1. Servo circuit.

room temperature load resistors R_{B_1} and R_{B_2}, and the signal oscillator. The output from the bridge is matched into a low noise pre-amp through a cooled transformer. The output from the pre-amp is then amplified and demodulated by the phase sensitive detector (p.s.d.). The p.s.d. output is connected to the element heater R_H through the room temperature feedback resistor R_{F_1}. The p.s.d. is phased so that a change in the temperature of the element producing a change in R_{Sn} results in a compensating adjustment of the p.s.d. output current, and therefore the heater power dissipated in the element until the bridge is again balanced. Hence power inputs to the bolometer from any source, e.g. heat sink temperature drifts or noise, are compensated for by the servo as well as power due to incident signal radiation.

The battery V_B, pot R_V and R_{F_2} provide additional d.c. offset current to the Bi heater. In practice, R_{F_2} is made equal to R_{F_1} so that the voltage across the pot is equivalent to the same voltage added as an offset voltage to the p.s.d. output. The temperature of the heat sink is set less than the bolometer operating temperature by the amount necessary to compensate for the increase in bolometer element temperature produced by the quiescent power dissipated by the heater.

It is appropriate at this point to discuss why it was decided to use a servoed element, i.e. where the temperature of the element is controlled by altering the power dissipated by a Bi film deposited on the element, rather than a servoed bolometer mount, where the temperature of the bolometer is controlled by altering the temperature of the bolometer mount. Using a Bi film deposited directly onto the bolometer substrate to provide feedback power to the bolometer produces a lag in the feedback loop equivalent to the time taken for

the Sn sensor to respond to changes in temperature of the element due to a change in feedback power supplied by the Bi heater. Using a servoed mount to supply the feedback power would result in a time constant being inserted in the feedback loop equivalent to the thermal time constant of the mount and the time constant of the bolometer element. As, in practice, the thermal time constant of the mount and element are liable to be very much greater than the time required for the Sn sensor to respond to power supplied to the bolometer element through the resistive Bi film, then using a servoed element will result in an inherently more stable feedback loop which can be operated at higher open loop gains resulting in superior servo-system frequency response. Additionally, as the thermal mass of the mount will be very much greater than the thermal mass of the element, servoing the temperature of the element will result in much lower power dissipation than servoing the temperature of the mount, helping to reduce the boil-off rate of the cryostat to a minimum.

2.2.2 Signal response

Figure (2.2a) gives a diagram of the functional servo loop and Figure (2.2b) the effective servo loop. Note that $s = \sigma + j\omega$ where ω = angular frequency and σ the damping. The bolometer substrate acts as the feedback differencing element, producing an output temperature change determined by the fraction of the incident signal power absorbed (ΔP) and the heater power produced by the output of the amplifier chain (P_F). The demodulation function d(t) represents the action of the phase sensitive detection. $A_2(s)$ represents the amplification and output time constant setting of the p.s.d. $S_1(f)$, $S_2(f)$ and $S_3(f)$ are noise spectra representing noise generators discussed in Section (2.3).

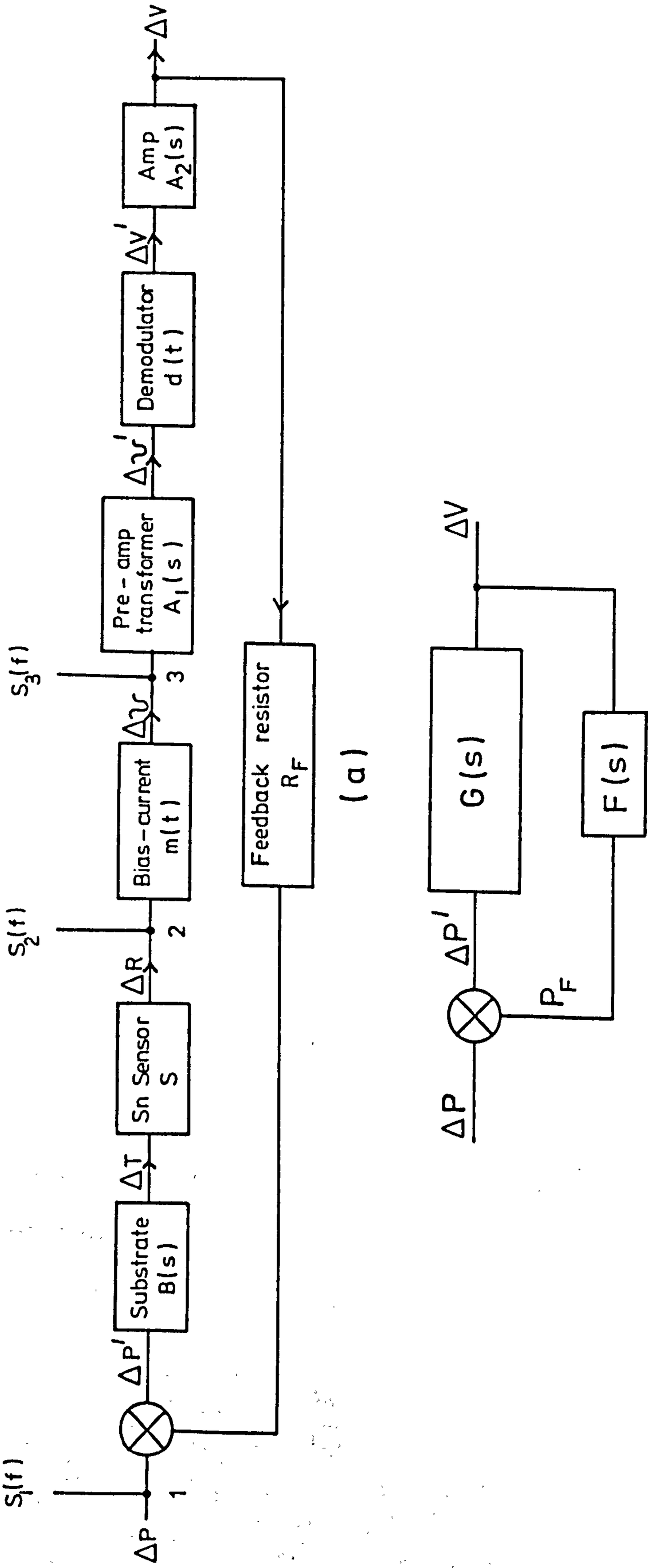

Figure 2.2. (a) Functional servo loop; (b) effective servo loop.

If the bandwidth of $B(s) \cdot A_2(s)$ is much less than the modulation frequency f_o as will be assumed, then (see Appendix I) the time dependent component of the product of m(t) and d(t) can be ignored.

Bolometer

Suppose the bias power dissipated by the Sn sensor is P_B. The total change of power is related to temperature change ΔT by

$$\Delta(P + P_B) = G\ \Delta T$$

where G is the thermal conductance to the heat sink and P is the radiation power input to the bolometer. But

$$\Delta P_B = i_B^{\,2}\ \Delta R_{Sn}$$

where i_B = r.m.s. bias current through R_{Sn}, and $\Delta R_{Sn} = S\ \Delta T$. Therefore

$$\Delta P + i_B^{\,2}\ S\ \Delta T = G\ \Delta T$$

or
$$\Delta T = \frac{\Delta P}{G_e}$$

where the equivalent conductance G_e is given by

$$G_e = G - i_B^{\,2}\ S$$

So far the bolometer frequency response has been neglected. For a single dominant bolometer time constant τ_B,

$$\tau_B = C/G_e$$

then
$$\Delta T = \frac{\Delta P}{G_e(1 + s\ \tau_B)}$$

i.e.
$$B(s) = \frac{1}{G_e(1 + s\ \tau_B)}$$

Sensor

For the Sn temperature sensor

$$\beta = \frac{1}{R_{Sn}} \frac{dR_{Sn}}{dT}$$

therefore $\Delta R_{Sn} = \beta R_{Sn} \Delta T$

no significant time constant is expected, therefore

$$S = \beta R_{Sn}$$

Element responsivity, r

The element transfer function is therefore

$$\frac{\Delta v}{\Delta P} = - i_B S B(s)$$

$$= \frac{- V_d \beta}{G_e (1 + j \omega \tau_B)}$$

For an absorbed radiation power input ΔP where $\Delta P = \alpha \Delta P_r$, ΔP_r being the radiation signal power incident on the bolometer,

$$r = \left| \frac{\Delta v}{\Delta P_r} \right| = \frac{\alpha V_d \beta}{G_e (1 + \omega^2 \tau_B^2)^{\frac{1}{2}}} \quad \ldots (2.1)$$

where r is the bolometer element responsivity for a radiation power input.

Modulator

The bias current produces

$$\Delta v \cos 2 \pi f_o t = m(t) \Delta R_{Sn}$$

where f_o is the Sn sensor bias current frequency and $m(t) = 2^{\frac{1}{2}} i_B \cos 2 \pi f_o t$.

Bridge, transformer and pre-amp

The combination of the bridge, transformer and pre-amp has a simple a.c. voltage to a.c. voltage transformation $A_1(s)$ and, assuming the bandwidth to be very much greater than $A_2(s)$ or $B(s)$, then $A_1(s)$ has the empirically determined frequency independent value A_1.

Demodulator/Amplifier

The demodulation function is performed by the p.s.d. and is given by (see Appendix I)

$$d(t) = 2^{\frac{1}{2}} \cos 2 \pi f_o t$$

The p.s.d. gives an a.c. voltage to d.c. voltage transformation with a time constant represented by

$$- \frac{A_2}{(1 + s \tau_A)}$$

where A_2 is an empirically determined positive quantity and the negative sign represents the correct phase relationship between the input signal to the bolometer and the p.s.d. output.

Overall transfer function

As the product of $m(t)$ and $d(t)$ is just i_B (see Appendix I), the overall transfer function is therefore

$$Y(s) = \frac{\Delta V}{\Delta P'} = - A_2(s) \; A_1 \; i_B \; S \; B(s)$$

where $\Delta P'$ is the error signal produced by the differencing element at the servo input (see Figure (2.2a)) and ΔV is the change in voltage at the p.s.d. output. Therefore

$$Y(s) = - \frac{A_2}{(1 + s \tau_A)} \cdot A_1 \; i_B \; \beta \; R_{Sn} \cdot \frac{1}{G_e (1 + s \tau_B)}$$

$$= \frac{A_1 \; A_2 \; i_B \; \beta \; R_{Sn}/G_e}{(1 + s \tau_A)(1 + s \tau_B)}$$

$$\equiv \frac{-A}{(1 + s\tau_A)(1 + s\tau_B)} \qquad \text{say}$$

where $G_e = G - i_B^2 R_{Sn} \beta = G - \beta P_B$

and $A = A_1 A_2 i_B \beta R_{Sn}/G_e$

Feedback

The power fed back is $I_F^2 R_H = P_F$, therefore

$$\Delta P_F = 2 I_F \Delta I_F R_H$$

and $\Delta I_F = \frac{\Delta V}{R_F}$ if $R_F >> R_H$

therefore

$$\Delta P_F = 2 I_F \frac{R_H}{R_F} \Delta V = a \Delta V$$

therefore for a closed loop

$$\Delta V = Y(s) \Delta P' = Y(s) (\Delta P + \Delta P_F)$$

$$= Y(s) \Delta P + Y(s) a \Delta V$$

where $a = 2 I_F R_H/R_F$

i.e. $\Delta V = \frac{Y(s)}{1 - a Y(s)} \cdot \Delta P$

therefore $\Delta P_F = \frac{a Y(s)}{1 - a Y(s)} \cdot \Delta P$

$$= G(s) \Delta P$$

where $G(s) = \frac{a Y(s)}{1 - a Y(s)}$

From the form derived for Y(s), G(s) can be written as

$$G(s) = -\frac{K}{K+1} \cdot \frac{1}{1 + \left[\frac{\tau_A+\tau_B}{K+1}\right]s + \frac{\tau_A\,\tau_B}{K+1}\,s^2}$$

or, in standard form

$$G(s) = -\frac{K}{K+1} \cdot \frac{1}{1 + 2\,\xi\,\frac{s}{\omega_o} + \frac{s^2}{\omega_o^2}} \qquad \ldots (2.2)$$

where $\omega_o = \left\{\frac{K+1}{\tau_A\,\tau_B}\right\}^{\frac{1}{2}}$

$$\xi = \tfrac{1}{2}\left\{\frac{(\tau_A+\tau_B)^2}{(K+1)\,\tau_A\,\tau_B}\right\}^{\frac{1}{2}}$$

therefore $\omega_o = \frac{\tau_A+\tau_B}{2\,\xi\,\tau_A\,\tau_B}$

and $K = a\,A$

i.e. $$K = \frac{2\,A_1\,A_2\,i_B\,I_F\,\beta\,R_{Sn}\,R_H}{G_e\,R_F} \qquad \ldots (2.3)$$

Figure (2.3a) shows the frequency response of the transfer function F(s) where

$$F(s) = \frac{1}{\left\{1 + 2\,\xi\,\frac{s}{\omega_o} + \frac{s^2}{\omega_o^2}\right\}}$$

plotted against the normalised frequency ω/ω_o for various values of ξ. Note that this function is equal to $-G(s)$ if $K \gg 1$.

Transient response

From standard theory[5], the step response of a second order feedback system with unity closed loop d.c. gain, i.e. with a transfer function equal to F(s), is given by

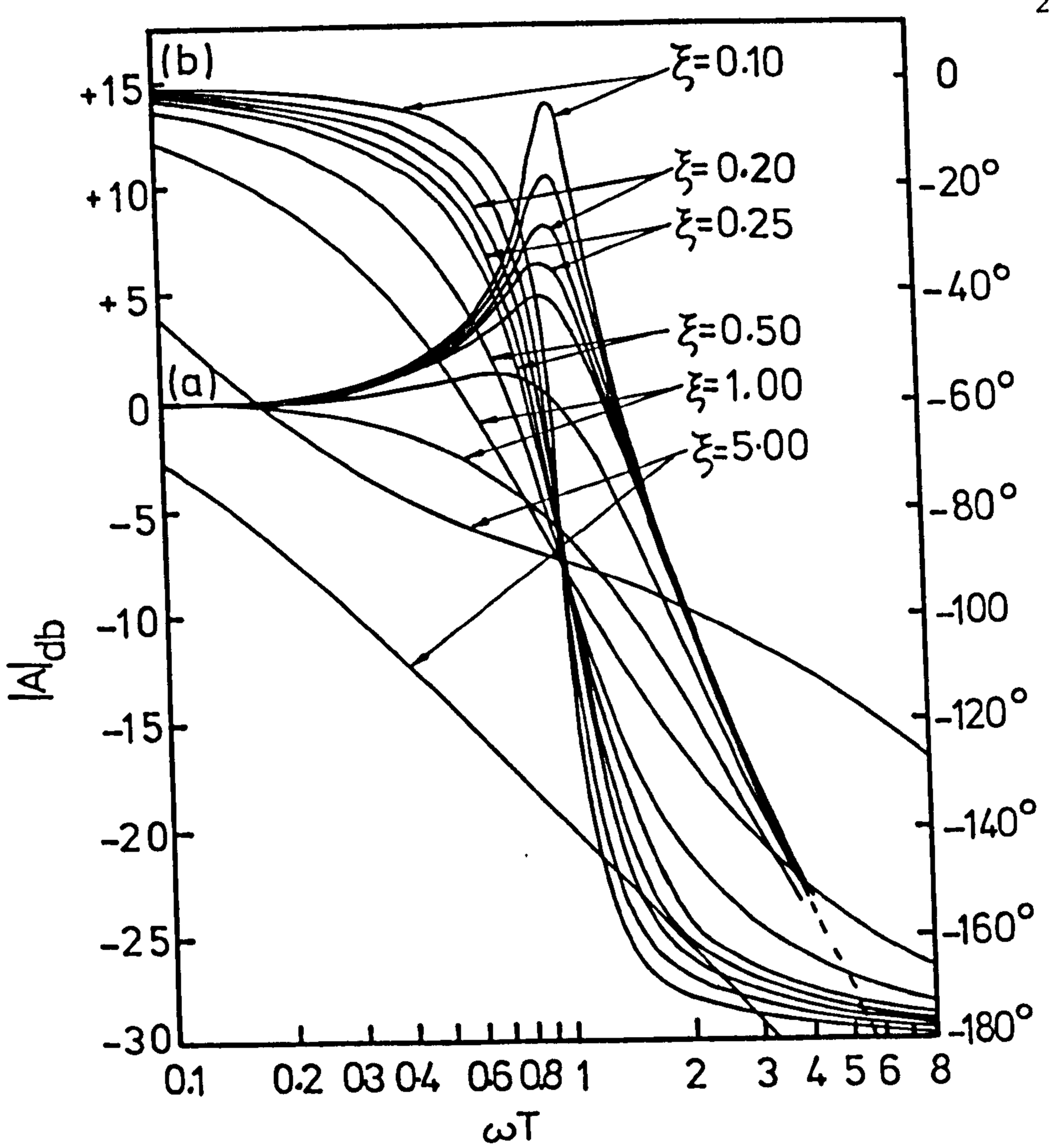

Figure 2.3(a). Frequency response for the transfer function F(s) showing gain and phase-shift curves.

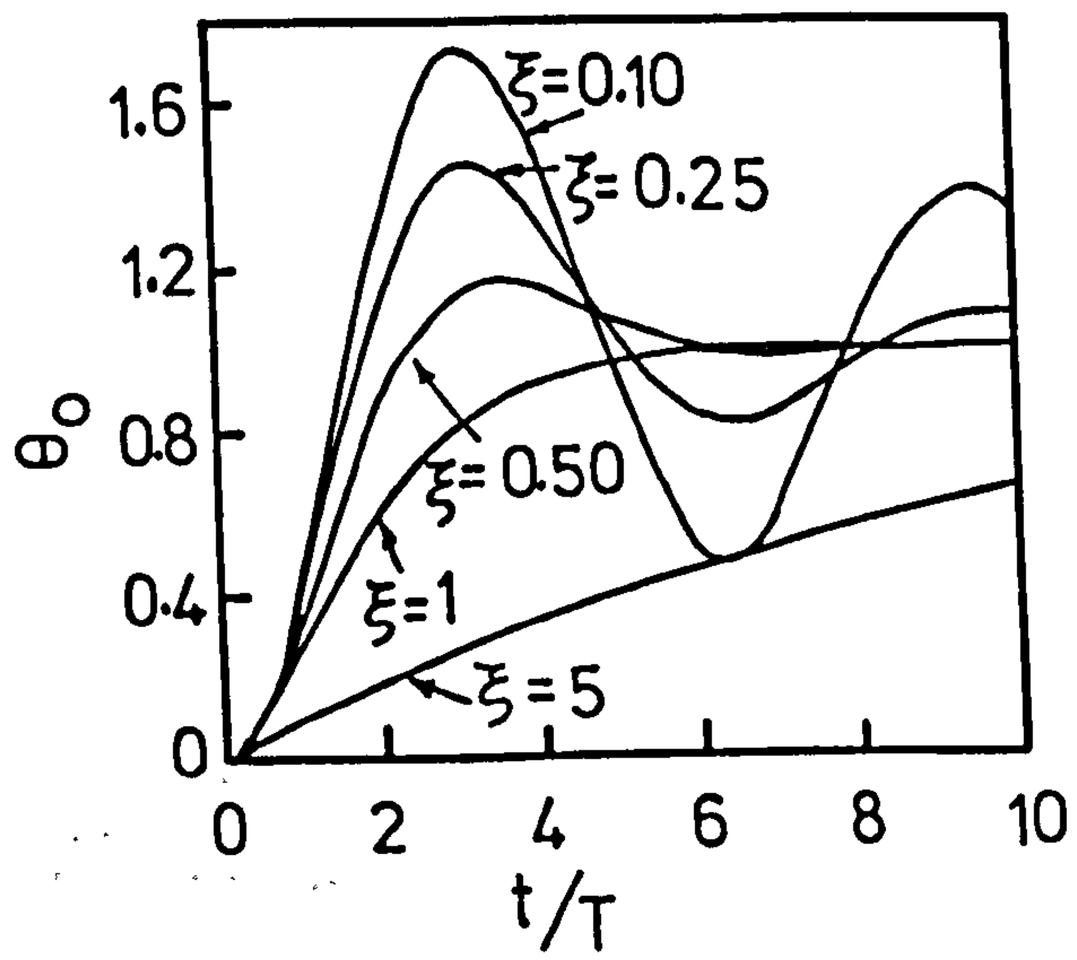

Figure 2.3(b). Transient response for the transfer function F(s).

for $0 < \xi < 1$

$$\theta_o(t) = 1 - \frac{e^{-\xi\omega_o t}}{(1-\xi^2)^{\frac{1}{2}}} \left[\sin \left\{ \omega_o (1-\xi^2)^{\frac{1}{2}} \cdot t + \tan^{-1} \left[\frac{(1-\xi^{\frac{1}{2}})^{\frac{1}{2}}}{\xi} \right] \right\} \right] \quad \ldots (2.4)$$

for $\xi = 1$

$$\theta_o(t) = 1 - e^{-\omega_o t}(1 + \omega_o t) \quad \ldots (2.5)$$

and for $\xi > 1$

$$\theta_o(t) = 1 - e^{-\xi\omega_o t} \left[\cosh\left\{ \omega_o (\xi^2 - 1)^{\frac{1}{2}} \cdot t \right\} + \frac{\xi}{(\xi^2-1)^{\frac{1}{2}}} \sinh\left\{ \omega_o (\xi^2 - 1)^{\frac{1}{2}} \cdot t \right\} \right] \quad \ldots (2.6)$$

where $\theta_o(t)$ is the servo output at time t. Figure (2.3b) shows the transient response of F(s) plotted against $\omega_o t$ for various ξ.

It should be noted that in all the expressions quoted in this section, ΔP is the signal power actually absorbed and converted into heat energy by the substrate. Because of the imperfect optical coupling between the substrate and the incident radiation signal ΔP_r, ΔP will represent only a fraction of the true (radiation) signal input. Therefore if

$$\Delta P = \alpha \, \Delta P_r$$

where α = the fraction of the incident radiation absorbed, then the response to a radiation signal power ΔP_r, i.e. K_r, will be given by

$$K_r = \alpha \, K.$$

See Chapter IV for a discussion of the value of α.

2.3 Noise

2.3.1 Noise sources

Several factors contribute to the overall noise power of the detection system and limit the minimum detectable radiation signal. The main sources of noise are:

(1) Phonon noise, which arises from the random statistical fluctuations in the exchange of energy between the bolometer and the heat sink. The noise power from this source is given by

$$W_{ph} = (4\ k\ T^2\ G_e)^{\frac{1}{2}}\ W.Hz^{-\frac{1}{2}} \qquad \ldots (2.7)$$

The phonon noise can be regarded as being injected at point 1 on the diagram of the functional servo loop illustrated in Figure (2.2a).

(2) Johnson noise:- any resistance R produces a Johnson noise given by

$$e_J = (4\ k\ T\ R)^{\frac{1}{2}}\ V.Hz^{-\frac{1}{2}}$$

From Figure (2.1), it is seen that there are several resistances which could add noise to the bolometer output, particularly the room temperature bias resistors R_{B_1} and R_{B_2}, and the feedback resistances R_{F_1} and R_{F_2}. The fraction of the Johnson noise produced by these resistors dropped across R_{Sn}, R_d and R_H can be made negligibly small, however, if the ratio of the cooled resistance to its load resistance is made sufficiently small. For example, the Johnson noise from R_{B_2} dropped across R_d is given by

$$\frac{R_d}{R_d + R_{B_2}} \cdot (4\ k\ T\ R_{B_2})^{\frac{1}{2}}\ V.Hz^{-\frac{1}{2}}$$

which, if $R_d \ll R_{B_2}$,

$$\rightarrow R_d \cdot \left\{\frac{4\ k\ T}{R_{B_2}}\right\}^{\frac{1}{2}}$$

$$\rightarrow 0 \quad \text{as} \quad \frac{R_d}{R_{B_2}} \rightarrow 0$$

A similar consideration applies to R_{B_1}, R_{F_1} and R_{F_2} and R_{Sn} and R_H respectively. This leaves R_{Sn} and R_d as the dominant Johnson noise sources. The Johnson noise developed across the transformer primary terminals by these two resistances is

$$e_J = (4\ k\ T\ R_D)^{\frac{1}{2}} \quad V.Hz^{-\frac{1}{2}} \qquad \ldots (2.8)$$

where $R_D = R_{Sn} + R_d$. As this Johnson noise is added to the modulated voltage developed across the Sn sensor, it can be regarded as being injected at point 3 in Figure (2.2a).

(3) Low frequency current noise in the Sn sensor:-

The work of Clarke and Voss[6] implies that "1/f" type noise in current biased Sn films at room temperature, evaporated onto glass substrates, is caused by thermal fluctuations along the length of the film which modulate its resistance. They have produced a semi-empirical formula which is in good agreement with experimental results obtained by Clarke and Hsiang[7] for Sn films at the superconducting transition evaporated onto glass. It must be noted that the Sn films used as temperature sensors for the STEB's produced for this thesis were evaporated onto sapphire, not glass, substrates and therefore the results and theory of [6], [7] can only serve as a guide when used to account for low frequency noise in these bolometers.

From [6], for a bar shaped Sn film of dimensions ℓ_1, ℓ_2, ℓ_3 where $\ell_1 >> \ell_2 >> \ell_3$, the voltage noise spectrum, $S_V(f)$, of the film in the frequency range $f_1 < f < f_2$ where

$$f_i = \frac{D}{\pi\, l_i^2}$$

D being an empirically derived thermal diffusivity, is given by

$$S_V(f) = \frac{\bar{V}^2\ \beta^2\ k\ T^2}{\left[3 + \ln(f_2/f_1)\right] C_V\ f} \qquad \ldots (2.9)$$

where k = the Boltzmann constant,

C_V = the thermal capacity of the film,

$\bar{V}$ = the mean voltage across the film.

Clarke and Voss' measurements were made using d.c. bias voltages whereas the Sn sensor in the STEB's produced for this thesis was a.c. biased. As the noise voltage arises basically from a fluctuation in the power dissipated by the film to the substrate, it will be assumed that $\bar{V}^2 = \overline{V^2}$ so that $\bar{V}$ in fact is equal to the r.m.s. value of the a.c. bias voltage.

According to Clarke and Voss, the voltage noise spectrum given by Equation (2.9) is produced as a result of the fluctuation in resistance caused by fluctuations in temperature along the length of the film. Therefore, as $\bar{V} = \overline{iR} \simeq \bar{i}_B \,.\, \bar{R}_{Sn}$ in this case, then for a film of dimensions $l_1 >> l_2 >> l_3$

$$S_V(f) = \frac{\bar{i}_B^{\,2}\ \bar{R}_{Sn}^{\,2}\ \beta^2 k\ T^2}{\left[3 + \ln(f_2/f_1)\right] C_V\ f} \qquad \ldots (2.10)$$

The noise spectrum representing the fluctuation in the resistance of the Sn film is therefore

$$S_R(f) = S_V(f)/\bar{i}_B^{\,2}$$

$$= \frac{\bar{R}_{Sn}^{\,2}\ \beta^2\ k\ T^2}{\left[3 + \ln(f_2/f_1)\right] C_V\ f} \qquad \ldots (2.11)$$

(4) Transformer/pre-amp noise: the transformer cannot be

regarded as noiseless (see Chapter III). It is convenient to refer the noise developed across the transformer secondary terminals as originating entirely from a noise generator e_T in series with the primary winding. The injection point for this noise source will therefore be point 3. Note that e_T will also include the equivalent input noise of the pre-amp referred to the transformer primary, and the Johnson noise produced by the transformer windings resistance.

(5) heat sink temperature fluctuations:- the fluctuation in thermal power delivered to the bolometer element due to a heat sink temperature fluctuation $\Delta T_{h.s.}$ $^{o}K.Hz^{-\frac{1}{2}}$ is given by

$$W_{h.s.} = \frac{G_e \ \Delta T_{h.s.}}{|1 + j\ 2\pi f\ \tau_B|} \qquad \ldots(2.12)$$

where the factor $|1 + j\ 2\pi f\ \tau_B|$ accounts for the thermal filtering by the bolometer time constant, τ_B. $W_{h.s.}$ is injected at point 1 in Figure (2.2a).

(6) Photon noise:- photon noise arises from fluctuations in the background power illuminating the bolometer. For a thermal bolometer, the expression for the noise power at the detector is[8]

$$\overline{\Delta P_B^{\,2}} = \frac{4A(kT_B)^5}{c^2 h^3} \ \Delta f \sin^2\frac{\theta}{2} \int_{x_1(T)}^{x_2(T)} \frac{x^4 e^x}{(e^x - 1)^2} \ f(x,T)\ dx \qquad \ldots(2.13)$$

where $\overline{\Delta P_B^{\,2}}$ = mean square fluctuation in radiation power at the detector,

A = the area of the aperture used with the cooled detector optics (i.e. the radiation cone aperture, see Chapter III),

Δf = post-detection system bandwidth,

T_B = background temperature,

θ = conical viewing angle,

$$x_1(T) = \frac{h\,\nu_1(T)}{kT}, \qquad x_2(T) = \frac{h\,\nu_2(T)}{kT}$$

where $\nu_1(T)$ and $\nu_2(T)$ are the lower and upper cut-off frequencies respectively and are functions of T (the temperature of the bolometer optics). Note that $\overline{\Delta P_B^{\,2}}$ is the mean square fluctuation in radiation power at the detector. This corresponds to a fluctuation in power absorbed by the detector of $\alpha(\overline{\Delta P_B^{\,2}})^{\frac{1}{2}}$ where α is the fraction of incident radiation power absorbed by the detector. The noise spectrum S_B representing the fluctuation in radiation power absorbed by the element can be regarded as being injected at point 1 in Figure (2.2a).

2.3.2 System noise

The servo loop treats the noise sources differently depending on their point of injection. It is therefore necessary to refer all noise spectra back to the input of the servo system, i.e. point 1 in Figure (2.2a).

It is shown in Appendix I that, provided the noise spectrum is white over the bandwidth of B(s), then the double-sided noise spectrum $S_3(f)$ injected at point 3 is equivalent to a spectrum $S_3'(f)$ at the servo input given by

$$S_3'(f) = \frac{S_3(f_o)}{i_B^{\,2}\left|B(j\,2\pi f)\right|^2 S^2} \quad -\frac{\Delta f}{2} \leq f \leq +\frac{\Delta f}{2}$$

$$= 0 \qquad \text{otherwise}$$

where Δf is the bandwidth of $B(j\,2\pi f)$ and f_o is the frequency of the cosinal modulation function $m(t) = 2^{\frac{1}{2}}\, i_B \cos 2\pi\, f_o\, t$.

There are two sources of noise injected at this point (N.B. all noise spectra in this section will now be quoted using two-sided spectra):

Johnson noise from R_D = 2 k T R_D Δf Volts^2 and transformer/pre-amp noise = e_T^2 Δf Volts^2.

Therefore

$$S_3'(f) = \frac{2\ k\ T\ R_D + e_T^2}{i_B^2\ S^2 |B(j\ 2\pi f)|^2} \quad W^2.Hz^{-1} \qquad \ldots(2.14)$$

The noise injected at point 2 is the excess low frequency noise produced by the Sn sensor, which, referred back to point 1, becomes

$$S_2'(f) = \frac{S_2(f)}{S^2 |B(j\ 2\pi f)|^2} \qquad \ldots(2.15)$$

$$= \frac{R_{Sn}^2\ \beta^2\ k\ T^2}{2\{3 + \ell n(f_2/f_1)\}\ C_V\ f\ S^2 |B(j\ 2\pi f)|^2} \quad W^2.Hz^{-1} \qquad \ldots(2.16)$$

The noise injected directly into point 1 is the phonon noise W_{ph}, the noise representing heat sink temperature fluctuations, $W_{h.s.}(f)$, and the fraction of the photon noise from the background power absorbed by the bolometer, S_B, i.e.

$$S_1'(f) = 2\ k\ T^2\ G_e + \frac{(G_e \Delta T_{h.s.}(f))^2}{2|1 + 2\pi j f \tau_s|^2} + \frac{\alpha^2\ \overline{\Delta P_B^2}}{2}$$

The total input noise spectrum is given by

$$S_i'(s) = \sum_{n=1}^{3} S_n'(s) \qquad \ldots(2.17)$$

The mean squared input noise power from the servo, W_n^2, for a double-sided spectrum will be

$$W_n^2 = \int_{-\infty}^{+\infty} S_i'(f)\ df$$

$$= \int_{-\infty}^{+\infty} \left[2\ k\ T^2\ G_e + \alpha^2 \overline{\Delta P_B^2} + \frac{(G_e \Delta T_{h.s.}(f))^2}{2|1 + j\ 2\pi f \tau_s|^2} + \frac{(2\ k\ T\ R_D + e_T^2)}{i_B^2\ S^2 |B(j\ 2\pi f)|^2} \right]$$

$$+ \frac{R_{Sn}^{\,2}\ \beta^2\ k\ T^2}{2\{3 + \ell n(f_2/f_1)\}\ C_V\ f\ S^2 |B(j\ 2\pi f)|^2}\Bigg] \cdot df \qquad \ldots(2.18)$$

The spot noise output from the servo in a bandwidth Δf about a given frequency, f, is approximately given by (provided $S_i'(f)$ and $|G(j\ 2\pi f)|$ are roughly constant over Δf).

$$W_n^{\,2}(f) = S_i'(f) |G(j\ 2\pi f)|^2\ \Delta f \quad \text{Watts}$$

and the equivalent input noise power to the servo by (if $|G(j\ 2\pi f)|^2$ is slowly varying over Δf)

$$(S_i'(f)\ \Delta f)^{\frac{1}{2}} \ \text{Watts}^2.$$

In this case, bearing in mind that $S_i'(f)$ is a double-sided spectrum, $S_i'(f) = 2^{-\frac{1}{2}} \times [\text{system NEP at the frequency f}]^2$.

2.4 Bolometer optics

The integrated radiation power emitted in a solid angle Ω by a black body source at a temperature T, incident on an area dA, up to a frequency ν_c, is given by

$$\int_0^{\nu_c} I_\nu\ d\nu\ dA\ d\Omega\ d\cos\theta \qquad \ldots(2.19)$$

where θ represents the inclination of the plane of the receiving area A with respect to the surface of the black body. I_ν is the Planck function and has the form

$$I_\nu = \frac{2\ h\ \nu^3}{c^2} \cdot \frac{1}{e^{h\nu/kT} - 1}$$

If $h\nu/kT \ll 1$ (true for FIR radiation) then

$$I_\nu \simeq \frac{2\ h\ \nu^3}{c^2} \cdot \frac{kT}{h\nu}$$

$$= \frac{2\ \nu^2\ kT}{c^2}$$

Therefore Equation (2.19) gives

$$\int_0^{\nu_c} \frac{2\ \nu^2\ k\ T}{c^2}\ d\nu\ dA\ d\Omega\ d\cos\ \theta$$

$$= \frac{2}{3} \cdot \frac{\nu_c^{\ 3}\ k\ T}{c^2}\ dA\ d\Omega\ d\cos\ \theta$$

$$= \frac{2}{3} \cdot \frac{c}{\lambda_c^{\ 3}}\ k\ T\ dA\ d\Omega\ d\ \cos\ \theta \qquad \ldots(2.20)$$

where λ_c is the cut-off wavelength of the filters. Equation (2.20) can be used to calculate the background power incident on the bolometer from the surroundings, which are assumed to have approximately black body emission characteristics, at temperature T by assuming dA to be the area of the aperture in front of the (assumed lossless) collecting cone focussing radiation onto the detector element. $d\Omega$ will be the effective solid angle of acceptance. See Chapter III for details of the determination of these parameters.

CHAPTER II

REFERENCES

(1) Pippard, A.B., Proc. Royal Soc. A216, 547 (1953).

(2) Blumberg, R.H. and D. P. Seraphim, J. Appl. Phys. 33, 163 (1962).

(3) Chopra, K.L., 'Thin Film Phenomena', McGraw-Hill Book Company, New York (1969), pp. 538 and 548.

(4) Hunt, T.K. and J. E. Mercereau, Phys. Rev. Letts. 18, 551 (1967).

(5) Pitman, R.J.G., "Automatic Control Systems Explained", St. Martin's Press, New York (1966), pp. 148.

(6) Clarke, J. and R. F. Voss, Phys. Rev. Letts. 33, No. 1, 24 (1974).

(7) Clarke, J. and T. Y. Hsiang, Phys. Rev. Letts. 34, No. 19, 1217 (1975).

(8) Putley, E.H., Physica Status Solidi 6, 571 (1964).

CHAPTER III

CONSTRUCTION

3.1 Bolometer fabrication

Only a brief summary of the bolometer fabrication is given in this section. A detailed description is given in a Queen Mary College internal report[1]. The bolometer is shown in Figures (3.1a) and (3.1b) and its fabrication schematically in Figure (3.2). The fabrication procedure can be summarised as follows:

A.

(1) contact pads of 2 μm thick In are deposited on top of 1000 Å thick Cr pads (improving the adhesion of the In film to the substrate) which are themselves deposited onto a cleaned, polished 60 μm thick by 5.0 mm diameter sapphire substrate.

(2) a zig-zag shaped Sn track, 500 Å thick by 100 μm wide by 12.5 mm long in total, is evaporated between two of the contact pads (the zig-zag track is chosen to give a higher, more convenient to work with, Sn resistance).

(3) 2 mm by 100 μm by 650 Å Bi heater is evaporated between the other pair of contacts.

B.

(1) a pair of cleaned 60 μm nylon leads tensioned to 5 grms weight are attached to an anodised Aluminium mount using G.E. 7031 varnish.

(2) the nylon threads are coated along the appropriate lengths with a 1500 Å Pb film evaporated on top of a 400 Å thick copper (Cu) underlay (Pb is superconducting at ^{4}He temperatures making the leads resistance negligible; the Cu underlay is necessary to give a

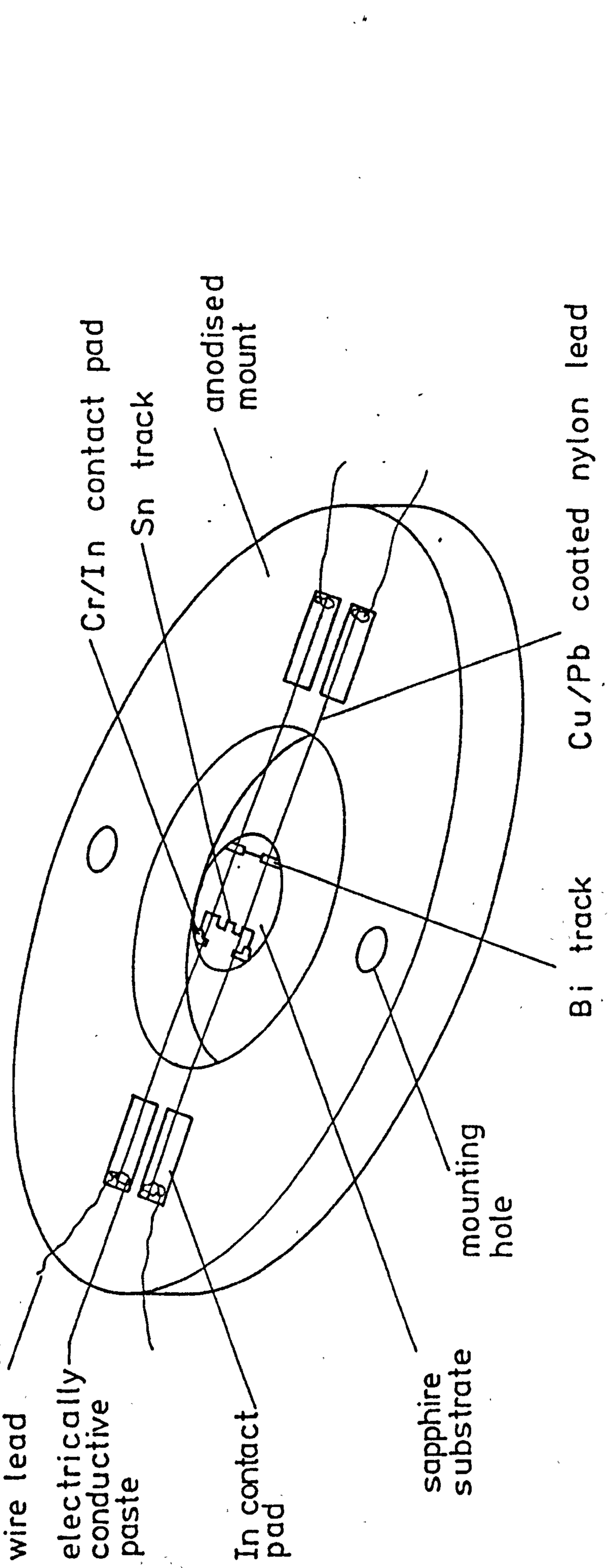

Figure 3.1(a). The bolometer.

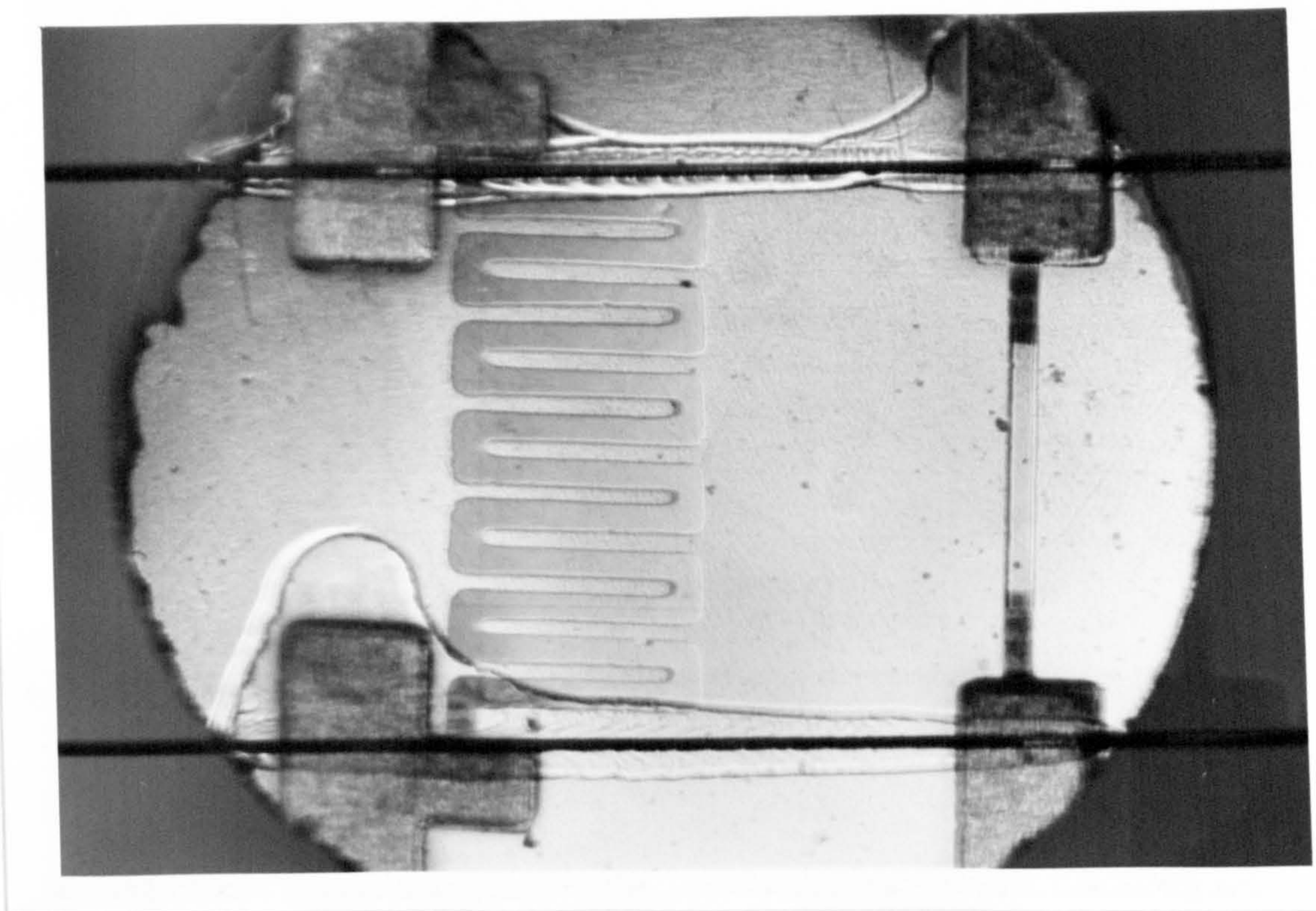

Figure 3.1(b). The 5mm diameter bolometer substrate.

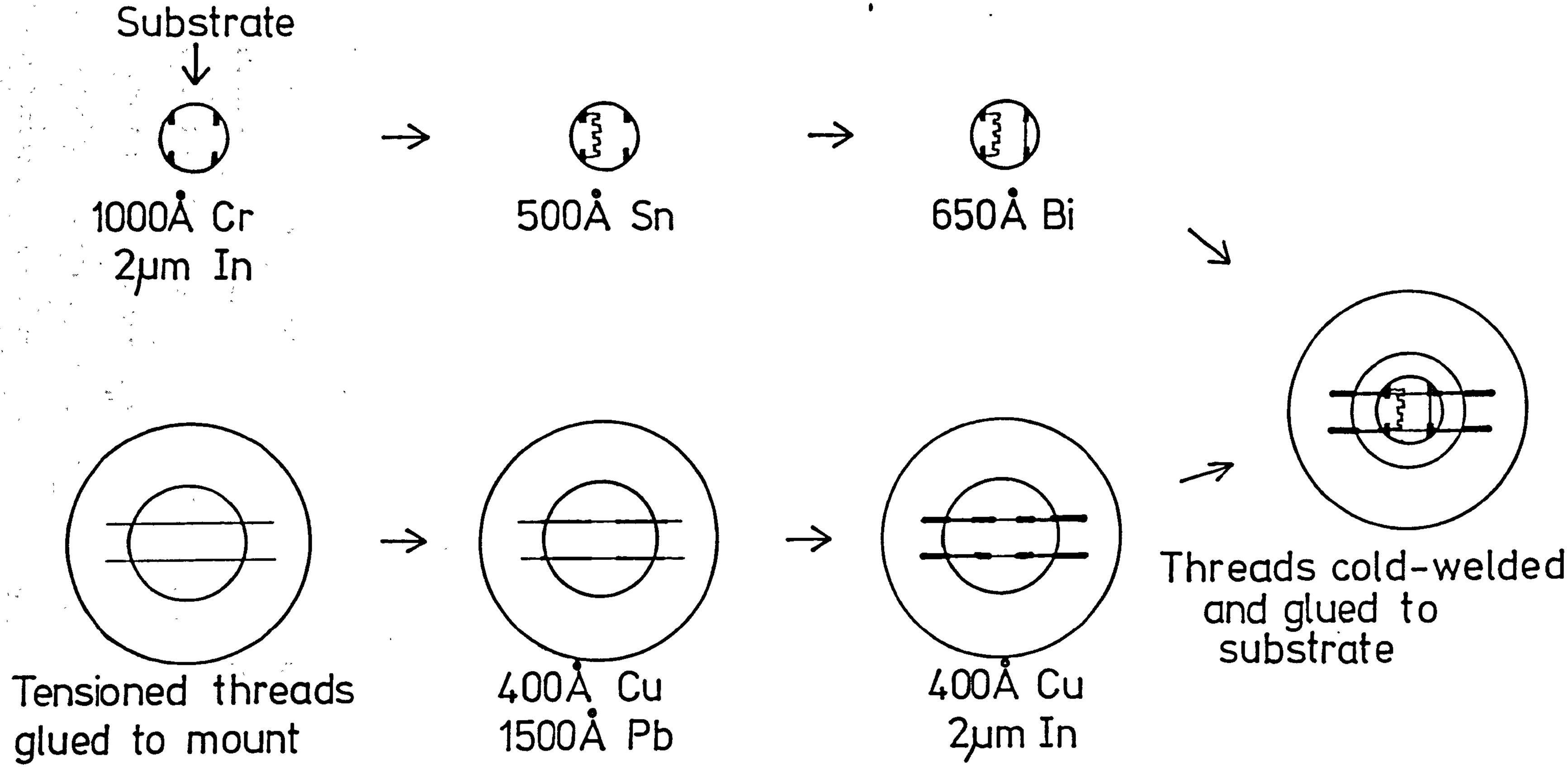

Figure 3.2. Bolometer fabrication.

continuous Pb film).

(3) regions of the nylon threads where contact to the substrate is to be made and where the nylon leads are to be attached to the mount are coated with a 2 μm In film over a 400 Å Cu underlay (the Cu underlay improves In adhesion).

C.

(1) the threads are cold-welded to the saphhire substrate using light and carefully controlled pressure on the nylon leads at the In contacts.

(2) the mechanical strength of the contacts is increased by glueing with G.E. 7031 varnish.

D.

(1) a Bi film, ≃ 180Ω/sq. at ^{4}He temperatures to remove Fabry-Perot interference fringes (see Chapter IV), is evaporated onto the uncoated surface of the substrate to act as an absorber for incident IR radiation.

E.

(1) two pairs of enamelled copper wire lead-out wires are stuck to the In contacts on the mount with G.E. 7031 varnish.

(2) electrical connection between bared ends of the lead-out wires and nylon leads is made with electrically conductive paint.

This method of construction produced bolometer elements with the following typical parameters at 3.7°K (see Chapter V);

thermal capacity (C)	- 2.4×10^{-6} J.°K^{-1}
thermal conductance (G)	- 1.6×10^{-6} W.°K^{-1}
bolometer time constant (τ_B)	- 1.5 secs
Sn sensor (normal) resistance (R_{Sn})	- 14 Ω
Bi heater resistance (R_H)	- 2.2 kΩ

resistance per square of absorbing

Bi film ($R_{sq.}$) - 180 Ω/sq.

The calculated thermal capacities of the element are given in Table (3.1). The total volume of the G.E. varnish used to reinforce the mechanical strength of the contacts could not be determined easily and therefore the values given for the volume of the varnish and its thermal capacity are very approximate. It will be seen that the total calculated thermal capacity is 2.4×10^{-7} J.^{o}K^{-1} compared with the measured value of 2.4×10^{-6} J.^{o}K^{-1}. One possible cause of error is the uncertainty in the value of c_v for the nylon leads (the quoted value for c_v for nylon is for Nylon II) as the type of nylon used for the leads was not known. It may also be that the dimensions of the G.E. varnish layer are very inaccurate. It was particularly difficult to estimate the volume of varnish which had heaped up around the leads.

3.2 Detector optics

A schematic diagram of the ^{4}He-cooled optics and fittings is shown in Figure (3.3). The fitting supporting the bolometer mount and radiation cone is also shown in more detail in Figure (3.4). Incident FIR radiation was collected by an F1.5 radiation cone (the method of measuring the cone F-number is given in section (3.2.2)) after passing through a set of filters and an aperture fixed to the front end of the cone. The bolometer was mounted so that the FIR radiation was incident on the surface of the substrate on which the Sn thermometer and Bi heater were deposited.

TABLE 3.1

Estimated thermal capacities of the bolometer element

	total volume (cm^{-3})	c_v ($J.^oK^{-1}.cm^{-3}$)	c_v ($J.^oK^{-1}$)
Sapphire substrate	1.2×10^{-3}	2×10^{-5} (2)	2.4×10^{-8}
G.E. 7031 varnish	$\simeq 10^{-5}$	2×10^{-4} (2)	$\simeq 2 \times 10^{-8}$
In contacts (4)	2.4×10^{-5}	5.1×10^{-3} (3)	3.1×10^{-8}
Sn track	6.3×10^{-8}	1.15×10^{-3} (3)	7.2×10^{-11}
Bi track	1.3×10^{-8}	3.9×10^{-3} (3)	5.1×10^{-11}
Bi absorber	10^{-6}	3.9×10^{-3} (3)	3.9×10^{-9}
Nylon leads (2)	5×10^{-6}	1.2×10^{-3} (4)	1.2×10^{-7} %

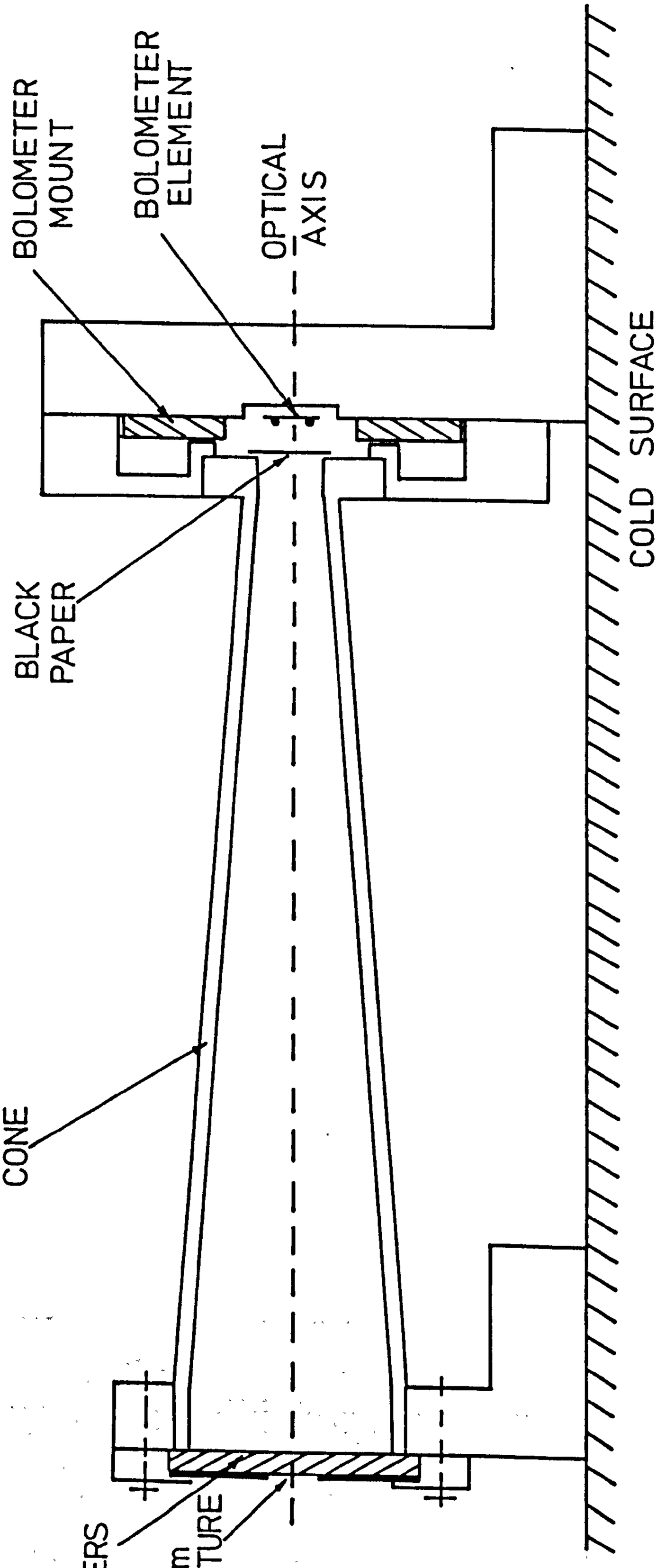

Figure 3.3. Bolometer optics.

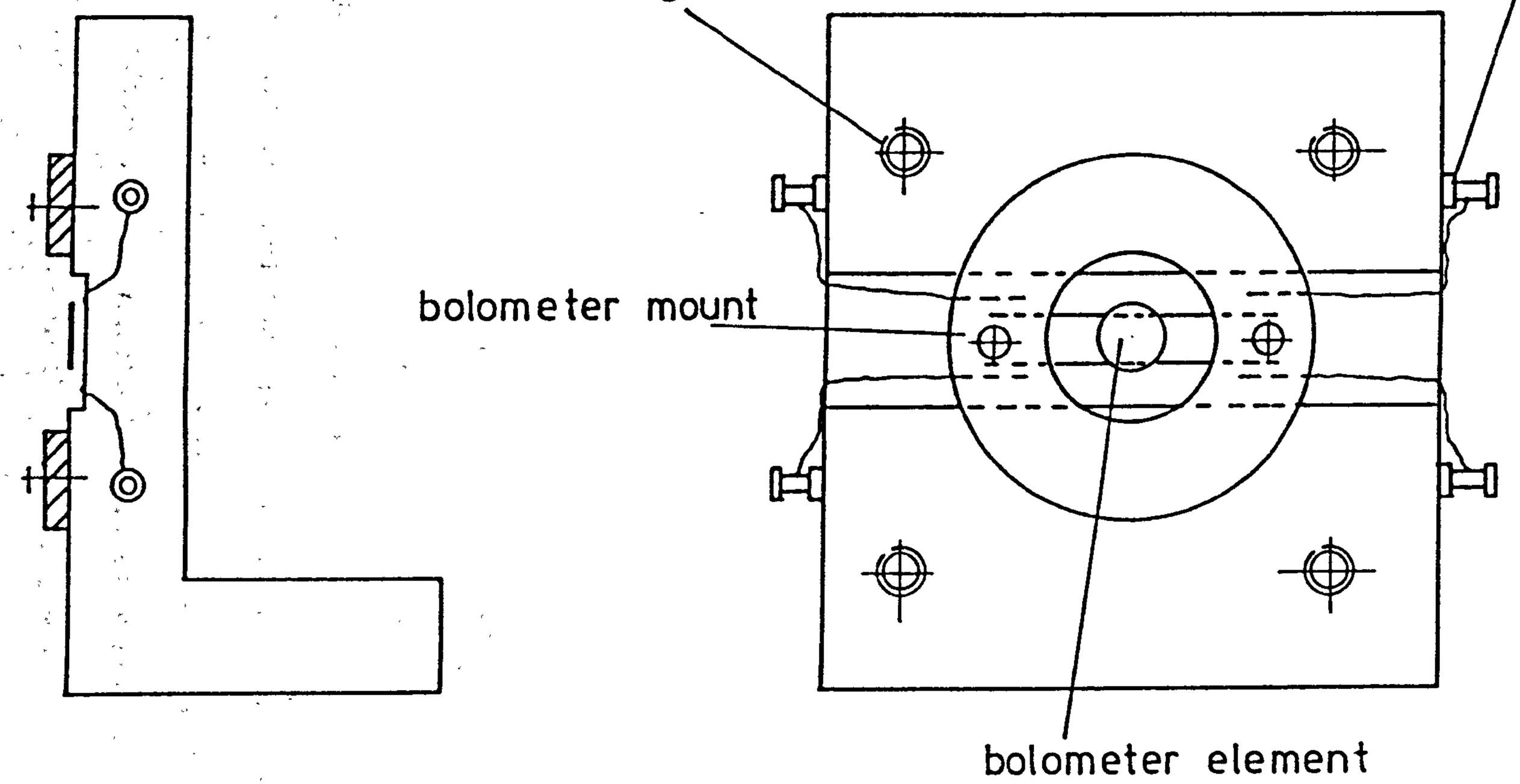

Figure 3.4. Detector mount used for ^{4}He temperature tests.

3.2.1 Filters and filter response

The filters mounted on the front end of the cone were 3 mm thick Fluorogold and a 120 lines per inch (L.P.I.) capacitative mesh, together with a 3 mm aperture made from copper shim. To provide additional filtration at short wavelengths, black paper 100 μm thick was stuck to the rear end of the cone, and the window in the LN_2 radiation shield was covered with 100 μm thick black polyethylene. The transmission characteristic of all these filters together is shown in Figure (3.5). The cryostat window was made from 2 mm thick TPX and can be assumed to have approximately 100% transmission at millimetre wavelengths.

3.2.2 Radiation power falling on element

From Section (2.4), the radiation power P_r incident on an area A from a black body at temperature T, within a solid angle Ω is given by

$$P_r = \frac{2}{3} \cdot \frac{A\ \Omega\ c\ k\ T}{\lambda_c^{\ 3}} \qquad \ldots (3.1)$$

where λ_c is the cut-off wavelength of the filters.

To calculate the background IR power incident on the bolometer, T will effectively be the temperature of the (room temperature) surroundings of the cryostat, as the room temperature radiation is much greater than the radiation from the ^4He surroundings. A will be the area of the aperture placed in front of the radiation cone.

It is difficult to calculate Ω explicitly but it is possible to obtain an approximate value in the following way:

A black body source is moved in an arc of radius f about the centre of the cone aperture, where f is the focal length of the detector optics. The detector response is plotted as a function of the angle of rotation, ∅. The effective area at a distance f from the

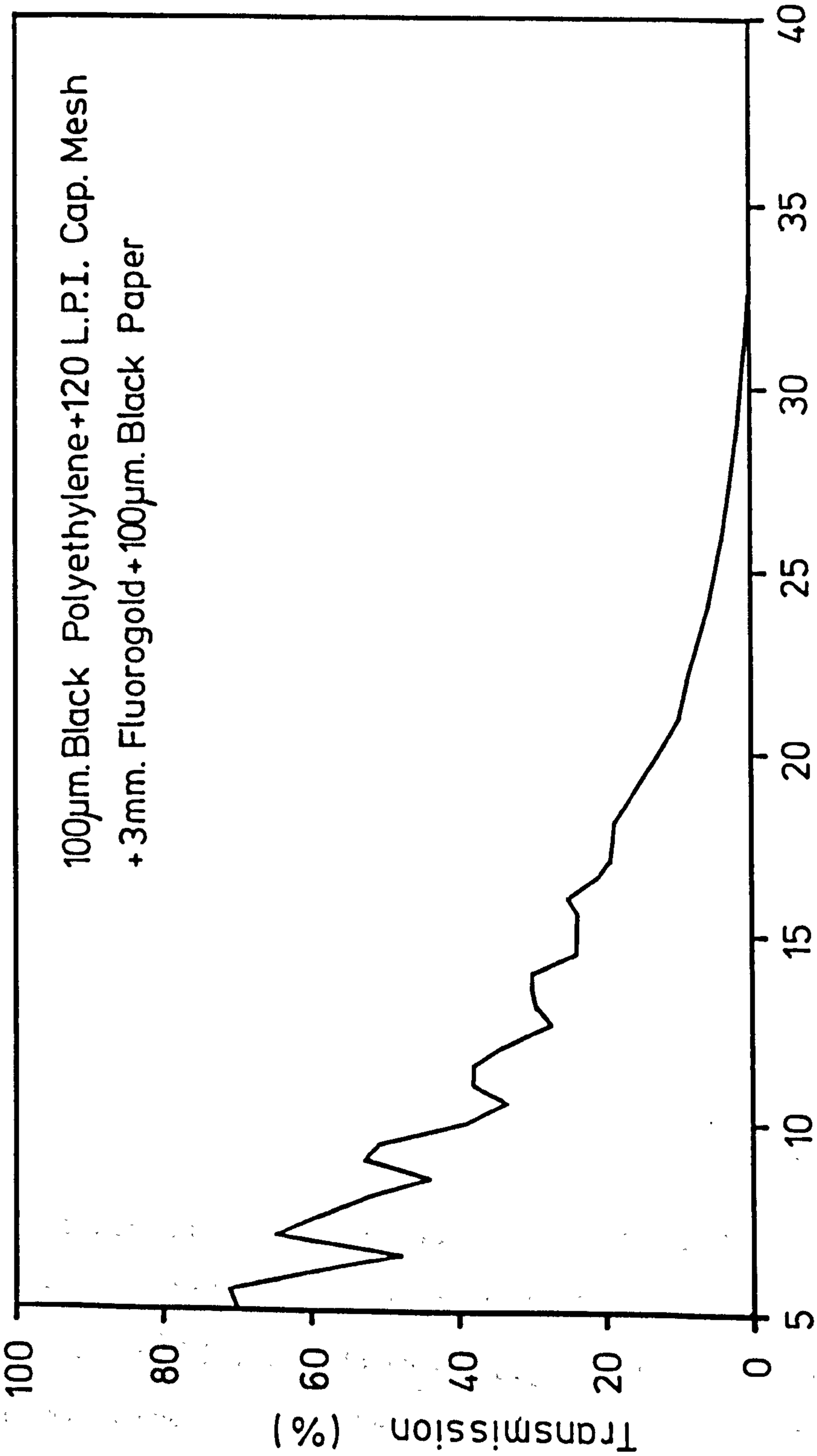

Figure 3.5. Transmission spectrum of cooled filters.

aperture seen by the detector is therefore approximately

$$A_{eff} = \pi\ f(\sin \frac{\phi_{\frac{1}{2}}}{2})^2$$

where $\phi_{\frac{1}{2}}$ is the half power beamwidth of the detector response. Therefore the effective solid angle seen by the detector is

$$\Omega_{eff} = \frac{A_{eff}}{f^2} = \pi \sin^2 \frac{\phi_{\frac{1}{2}}}{2} \quad \ldots (3.2)$$

If it can be assumed that the polar response of the detector optics is determined by the radiation cone used, then $\phi_{\frac{1}{2}}$ is given by

$$\phi_{\frac{1}{2}} = 2 \cdot \tan^{-1} \frac{1}{2F}$$

where F is the radiation cone F-number. For F = 1.5, then $\phi_{\frac{1}{2}} = 37^{o}$ and from Equation (3.2) $\Omega_{eff} = .33$.

In Equation (3.1), Ω is just Ω_{eff}. The receiving area A is the area of the 3 mm diameter cone aperture = 7.1×10^{-6} m^2. $\lambda_c \simeq .6$ mm, corresponding to a cut-off frequency of 15 cm^{-1} (see Figure (3.5)). Therefore the background incident on the detector from the room temperature ($290^{o}K$) surroundings is, from Equation (3.1),

$$P_B = 8.7 \times 10^{-9}\ W$$

In order to be able to calibrate the detector system, i.e. to measure signal-to-noise ratios and responsivity, it was necesary to be able to illuminate the element with a known chopped signal. Ideally the source should be a black body of known temperature completely covering the effective solid angle Ω_{eff} seen by the detector. The radiation chopper is sited between the source and the detector window and must be close enough to the window to cover the Ω_{eff} seen by the detector. The radiation signal incident on the detector at any given

moment will therefore be determined by whether or not the source is being blanked off from the detector by one of the chopper blades. If it is, the instantaneous power falling on the element is given by Equation (3.1) with T equal to the temperature of the chopper blade, i.e. the background temperature T_b. If the detector is being illuminated by the source then the instantaneous radiation power falling on it is again given by Equation (3.1) but with T equal to the temperature of the source T_s. Therefore the modulation of the radiation power incident on the detector is given by

$$P_r = \frac{2}{3} \cdot \frac{A\,\Omega_{eff}\,c\,k}{\lambda_c^{\,3}}\,(T_s - T_b) \qquad \ldots (3.3)$$

A convenient source for approximate calculations is a hand placed close to the cryostat window. T_s is therefore the surface temperature of the hand. T_b is just the temperature of the cryostat surroundings, i.e. the room temperature. If $T_s - T_b \approx 20^{o}K$, then by Equation (3.3)

$$P_r = 4.8 \times 10^{-11}\ W.$$

3.3 Detector electronics

The detector electronics are shown in Figure (2.1). R_d is a cooled resistor mounted on the cryostat ^4He heat sink. It was made from a length of 44 s.w.g. constantan wire stuck onto a rectangular shaped piece of quartz ≈ 1 mm thick, polished on both sides. The quartz was stuck down to the ^4He heat sink with G.E. 7031 varnish to give a good thermal contact, and covered with a copper radiation shield.

The transformer, a Triad Jz-5, was also cooled. It was wrapped in several layers of mu-metal to ensure that it was well shielded from stray magnetic fields and was mounted in a case made from solid high conductivity copper. The case was bolted down to the cryostat heat

sink. The transformer has a turns ratio (n) of 40 and the following specifications at $3.7^{o}K$:

primary inductance, L_p = 20 mH

secondary inductance, L_s = 5.0 H

primary resistance, R_p = .1 Ω

secondary resistance, R_s = 75 Ω

The voltage magnification ratio of the transformer is just n_d (assuming that the load across the secondary terminals is much greater than ωL_s) where n_d^2 is given by

$$n_d^2 = \frac{n^2}{1 + \frac{R_D^2}{\omega^2 L_p^2}} \qquad \ldots (3.4)$$

where R_D = total resistance across the transformer primary. As

$R_L >> R_{Sn}, R_d, R_p$ and $R_p << R_d, R_{Sn}$

$$R_D = R_{Sn} + R_d$$

$$= 10\ \Omega$$

The effective impedance looking into the secondary terminals is

$$n_d^2 R_D + R_s + j\omega L_s \qquad \ldots (3.5)$$

Therefore the current noise produced by the pre-amp will be greater than would have been the case without transformer coupling. The total equivalent input noise of the pre-amp is given by

$$e_A^2 = e_n^2 + i_n^2 Z_A Z_A^*$$

where e_n is the equivalent short circuit input noise, i_n is the equivalent input current noise and Z_A is the load impedance across the

pre-amp input given by Equation (3.5). For the TP-1 pre-amp used (which is described in Appendix II) e_n = .6 n V . $Hz^{-\frac{1}{2}}$ at 1 K Hz and $i_n = 4 \times 10^{-15}$ A . $Hz^{-\frac{1}{2}}$. It therefore turns out that the pre-amp input current noise is negligible in comparison with its input voltage noise at the STEB bias frequency of 1 K Hz and can be ignored.

Transformer noise

It was necessary to find out how much noise was being added by the transformer/pre-amp combination to the noise produced by the bolometer. The method of doing this was to connect a cooled load resistance R_D (= 10 Ω) across the primary to represent the loading presented to the transformer by the bridge. The noise voltage across the output of the TP-1 pre-amp connected across the secondary terminals was measured with a p.s.d. This measured noise was then compared with the noise levels expected using a noiseless transformer. It was then possible to refer the excess noise to an equivalent noise generator e_T connected in series with R_D and the primary. The noise circuit is shown in Figure (3.6). R_D and R_s are noiseless resistances representing the primary load and the secondary winding resistance. e_J and e_s are the respective noise generators due to Johnson noise. Z_A is the load impedance on the pre-amp input and e_n and i_n the equivalent input voltage and current noise respectively of the TP-1 pre-amp.

The p.s.d. used was an Ithaco 391A lock-in amplifier operated in its noise measurement mode. In this mode the p.s.d. gives a d.c. output proportional to the true r.m.s. noise applied to the input at the set frequency and within the set bandwidth. The p.s.d. input noise was 10 nV . $Hz^{-\frac{1}{2}}$, negligible in comparison with the output noise of the pre-amp for any pre-amp input loading.

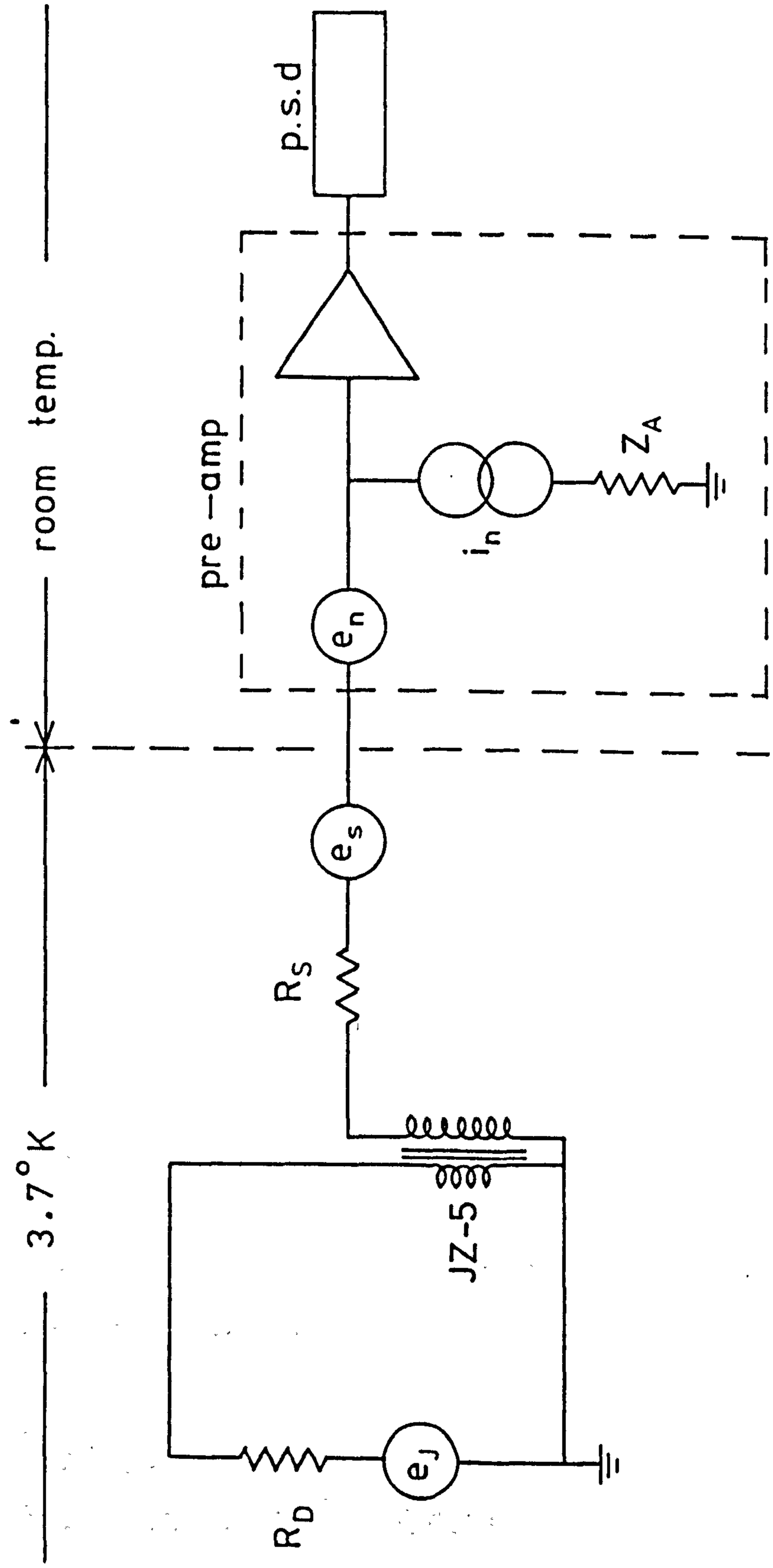

Figure 3.6. Noise circuit for the transformer/pre-amp noise tests.
(Note: R_D includes the primary winding resistance)

The empirical value of e_p $[= (e_J+e_T^2)^{\frac{1}{2}}]$ could be found by dividing the d.c. output of the p.s.d. by the total gain which is n_d x TP-1 gain x p.s.d. conversion gain. Therefore e_T is given by

$$e_T = (e_p^2 - e_J^2)^{\frac{1}{2}}$$

Figure (3.7) shows a plot of e_T versus frequency. Figure (3.8) shows a plot of n_d e_T, e_A and n_d e_J versus frequency to illustrate the relative effect of the different noise sources. Note that at frequencies much less than 1 K Hz, the approximation that $n_d = n$ is no longer valid and this has been taken into account in the figures quoted using Equation (3.4). The increasing size of the error bars at low frequencies is due to increasing errors in noise measurement by the p.s.d. because of the necessarily smaller noise bandwidths used. It will be seen from the graphs that at frequencies less than a few hundred Hertz, the transformer and pre-amp noise is much greater than the Johnson noise from the load resistance R_D. At higher frequencies the excess noise is much reduced and the transformer/pre-amp combination gives a noise figure of only 3.3 dB at 1 k Hz relative to the $3.7^{\circ}K$, 10 Ω Johnson noise produced by R_D. Bearing in mind that noise voltages add in quadrature, it can also be seen that pre-amp noise is insignificant compared to the transformer noise developed across the secondary at any frequency between 100 and 1000 Hz.

3.4 Cryogenics

3.4.1 ^{4}He pressure regulation

An Oxford Instruments MD800 cryostat was used to provide the ^{4}He-cooled heat sink necessary for the operation of the bolometer and optics. It was necessary for the cryostat heat sink to be maintained

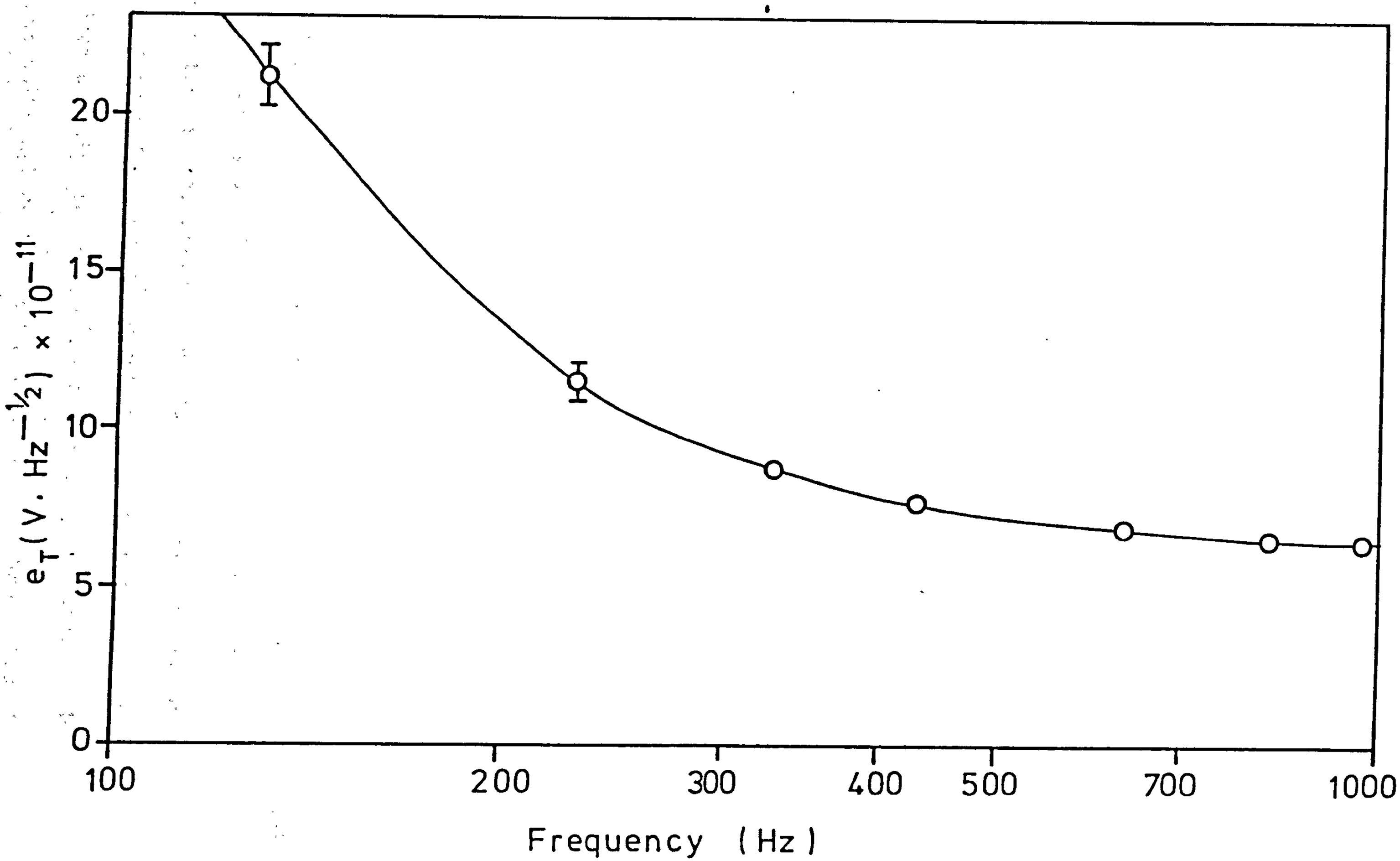

Figure 3.7. e_T versus frequency.

at a steady temperature about 10 m ^{o}K below the operating temperature of approximately 3.7^{o}K (see Chapter V) to allow for the heating effect of the quiescent bias power applied to the element through the Bi heater.

To achieve the required ^{4}He boil-off temperature, the ^{4}He can had to be held at a steady pressure of ≃ 450 mm. Hg using an adjustable pressure regulating device (a manostat) connected in series between the ^{4}He can and vacuum pump. The manostat used was made by Lake Shore Cryotronics Inc., model No. 329. The pressure regulating properties and the consequent temperature stability of the ^{4}He heat sink are discussed in section (3.4.3).

The pressure in the regulated volume was monitored with a mercury manometer. A schematic diagram of the vacuum regulation system is shown in Figure (3.9). The venting valve on the manostat opens intermittently while the manostat is operating and must be connected to an atmospheric pressure ^{4}He gas reservoir to prevent air leaking into the cryostat.

3.4.2 Detector assembly

The detector assembly is shown in Figure (3.10). Plate 1 shows the Cu bottom plate of the ^{4}He can of the cryostat complete with all the ^{4}He-cooled detector fittings. The ^{4}He can in the MD800 cryostat is shielded by an LN_2 temperature (77^{o}K) radiation shield to reduce ^{4}He boil-off. Electrical connection between the terminals on the ^{4}He heat sink and the outer connector was made using 44 s.w.g. enamelled constantan wire to reduce ^{4}He boil-off to a minimum. The 100 μm thick black polyethylene filter was attached to the LN_2 radiation shield with G.E. 7031 varnish.

Electrical connections between terminals on the ^{4}He heat sink

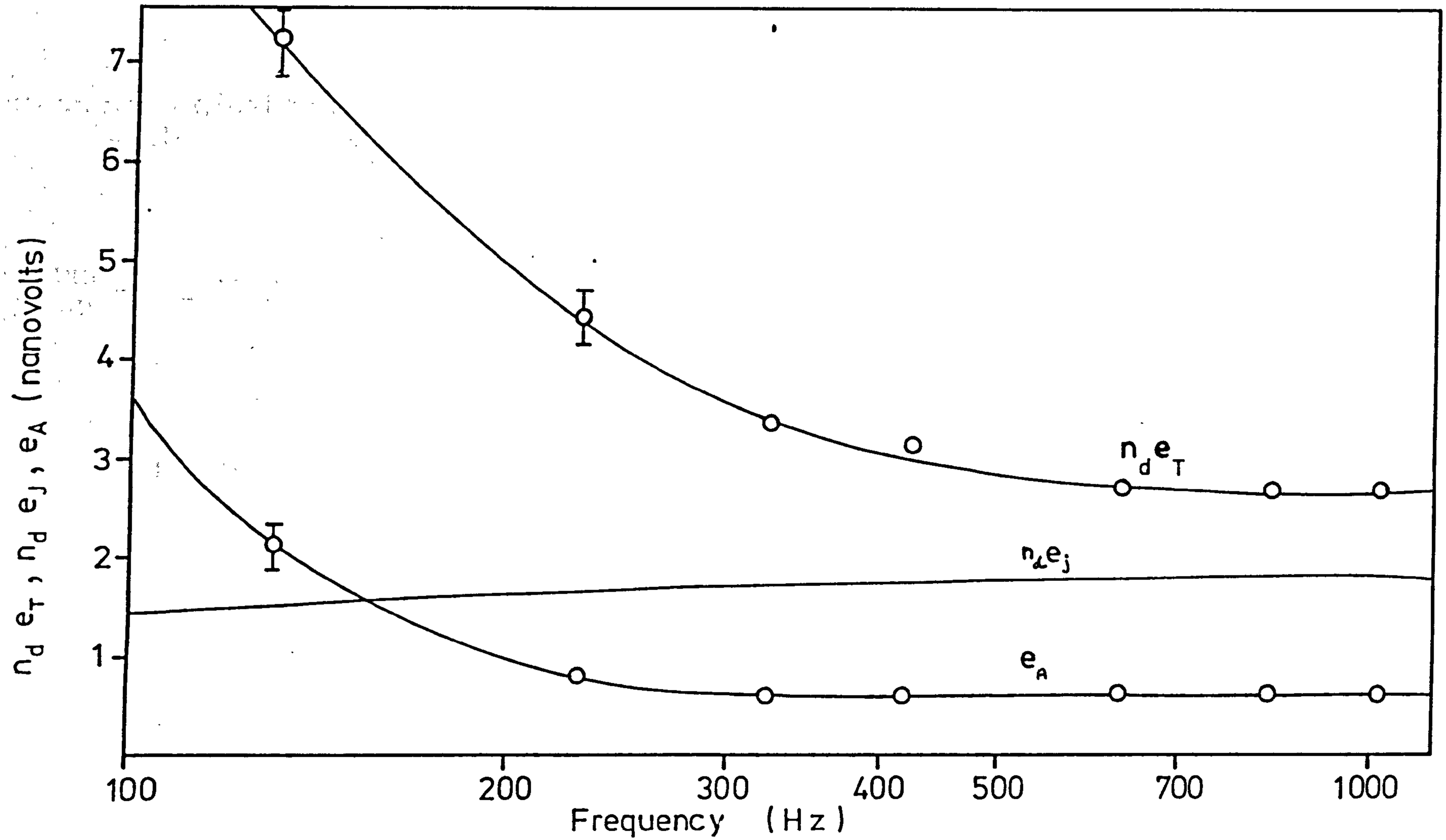

Figure 3.8. $n_d e_T$, $n_d e_J$ and e_A versus frequency.

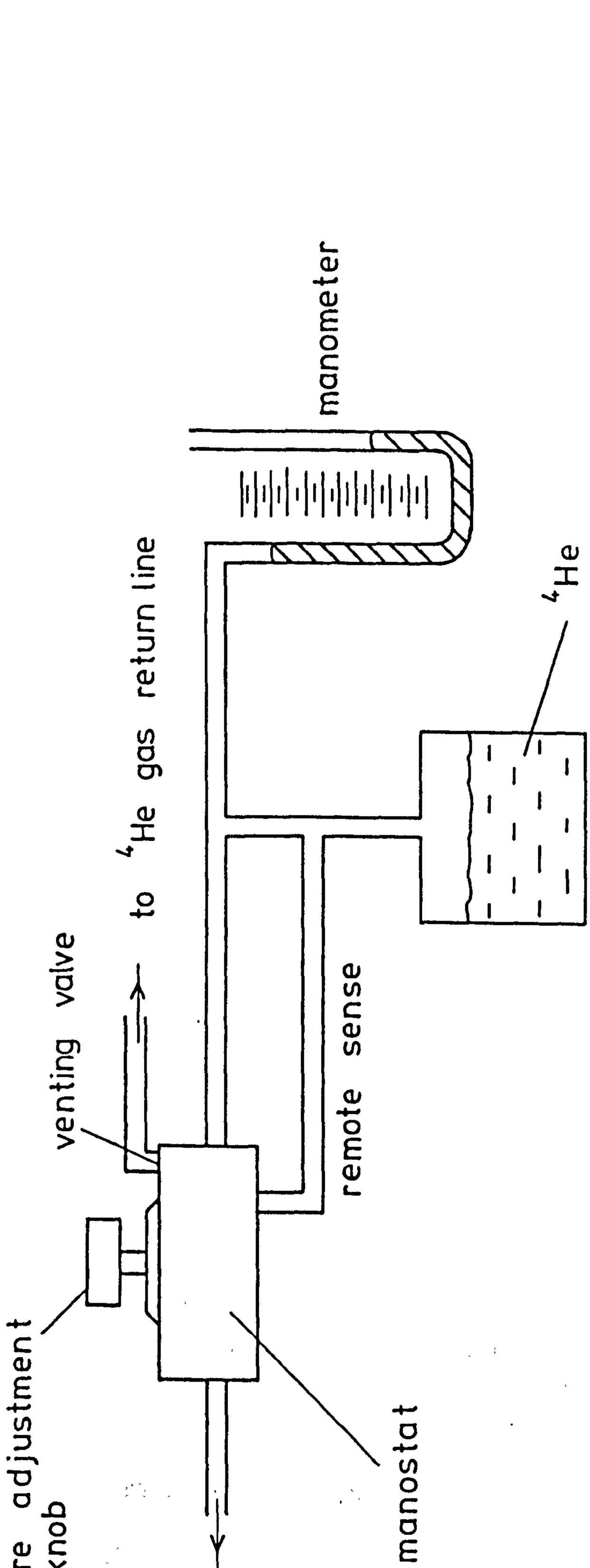

Figure 3.9. ^{4}He pressure regulation.

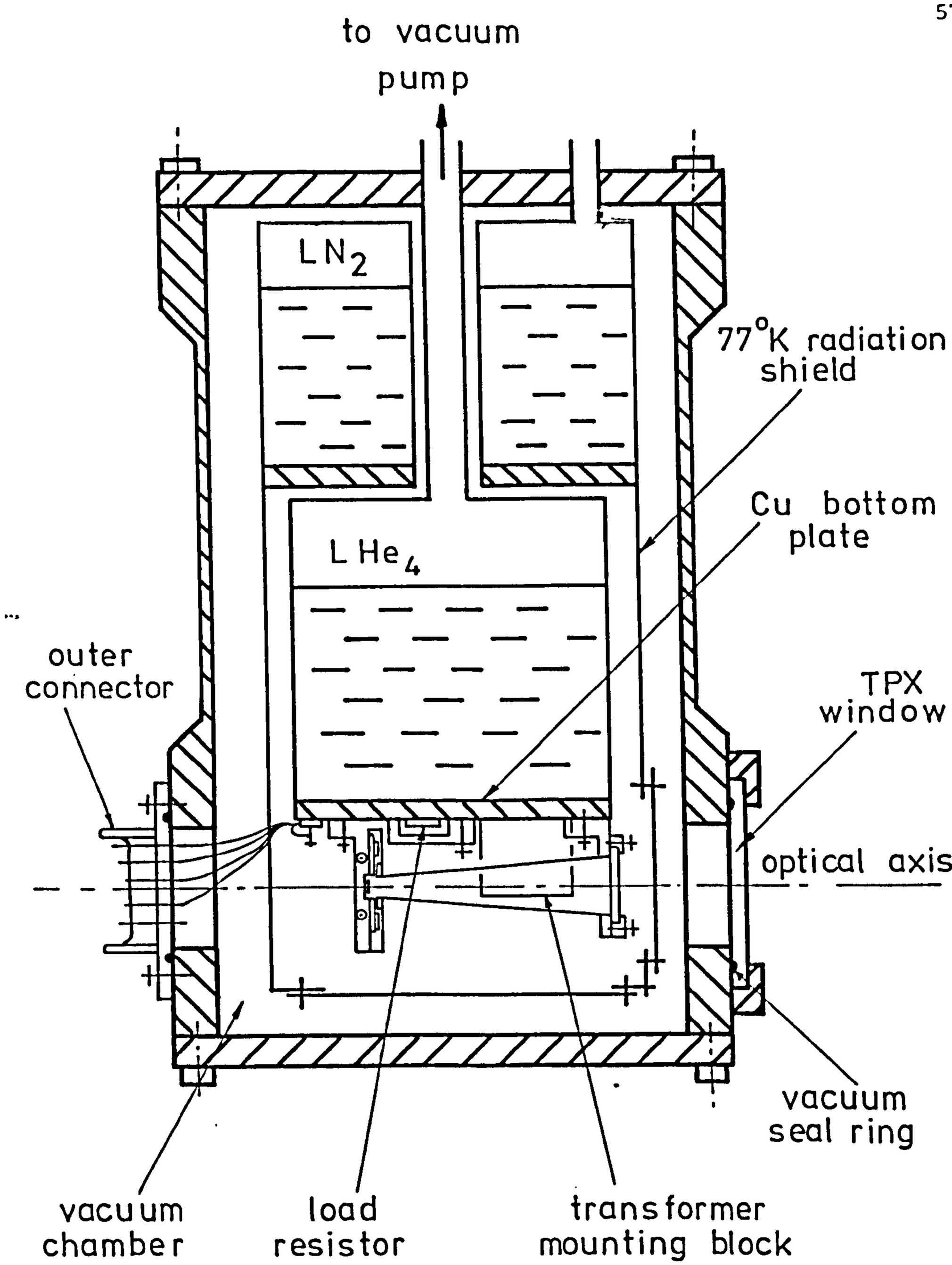

Figure 3.10. Detector assembly.

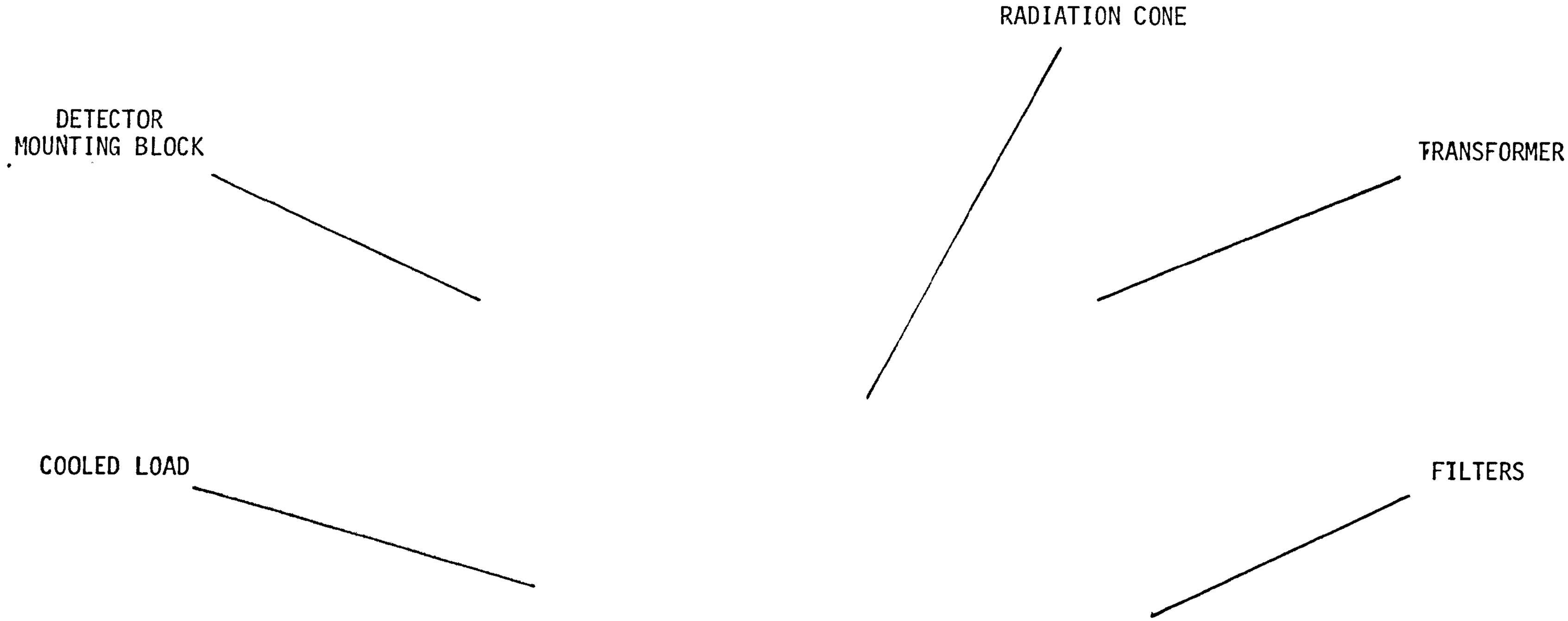

Plate 1. ^{4}He-cooled detector fittings.

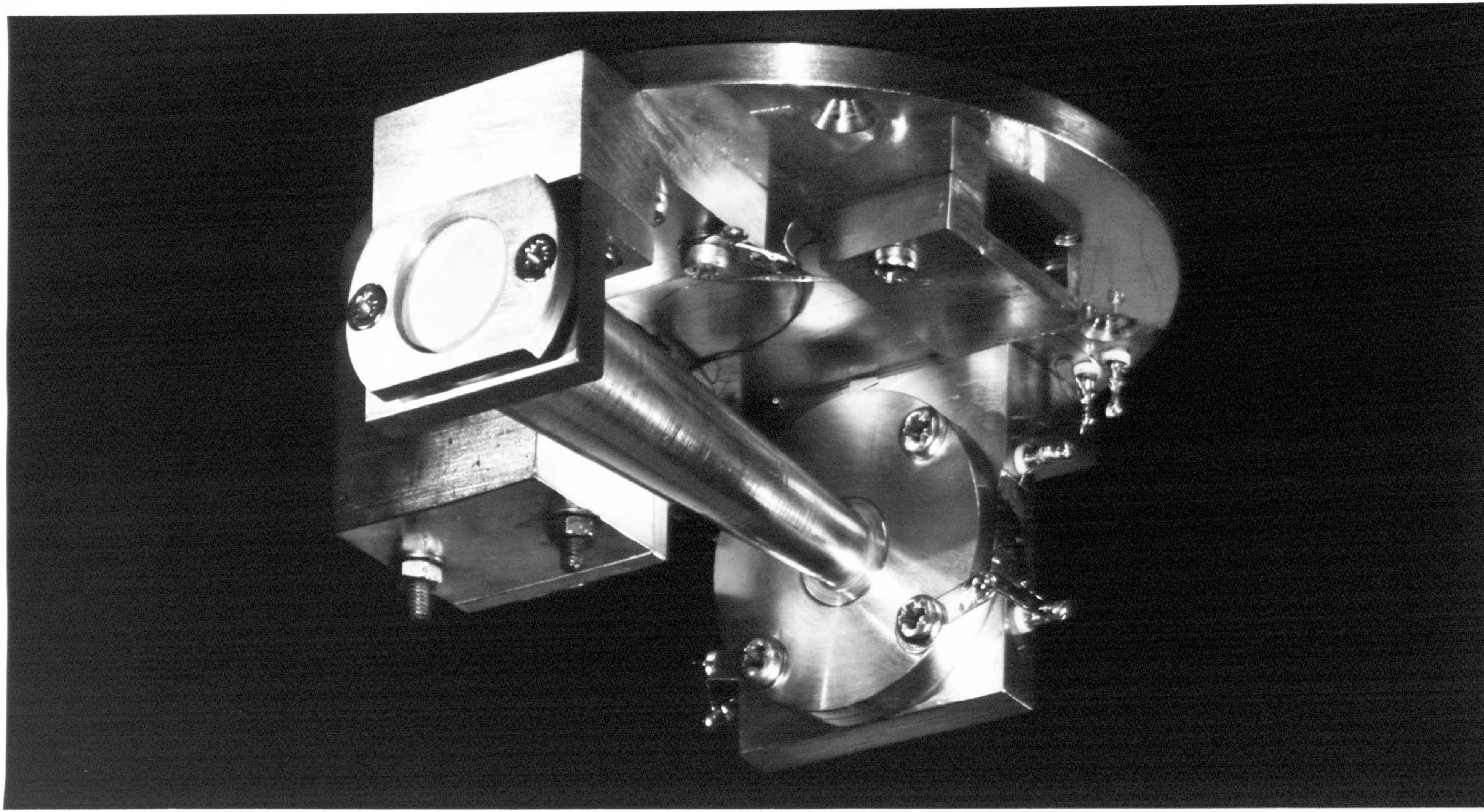

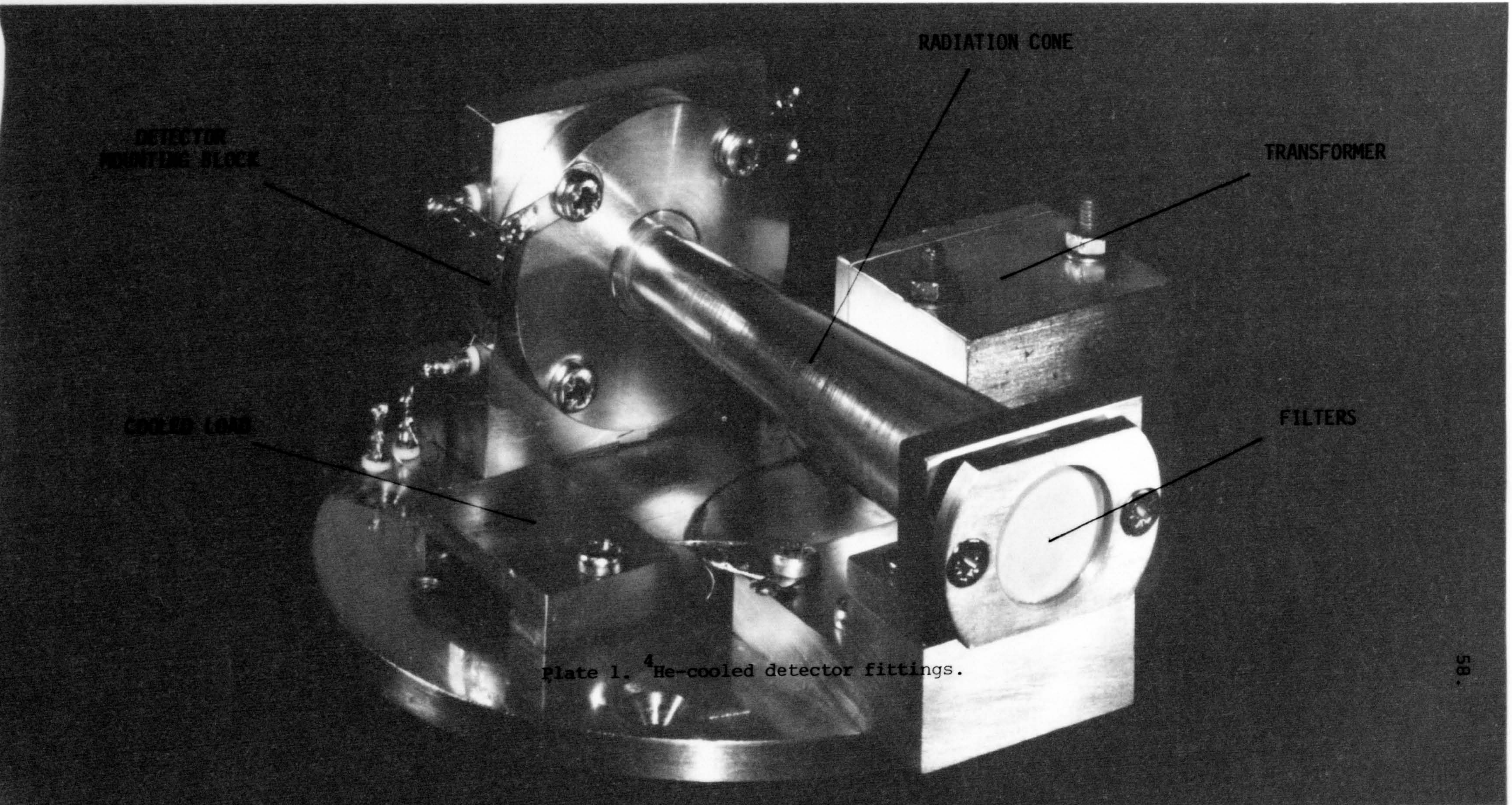

Plate 1. ^{4}He-cooled detector fittings.

were made using 40 s.w.g. enamelled copper wire firmly stuck down with G.E. varnish. All mating surfaces on the fittings and the cryostat base plate were lapped and smeared with silicon heat sink paste before bolting together to ensure good thermal contact. All fittings and the cryostat base plate were gold plated to give high reflectivity and good resistance to corrosion.

3.4.3 Cryostat ^{4}He heat sink temperature fluctuations at 3.7°K.

Cryostat heat sink temperature fluctuations could be divided into two categories:

(1) drifts or very low frequency fluctuations (i.e. << 1 Hz) outside the detector signal bandwidth,

(2) higher frequency fluctuations (i.e. > 10 Hz) in the signal bandwidth which would be seen as excess noise produced by a thermal detector mounted on the heat sink.

Heat sink fluctuations > 10 Hz

It was possible to obtain an upper limit for $\Delta T_{h.s.}(\omega)$ for ω > 10 Hz by measuring the excess noise (i.e. from all sources other than Johnson noise) produced by a d.c. biased Germanium (Ge) thermometer mounted on the ^{4}He heat sink of the cryostat. An upper limit for $\Delta T_{h.s.}(\omega)$ could be calculated by assuming the excess noise was entirely due to changes in resistance of the crystal produced by cryostat heat sink fluctuations. The crystal was cut from a Ge boule of donor concentration 3.5×10^{16} cm^{-3} as this doping level gives a very high temperature coefficient of resistance at 3.7°K. It was mounted on one surface of a piece of polished quartz with a small amount of G.E. varnish. The other surface of the quartz was stuck down to the cryostat heat sink with G.E. varnish also. This arrangement gave a time constant between the Ge crystal and the heat sink of

less than 1 m sec. The crystal was calibrated by measuring the vapour pressure above the surface of the ^{4}He using a mercury manometer reading to $\pm$ .5 mm. Hg. As the vapour pressure above the ^{4}He corresponds to a particular boil-off temperature, it is possible to obtain an R-T plot for the crystal. The crystal resistance at 3.70(3)^{o}K was 1.25 MΩ.

For the $\Delta T_{h.s.}(\omega)$ tests, the crystal was d.c. biased through a 2.5 MΩ cooled load resistor in series with a 1.0 volt battery. Using the manostat and manometer, it was possible to produce an R-V plot for the crystal in a temperature range around 3.7^{o}K. Fluctuations in the voltage across the crystal were amplified by an a.c. coupled input, low noise pre-amp. These fluctuations were then measured using an Ithaco 391A lock-in amplifier operated in its noise measurement mode, where the d.c. output of the lock-in amplifier is proportional to the true r.m.s. noise applied to its input within the set bandwidth. Knowing the pre-amp and lock-in amplifier gains, it was possible to calculate the excess fluctuations in voltage (i.e. above Johnson noise) across the crystal. This fluctuation in voltage could be converted into a temperature fluctuation using the R-V and then R-T plots for the crystal. The crystal used produced a voltage change of 4.032 V.^{o}K^{-1} at 3.70^{o}K. Figure (3.11) shows a plot of $\Delta T_{h.s.}(\omega)$ versus frequency. At frequencies greater than 100 Hz the excess noise was about the same as the Johnson noise and it therefore seems likely that most of the extra noise at lower frequencies was due to crystal current and contact noise.

Heat sink temperature drifts

Experiments performed to measure the cryostat heat sink temperature drifts employed the same Ge crystal and 2.5 MΩ load resistor used in

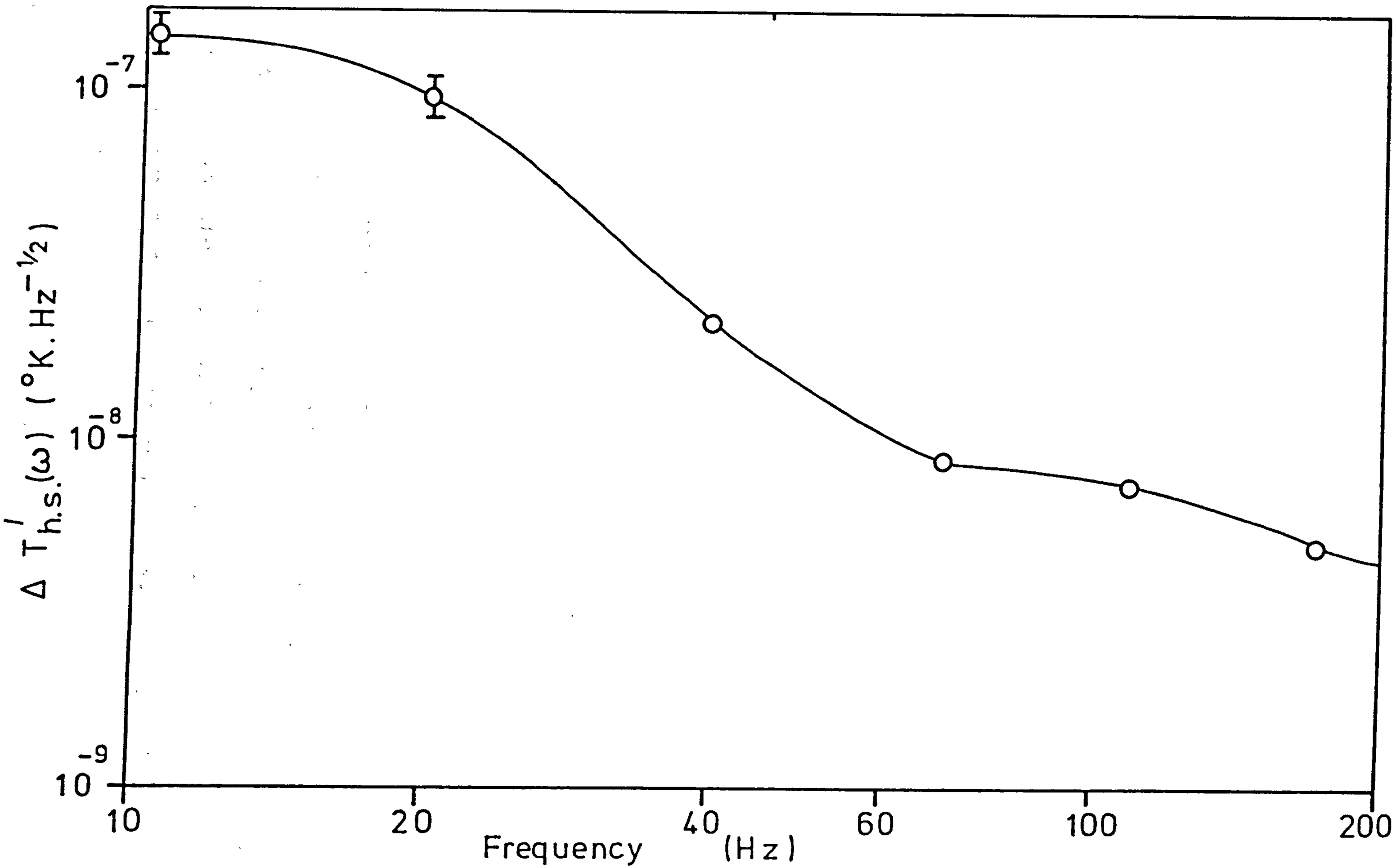

Figure 3.11. $\Delta T'_{h.s.}(\omega)$ versus frequency.

the experiments to measure higher frequency fluctuations. The calibration output of the lock-in amplifier was used to provide a very stable a.c. bias voltage across the crystal and its load resistor. Changes in the crystal temperature would therefore result in changes in amplitude of the a.c. bias voltage across it. The lock-in amplifier was set to its 'lo drift' mode and the voltage across the crystal fed directly into its input. Fluctuations in the a.c. voltage across the crystal were therefore registered as changes in the d.c. output of the lock-in amplifier. The output was calibrated using the manostat and mercury manometer to set the ^{4}He heat sink to a range of temperatures around 3.7^{o}K and noting the lock-in amplifier output reading at each temperature setting. Figure (3.12) shows the cryostat heat sink temperature drifts over a period of 15 minutes. The periodicity of the fluctuations (which was maintained indefinitely) is likely to have been caused by the action of the manostat keeping the temperature steady to within $\pm$ .5 m ^{o}K, i.e. regulating the pressure in the ^{4}He can to $\pm$ .25 mm. Hg. The time constant on the lock-in amplifier output was set to 4 seconds.

To ensure that these fluctuations on the lock-in amplifier output were only due to excess noise or changes in resistance of the crystal, the crystal was replaced by a cooled wire-wound resistor of approximately the same resistance. The fluctuation in the output of the lock-in amplifier was then < .1 mV, i.e. system output noise and drift would be equivalent to a temperature noise level of <.1 m ^{o}K in Figure (3.12).

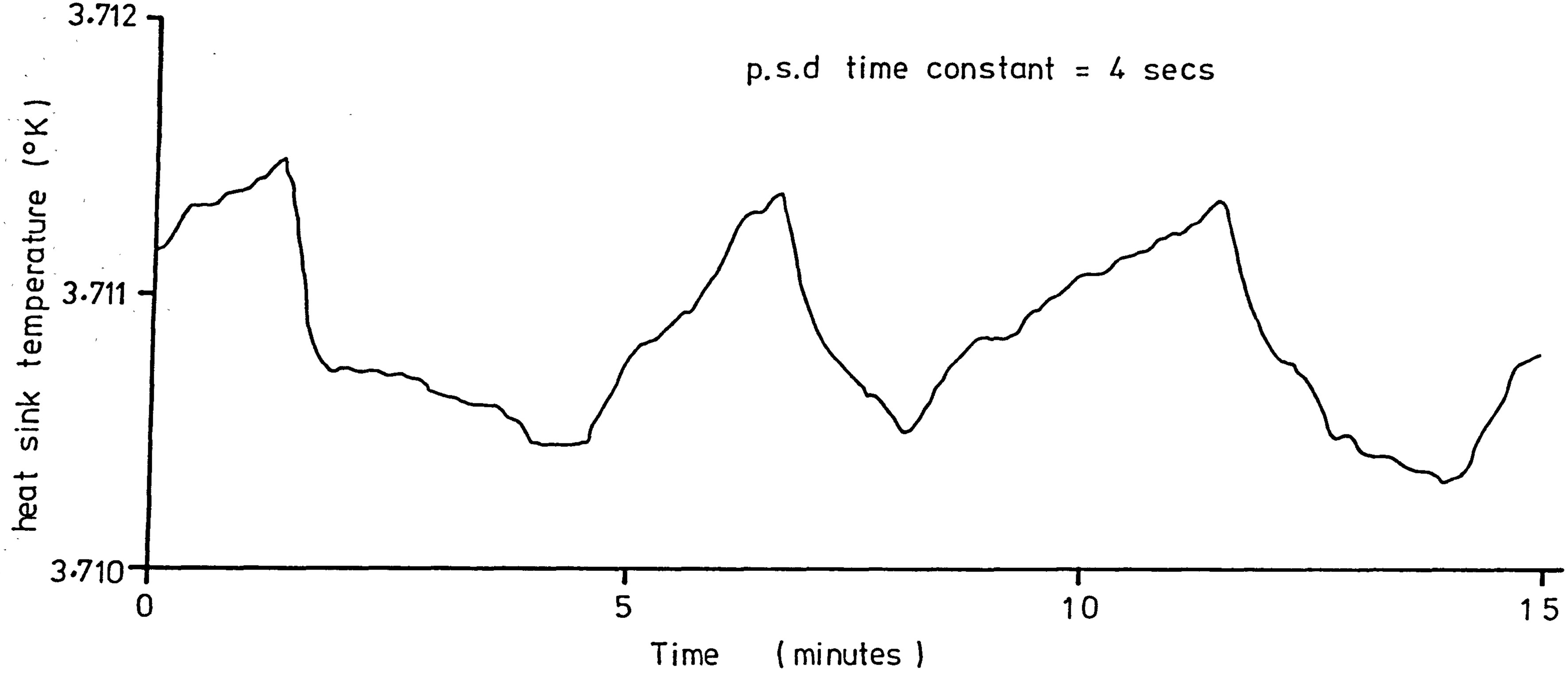

Figure 3.12. Cryostat heat sink drifts.

CHAPTER III

REFERENCES

(1) Dunn, M.S.F., 'Fabrication of Q.M.C. Superconducting Transition Edge Bolometers', Queen Mary College internal report No. RAG-80-01 (1980).

(2) Chanin, G., J. P. Torre and L. Peccoud, Infrared Phys. 18, 660 (1978).

(3) Johnson, V.J. (Ed.), "Properties of Materials at Low Temperatures: a Compendium", National Bureau of Standards Cryogenic Engineering Laboratory, U.S. Air Force contract No. 33 (616) 58-4 (1958-9).

(4) Reese, W. and J. E. Tucker, J. Chem. Phys. 43, 105 (1965).

(5) Fritzsche, M., J. Phys. Chem. Solids 6, 69 (1958).

CHAPTER IV

ABSORPTION OF RADIATION BY THE BOLOMETER SUBSTRATE

4.1 Introduction

A key parameter of the bolometer element is α, the fraction of the incident radiation power absorbed. This chapter describes a method of calculating α using a transmission line analogue (TLA) model. Figure (4.1a) shows the complete analogue, where Z_O and Z_S are the characteristic impedances of the transmission lines representing free space and the substrate. Z_F is a load impedance representing the absorbing film deposited on the substrate. As will be shown in section (4.2.2), greater absorption and the possibility of obtaining a flat absorption spectrum results if the film is deposited on the back surface, i.e. the surface away from the incident radiation.

It is shown in Appendix IV how the transmission line problem can be treated using the method of scattering coefficients for two cascaded two-port networks, one consisting of the dielectric interface between Z_O and Z_S and the other, the shunt impedance Z_F across the interface between Z_S and Z_O (see (Figure 4.1b)).

4.2 Comparison of TLA model computed spectra with experimental data

4.2.1 Comparison with room temperature data

(1) contains measured room temperature reflection and transmission data between 10 cm^{-1} and 190 cm^{-1} for a 163 Ω/sq. Bi film evaporated onto a 1 mm thick quartz substrate both for radiation incident on the quartz side and the Bi film side. These data were used to prove the validity of the TLA model.

Appendix V describes a computer program (program SUB) used to

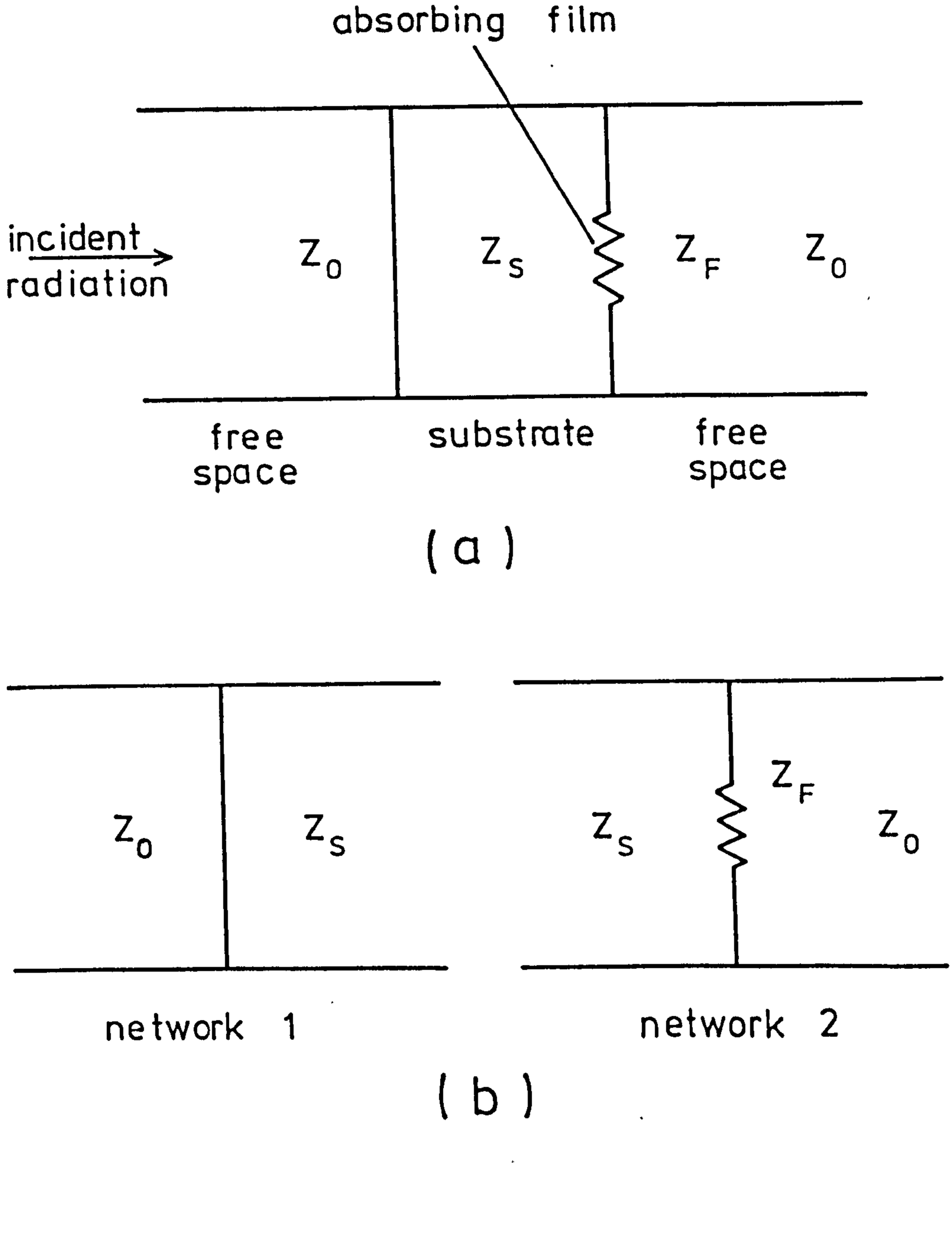

Figure 4.1. (a) the complete transmission line analogue model for an absorbing substrate; (b) the constituent two-port networks.

compute FIR transmission, reflection and absorption coefficients of dielectric substrates coated with absorbing metal films of known impedance per square. The program can be used to calculate coefficients for radiation incident on the film side or the dielectric side of the substrate. The data input required by the program includes the refractive indices and absorption coefficients of the dielectric for the frequency range of interest. For all computed spectra shown in this chapter, these values were obtained from [2].

Figure (4.2) reproduces the spectra given in [1]. The overlay shows the computed spectra produced by program SUB for transmission and reflection coefficients plotted with a 1 cm^{-1} stepping interval. For clarity, the narrowly spaced interference fringes on the computed spectrum have only been plotted for R' (i.e. reflection with radiation incident on the Bi film). The spacing of the fringes is 2 cm^{-1} as expected for a 1 mm thick substrate. T, R and T' (transmission and reflection coefficient spectra for radiation incident on the quartz side and the transmission coefficient spectrum for radiation incident on the Bi film respectively) give the spectra of the averaged values.

The measured spectra do not show the fringes, especially at higher frequencies for several reasons. One is that the resolution of the measured spectra was comparable with the fringe spacing. The fact that the surfaces of the sample could never be quite parallel would also reduce the interference fringes, the effect being greater for higher frequencies. The roughness of the sample would also tend to produce a fringeless spectrum at higher frequencies as once the surface roughness becomes comparable with the radiation wavelength, the interfaces between the substrate and free space are no longer sharp and a transmitted or reflected wave will not retain any plane-wave-like properties, in

Figure 4.2. Measured and computed (overlay) reflection and transmission spectra for a 1mm thick quartz substrate at room temperature coated with a 163 Ω/sq. Bi film.

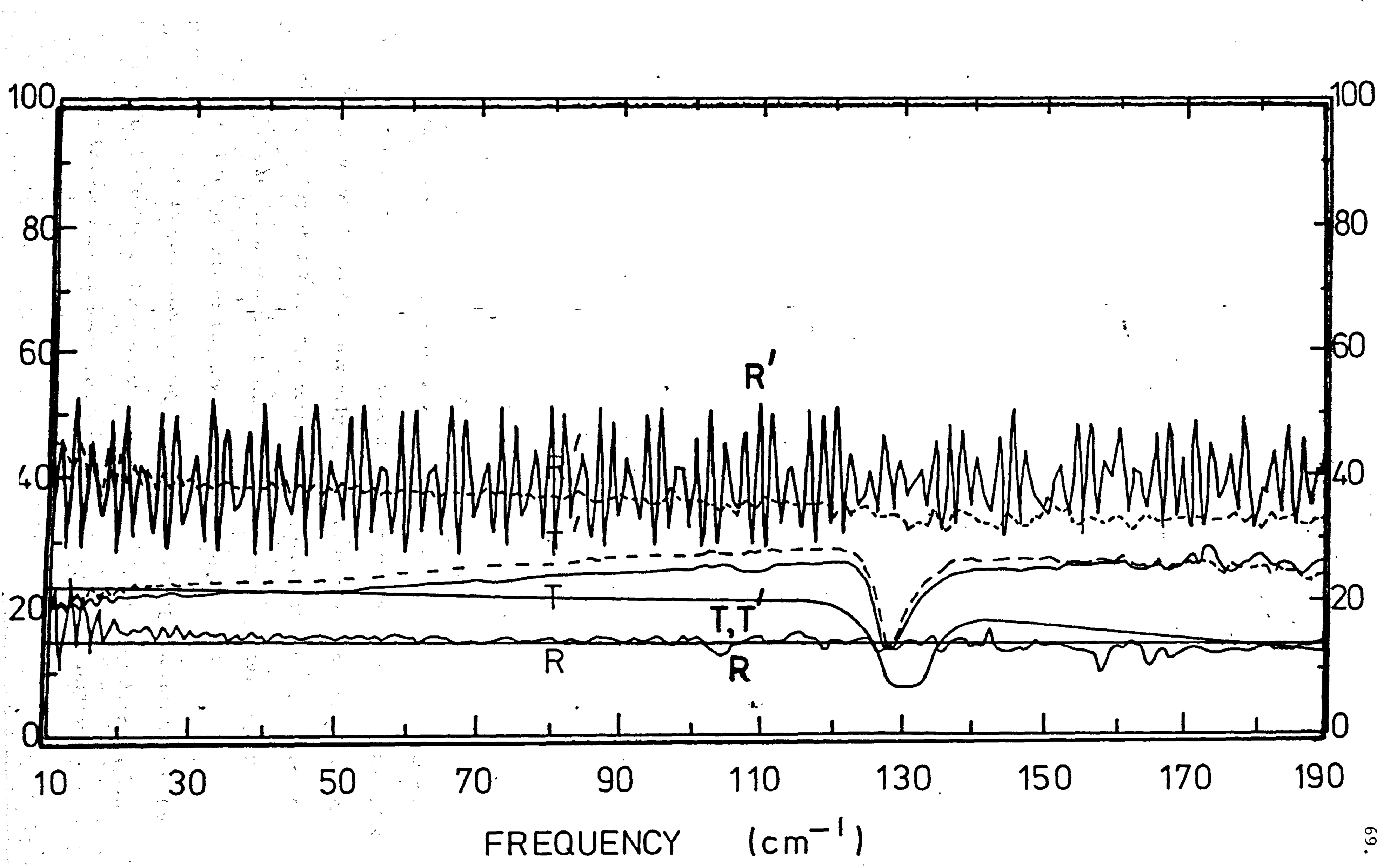
100
80
60
40
20
0
R′
T
T,T′
R
R
10
30
50
70
90
110
130
150
170
190
FREQUENCY (cm⁻¹)

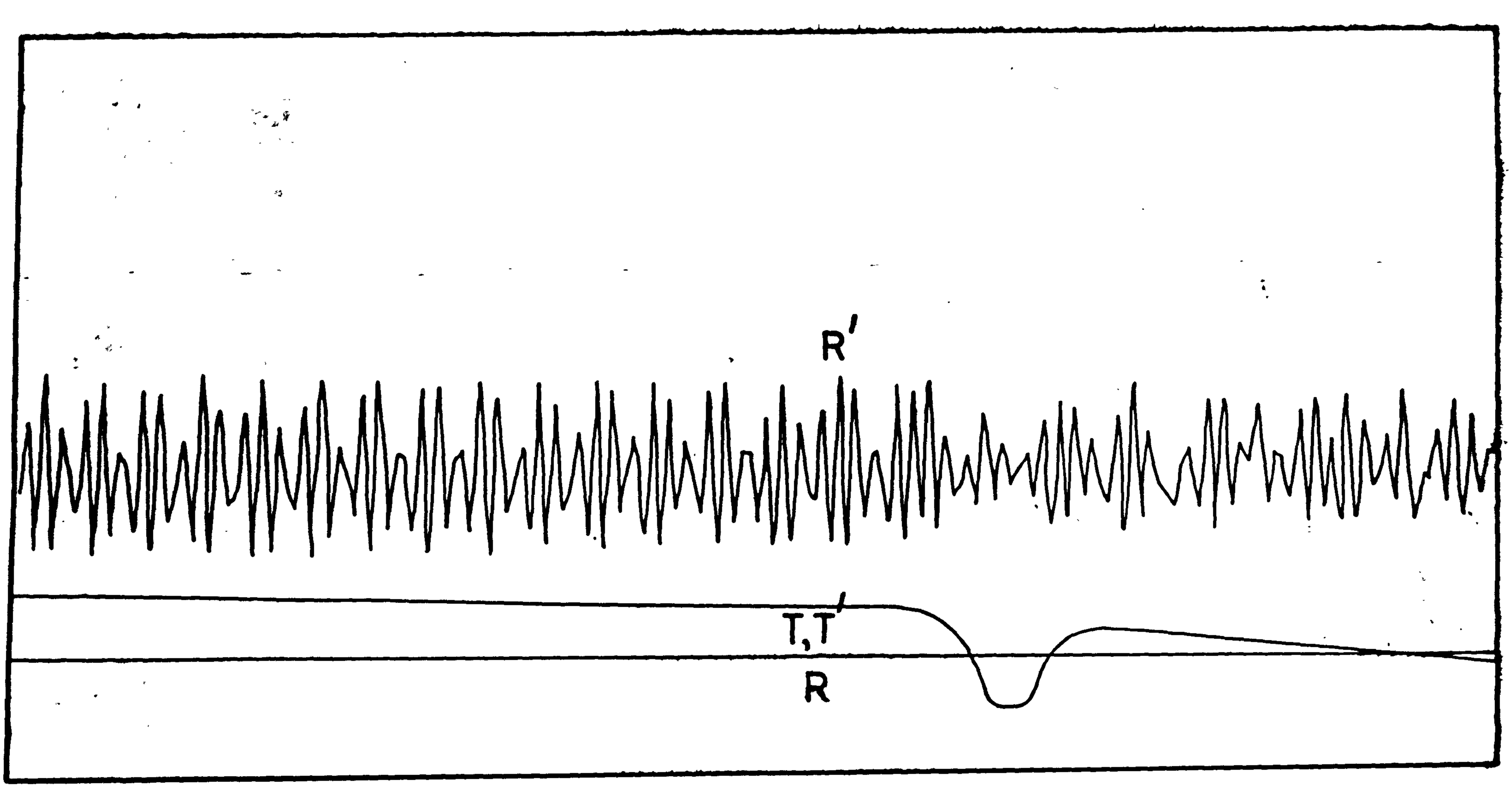

69.

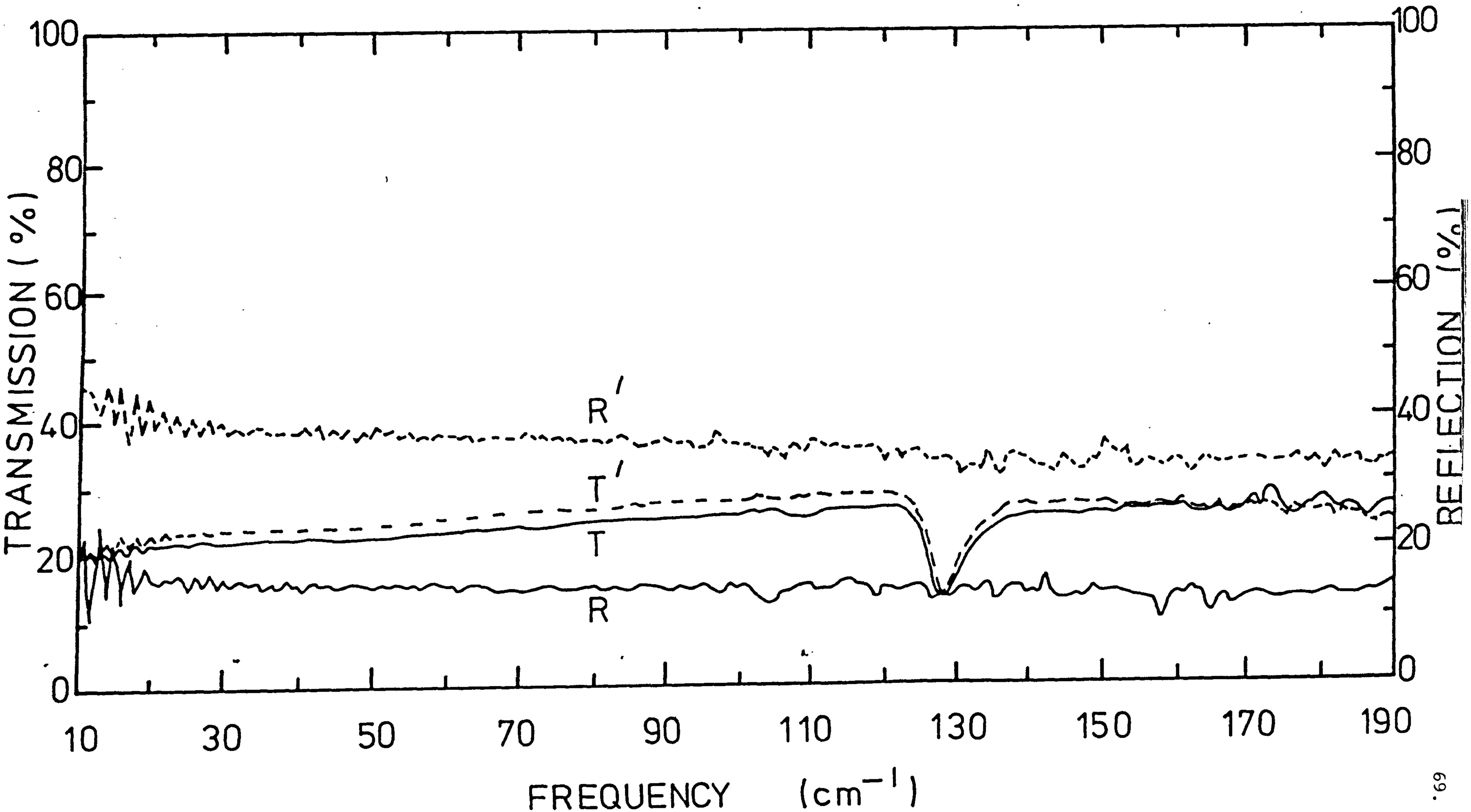
100
80
60
40
20
0
TRANSMISSION (%)
REFLECTION (%)
R'
T'
T
R
10
30
50
70
90
110
130
150
170
190
FREQUENCY (cm⁻¹)

particular constant phase in the x-y plane.

Another significant discrepancy between computed and measured spectra is that between computed and measured T and T'. The fact that the measured T and T' shows a rising characteristic with increasing frequency in spite of the increasing absorption of the quartz sample indicates that radiation was leaking around the edges of the sample. This effect will be more significant at higher frequencies because of diffraction effects.

In summary, the TLA model seems to give reasonable agreement with the experimental results and where discrepancies do occur, they appear to be due more to less than ideal conditions of measurement than any fundamental fault in the model.

4.2.2 FIR absorption of sapphire substrates coated with Bi films at ^{4}He temperatures

Figure (4.3) is a plot of the calculated absorption averaged over the interference fringes at 100 cm^{-1} of a 60 μm sapphire substrate at 1.5°K as a function of the impedance/square (R_{sq}) of the absorbing Bi film. Program SUB was used to provide computed absorption spectra for various R_{sq} between 40 and 550 Ω/sq. Input data for program SUB were taken from [2] and apply to sapphire at 1.5°K. It will be assumed, however, that these 1.5°K values are very nearly the same as the 3.7°K values which would be directly applicable to the substrate of a STEB operating at 3.7°K. The average absorption at 100 cm^{-1} for each of the film resistances was calculated from the spectra produced by SUB and used to plot the graph shown in Figure (4.3).

It is seen that for any R_{sq}, greatest absorption occurs when the radiation is incident on the uncoated surface of the substrate. In this case maximum absorption occurs for an R_{sq} of approximately 70 Ω/sq.

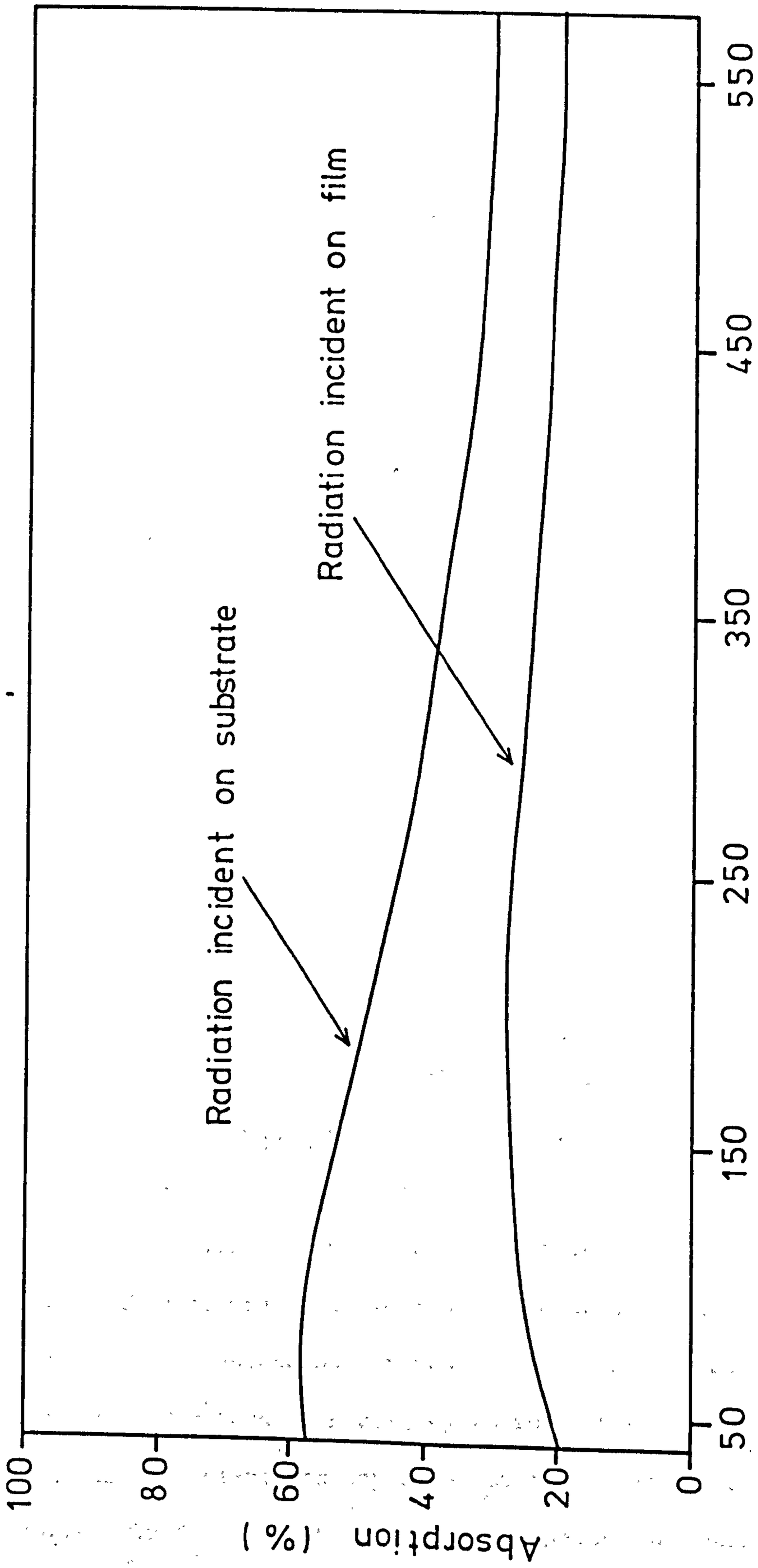
Radiation incident on film
Radiation incident on substrate
Absorption (%)
100
80
60
40
20
0
Film resistance per square (Ω/sq.)
50
150
250
350
450
550
Averaged absorption @ 100 cm^{-1} for a 60μm thick sapphire substrate at 1.5°K.

Figure 4.3. A

However a sapphire substrate will show very prominent Fabry-Perot fringes when coated with a film of this impedance due to reflection at the sapphire/Bi film/free space interface. This effect can be eliminated by choosing R_{sq} such that the parallel combination of the film impedance and free space matches the impedance of the sapphire, i.e. so that

$$\frac{1}{Z_S} = \frac{n}{Z_O} = \frac{1}{R_{sq}} + \frac{1}{Z_O}$$

$$\text{i.e.} \quad R_{sq} = Z_O/(n - 1)$$

where n is the refractive index and Z_S is the wave impedance of the sapphire substrate. Taking Z_O as 377 Ω and n as approximately 2.1 at 100 cm^{-1} shows that $R_{sq} \simeq 180$ Ω/sq. for a fringeless absorption spectrum. Figure (4.3) shows that the absorption of a sapphire substrate coated with a Bi film of impedance R_{sq} = 180 Ω/sq. results in only slightly less absorption than the maximum possible, i.e. 50% instead of 59%. The absorption spectrum given by SUB for this value of R_{sq} between 10 cm^{-1} and 200 cm^{-1} is not quite flat as the refractive index of sapphire varies slightly with frequency[2].

4.2.3 FIR transmission spectra measurements on Bi-coated sapphire substrates at 4.2°K

Section (4.2.1) has shown that the TLA model is capable of giving a reasonably accurate prediction of the absorption properties at room temperature of quartz substrates coated with absorbing Bi films. However it was thought necessary to show that the model was also applicable to Bi-coated sapphire detector substrates at ^{4}He temperatures. To do this FIR transmission spectra of sapphire substrates coated with Bi films were measured at 4.2°K and compared with computed

spectra using the TLA model.

Preparation of the samples

As the objective was to prove that the TLA model could predict the absorption properties of STEB substrates at ^{4}He temperatures, it was decided to use substrates similar to those used for the STEB's, i.e. approximately 60 μm thick sapphire substrates, 5 mm in diameter. The film resistances at ^{4}He temperatures were taken from measurements on films deposited on glass slides placed next to the substrates during evaporation. Tests on a number of Bi films with thicknesses between 250 Å and 2000 Å evaporated onto glass and sapphire substrates, showed that the factor by which the resistance of the Bi films increased between room temperature and 4.2°K was in the range 1.9 to 2.5, i.e. on average, 2.2 ± 15%. This factor appeared to be independent of the film thickness and the type of substrate.

Before evaporation the substrates were first thoroughly cleaned by agitating them for several minutes each in trichloroethylene, acetone and finally chloroform. They were then transferred to the holder (described in [3]) used for evaporating films onto detector substrates, mounted in the evaporator and pumped down as quickly as possible. The evaporation source used was a molybdenum boat loaded with spectrographically pure Bi. R_{sq} for the Bi film was monitored during the evaporation by measuring the resistance across a cleaned glass slide placed next to the substrate holder. Another cleaned glass slide was also laid next to the substrate for thickness measurements. For this purpose the slide was partially covered by another slide, which when removed after evaporation, left a straight step-edged film on the surface of the slide underneath. The source used for the evaporations was a molybdenum boat loaded with spectrographically pure

Bismuth. Evaporations were carried out at pressures of 10^{-5} Torr and rates of approximately 50 Å/sec.

Film thickness measurement

Thickness measurements were made on the step-edged film deposited on the half-coated glass slide using the following multiple beam interferometry technique:

A Watson 6 mm objective with an interference arrangement containing a monochromator, collimator, beam splitter and reference mirror was employed. The optical arrangement is shown in Figure (4.4). The resulting interference fringes viewed through the microscope graticule eyepiece were shifted at the film step-edge due to phase shifts caused by the film thickness. The film thickness t is given by

$$t = \frac{\text{fringe shift}}{\text{fringe spacing}} \times \frac{\lambda}{2}$$

where λ is the wavelength of the illuminating light (approximately 5000 Å for the green filter used with the white light source). Where the fringe shift was greater than the fringe spacing, it was necessary to use white light, when fringes of equal chromatic order could be traced across the step. This technique was quick and easy but gave an error of approximately ± 100 Å.

For films of thickness less than 500 Å, the Fizeau Fringes method using a multiple beam was used[4]. Using films evaporated onto standard glass slides it was possible to obtain film thickness measurements accurate to ± 25 Å.

4.2.4 Transmission measurements on Bi-coated sapphire substrates at $4.2^{\circ}K$

The $4.2^{\circ}K$ transmission measurements on the Bi-coated sapphire substrates were made with a polarising Michelson interferometer based

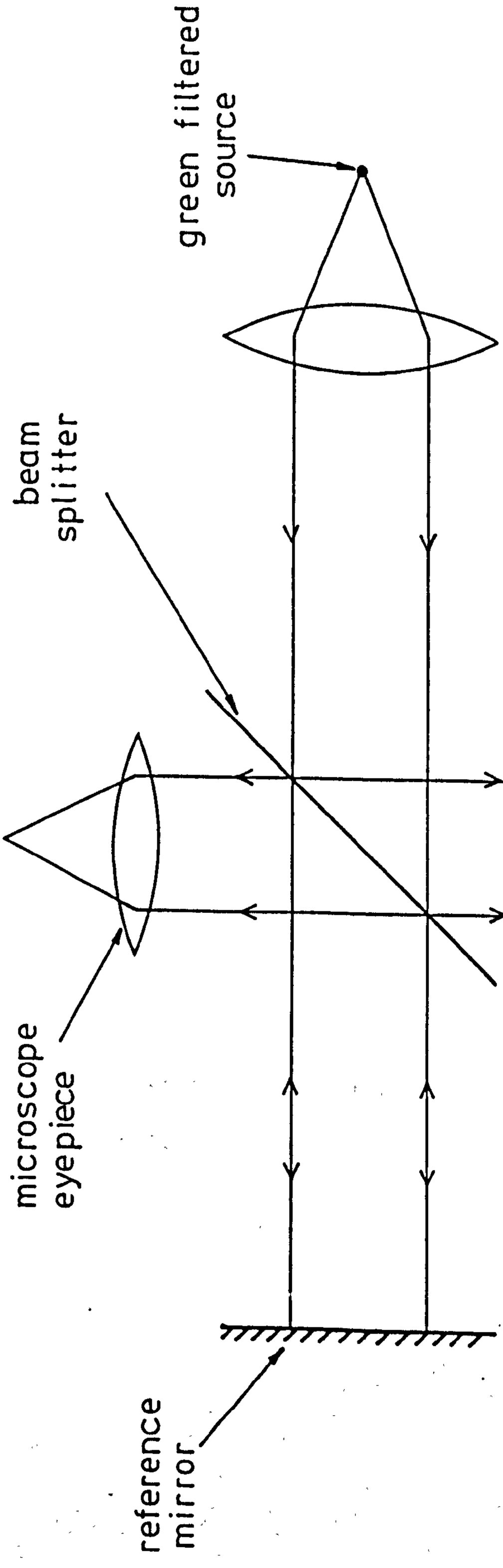

Figure 4.4. Film thickness measurement for films greater than 500 Å thick.

on a Research and Industrial Inst. Co. FS-720 Fourier Spectrophotometer module using a 10 μm wire beam splitter. The sample was mounted in an Oxford Instruments continuous flow cryostat positioned in the interferometer so that the sample was situated at the focus of the interferometer beam. The detector used for the FIR radiation transmitted through the sample was a ^{4}He-cooled Germanium bolometer with a radiation NEP of $\simeq 3 \times 10^{-13}$ W.Hz$^{-\frac{1}{2}}$.

All transmission measurements were made with the radiation incident on the uncoated surface of the substrate. The transmission spectra for the frequency range 20 cm^{-1} to 90 cm^{-1} of three samples are shown in Figure (4.5). From Section (4.2.2) the value of R_{sq} which will give fringeless transmission spectra is $\simeq$ 180 Ω/sq. One of the samples was coated with a film with an impedance very close to this value, i.e. $R_{sq} \simeq 200$ Ω, and it is seen that the transmission spectrum is indeed nearly flat. The other two samples have values of R_{sq} relatively far removed from the value need for a flat transmission characteristic resulting in distinct fringes. The slight discrepancies between computed and measured spectra in fringe spacing and phase are caused mainly by the error in the value of the substrate thickness used in the computed spectra due to the tolerance in the thickness specification of the substrates.

Figure 4.5. Measured and computed transmission spectra of sapphire substrates at ≈4.2°K coated with Bi films for radiation incident on the uncoated surfaces of the substrates.

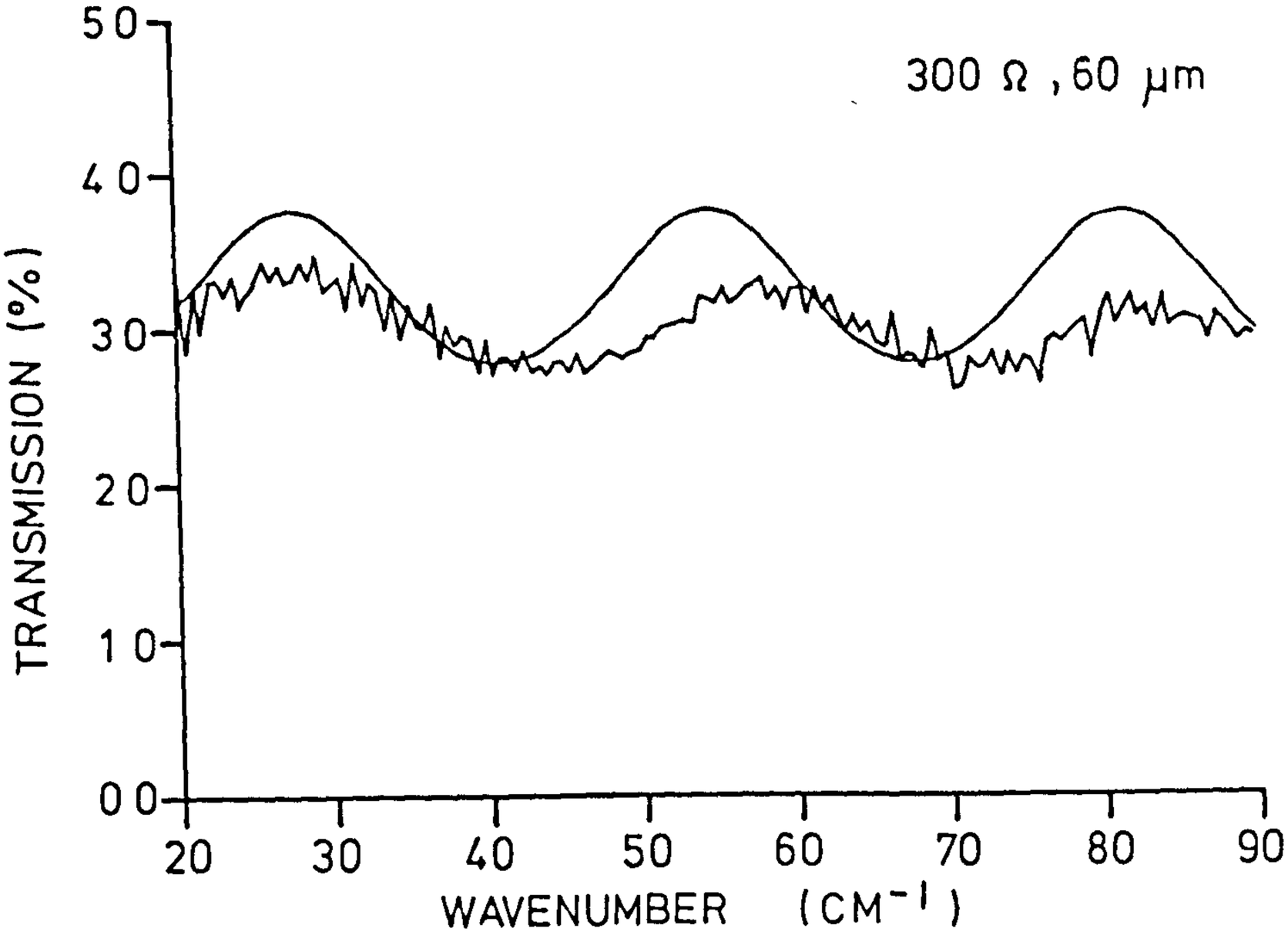
300 Ω , 60 μm
TRANSMISSION (%)
50
40
30
20
10
00
20
30
40
50
60
70
80
90
WAVENUMBER (CM⁻¹)

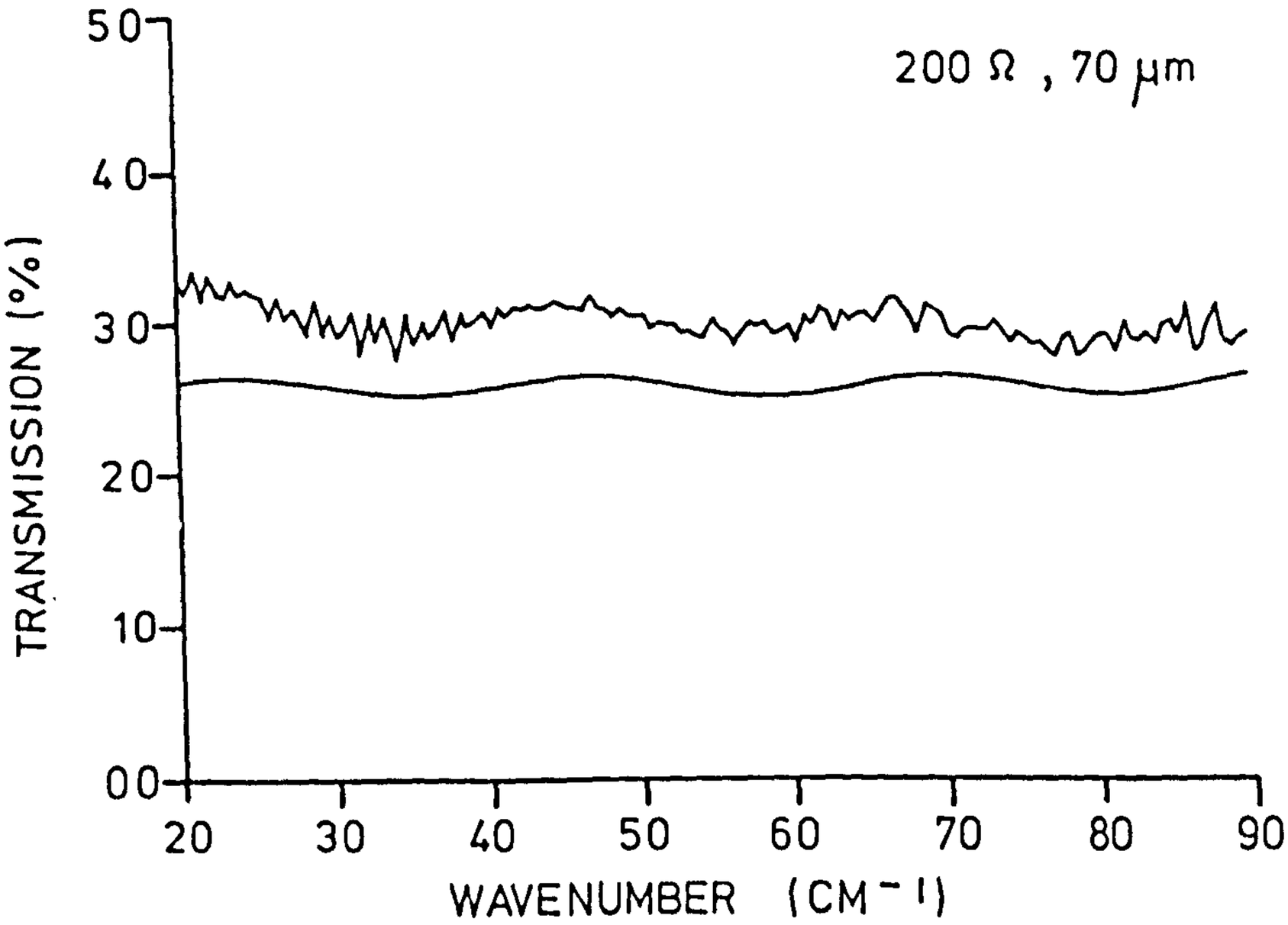
200 Ω , 70 μm
TRANSMISSION (%)
50
40
30
20
10
00
20
30
40
50
60
70
80
90
WAVENUMBER (CM⁻¹)

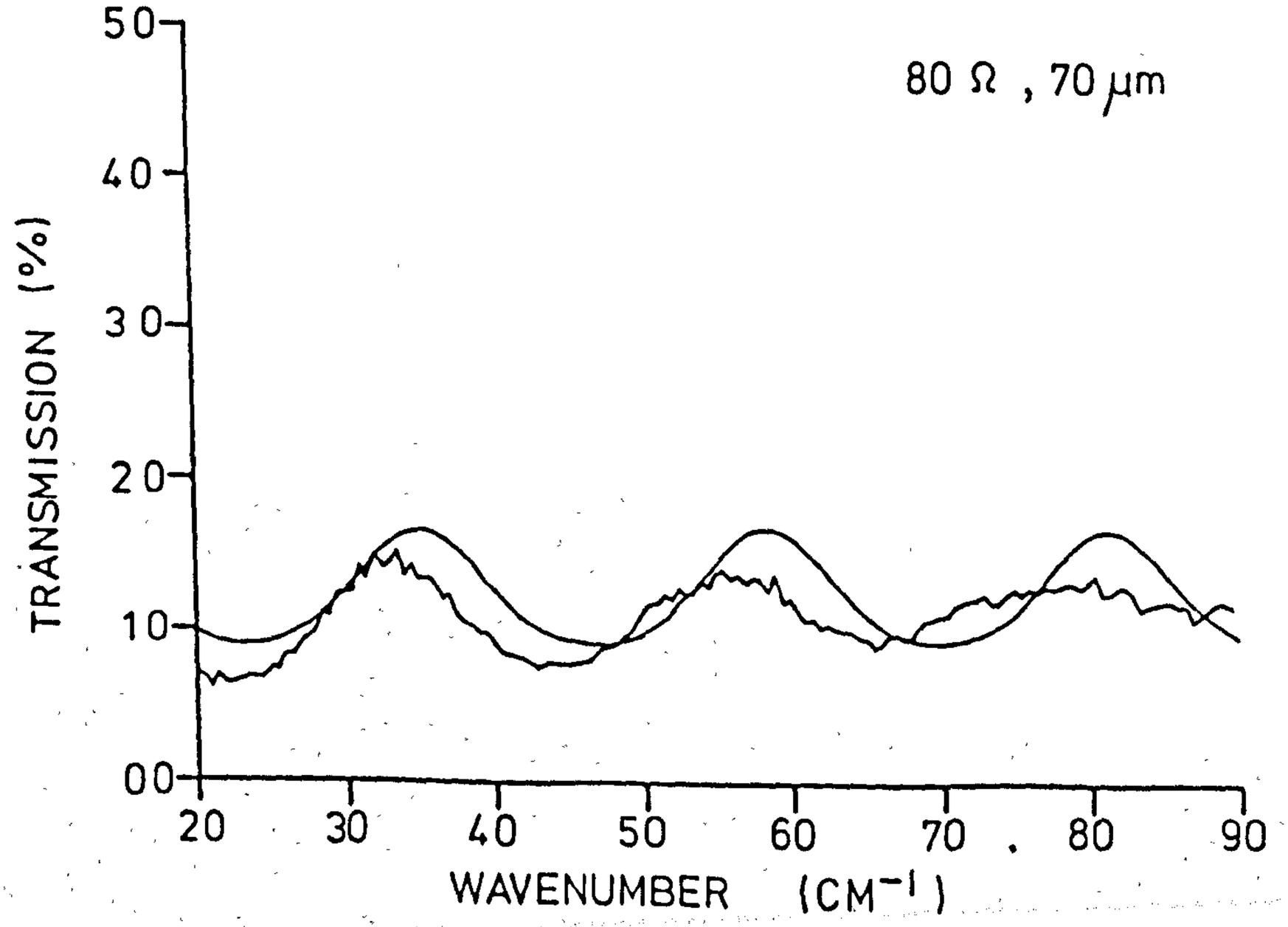
80 Ω , 70 μm
TRANSMISSION (%)
50
40
30
20
10
00
20
30
40
50
60
70
80
90
WAVENUMBER (CM⁻¹)

CHAPTER IV

REFERENCES

(1) El-Atawy, S.A. and P. A. R. Ade, Infrared Phys. 18, 683 (1978).

(2) Loewenstein, E.V., D. R. Smith and R. L. Morgan, Appl. Opt. 12, No. 2, 398 (1973).

(3) Dunn, M.S.F., 'Fabrication of Q.M.C. Superconducting Transition Edge Bolometers', Queen Mary College internal report No. RAG-80-01 (1980).

(4) Chopra, K.L., "Thin Film Phenomena" published by the McGraw-Hill Book Co. (1969).

CHAPTER V

BOLOMETER TESTS

5.1 Introduction

In this chapter the methods used to measure the detector element parameters and the performance of the complete bolometer system are described; the results are compared with the theory derived in Chapter II. Results are quoted for two of the detectors produced and these will be referred to as the No. 2 and No. 3 detectors. The No. 2 detector element was characterised by a poor Sn deposition which seriously degraded the noise performance and gave a rather broad superconducting transition. Results from the No. 2 detector tests have therefore been quoted on a restricted basis, mainly in connection with servo-system performance.

5.2 Measurement of element parameters

5.2.1 R-T characteristic of the Sn sensor at the superconducting transition

The method used to measure the resistance of the Sn sensor is shown in Figure (5.1a). R_L is a room temperature load resistor which, together with the oscillator, forms a constant a.c. current supply for R_{Sn}. The voltage across R_{Sn} is amplified and measured on a digital volt-meter (DVM). Hence the reading on the DVM is directly proportional to R_{Sn}, which can therefore be calculated as the oscillator output, R_L and the amplifier gain are all known. The bolometer element can be taken through its superconducting transition using the manostat. The pressure in the ^{4}He can was measured at each manostat setting with a mercury manometer accurate to $\pm$ .5 mm. Hg. Hence a plot of R_{Sn} versus

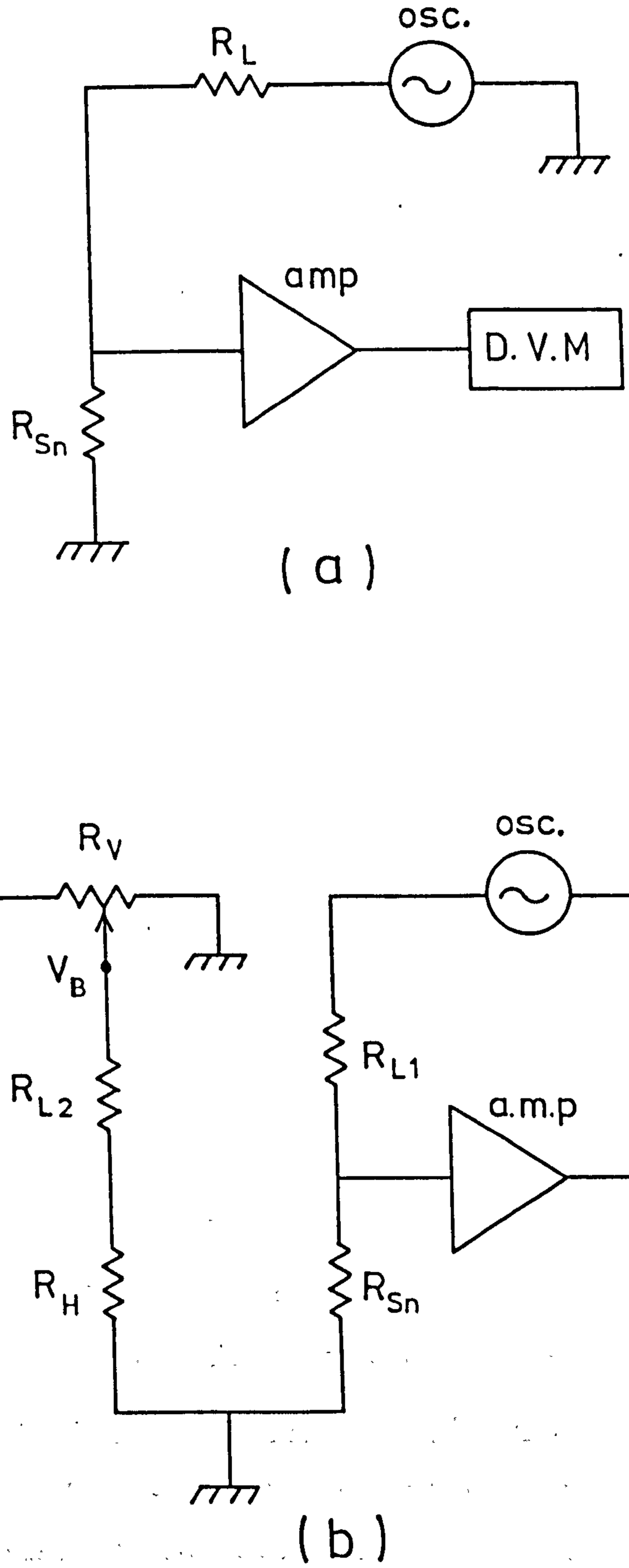

(a)

(b)

Figure 5.1. (a) transition temperature measurement;
(b) measurement of G.

T can be made if the element is assumed to be at the same temperature as the cryostat heat sink.

It is important to make sure that the a.c. bias current through the Sn sensor does not significantly raise the temperature of the element, otherwise the value for T_c will be inaccurate. This can be done by repeating the experiment for a lower oscillator output and ensuring that the value of R_{Sn} calculated remains the same.

Figure (5.2) shows the R_{Sn} versus T and β versus T characteristics of the No. 3 detector element at the superconducting transition. The transition temperature T_c, which is defined as the temperature at which the Sn film has half its normal resistance, is seen to be approximately 3.62°K whereas the value of T_c for the pure bulk material is 3.72°K. This discrepancy was thought to have been caused by slight differences in temperature between the bolometer mount and the ^{4}He can heat sink due to thermal resistances between mated surfaces of the bolometer mount and fittings rather than any thin film phenomena. The reason for this was that T_c measurements on Sn films of the same thickness evaporated onto glass slides stuck down directly to the cryostat heat sink and covered with radiation shields milled from solid high conductivity blocks gave values of T_c very close to 3.72°K.

5.2.2 Measurement of the thermal conductance G

For this measurement it was necessary to measure the change in element temperature (ΔT) for a given change in thermal power (ΔP) supplied to the element. As $\Delta P = G\,\Delta T$, G can then be calculated. For temperatures around T_c, the element temperature could be measured by measuring the Sn resistance in the same way as in the R-T transition tests and finding the temperature from the R-T plot. Power was supplied to the element by passing a d.c. current through the Bi

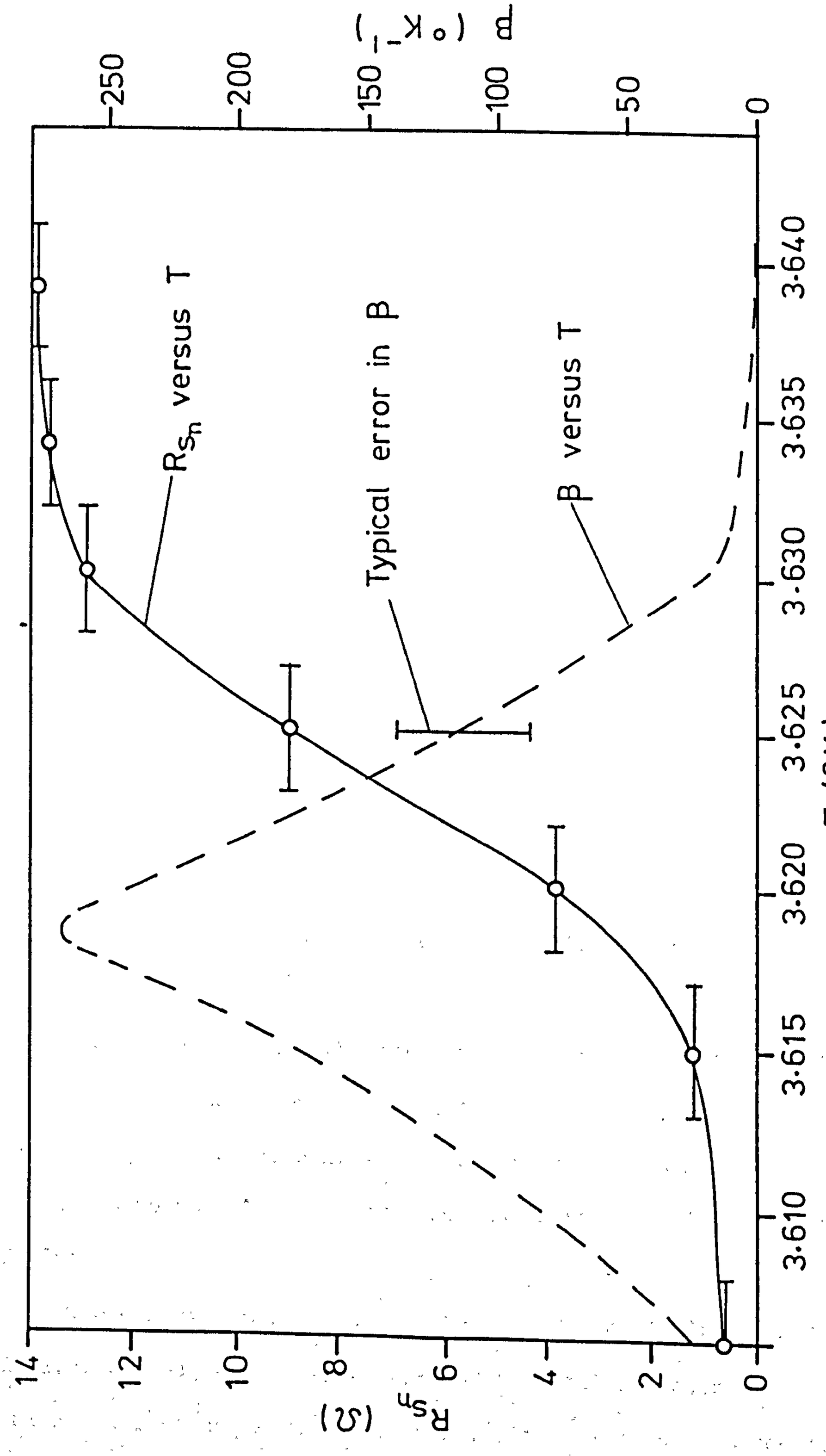

Figure 5.2. Plot of R_{Sn} and β versus T for the No. 3 element.

heater. The experimental set-up is shown in Figure (5.1b). The power supplied through the Bi heater was varied using the pot R_V. If the voltage across R_{L2} is decreased from V_{B1} to V_{B2} using R_V, then for $R_{L2} >> R_H$

$$G = (V_{B1}^2 - V_{B2}^2) \frac{R_H}{\Delta T . R_{L2}^2}$$

The value of G found using the above method was

$$G = 1.6 \pm .3 \ \mu W.^{o}K^{-1}$$

The error was caused by the error in measuring ΔT due to the $\pm$ .5 mm. Hg resolution of the mercury manometer.

5.2.3 Measurement of the element time constant τ_B

For this measurement use was made of the fact that the R-T characteristic of the Sn sensor is approximately linear around the mid-point of the transition (see Figure (5.2)).

If a known power is supplied instantaneously to the element then, provided the temperature of the element remains in the linear region, the time constant of the element will be given by the time taken for R_{Sn} to change by $1 - {}^{1}/_{e}$ of the total eventual change. This method was chosen, rather than the more obvious method of measuring the frequency response of the element and assuming a transfer function of $(1 + \omega^2 \tau_B^2)^{-\frac{1}{2}}$, because it was much quicker and therefore less affected by drifts in bolometer temperature caused by heat sink temperature drifts.

The experimental set-up is shown in Figure (5.3). The Sn sensor is a.c. biased by the oscillator and the load resistor R_{L1}. The voltage across R_{Sn} is proportional to its resistance in the linear region of the R-T characteristic. This voltage is amplified and then

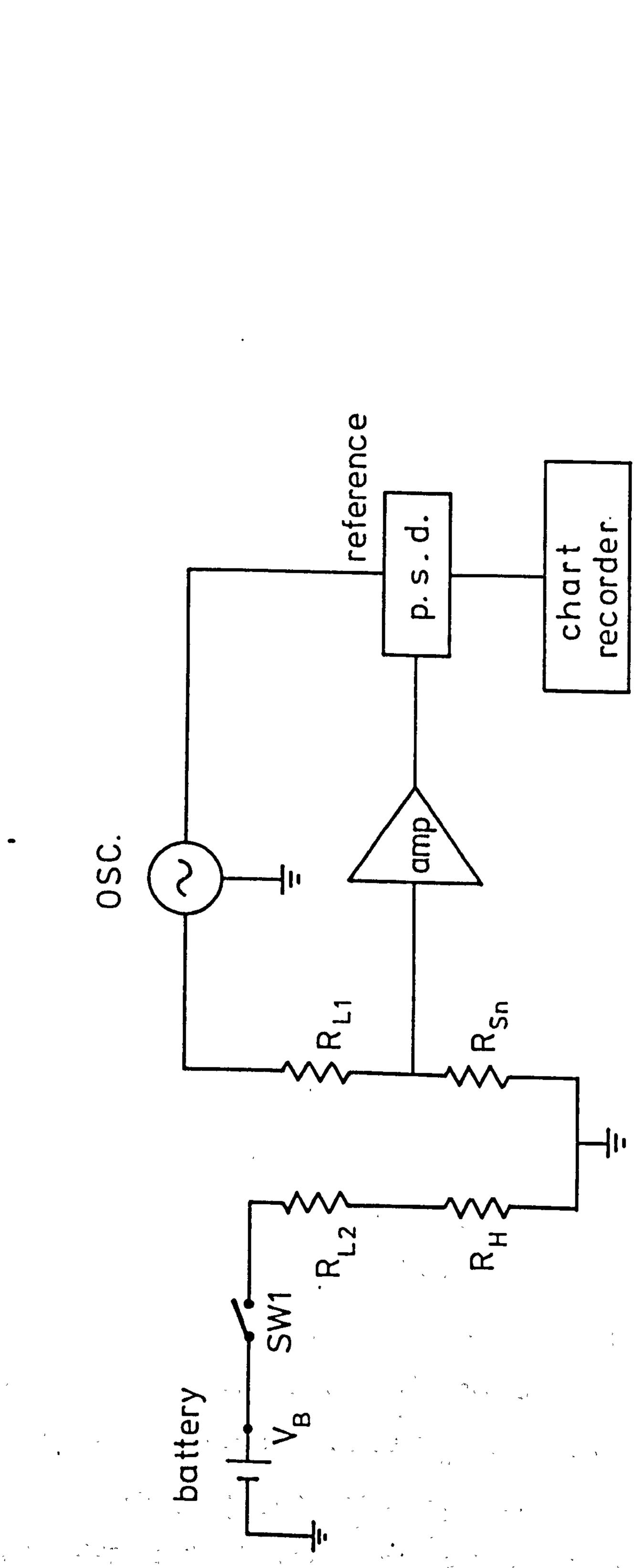

Figure 5.3. Measurement of bolometer time constant.

fed into a p.s.d. referenced to the bias frequency. The output of the p.s.d. is read off a chart so that the chart reading is proportional to the element resistance. Closing SW1 supplies a step input power to the element. The time taken for the p.s.d. output to change by $1 - {}^{1}/_{e}$ of its final change corresponds to τ_B. The value of the element time constant given by this method was

$$\tau_B = 1.5 \pm .1 \text{ secs}$$

The time constant applied to the output of the p.s.d. was 30 msec and would therefore have had a negligible effect on the measurement of τ_B.

Element thermal capacity C

As $C = G\,\tau_B$, then for $G = 1.6\ \mu W.{}^{o}K^{-1}$ and $\tau_B = 1.5$ secs

$$C = 2.4 \times 10^{-6}\ J.{}^{o}K^{-1}$$

5.3 Servo-system performance

5.3.1 Servo-system

The principles of operation of the servo loop have already been described in Chapter II. The servo circuit is shown again in Figure (5.4). The signal p.s.d. is used to monitor the output of the servo-system at the signal (modulation) frequency. The battery V_B, pot VR1 and R_{dc} effectively provide additional d.c. offset to the p.s.d. output. The signal oscillator and bias resistor R_S provide a means of modulating the feedback current I_F enabling the servo output to be calibrated.

The radiation power ΔP absorbed by the element which would produce a change equivalent to I_S in I_F is found from the following:

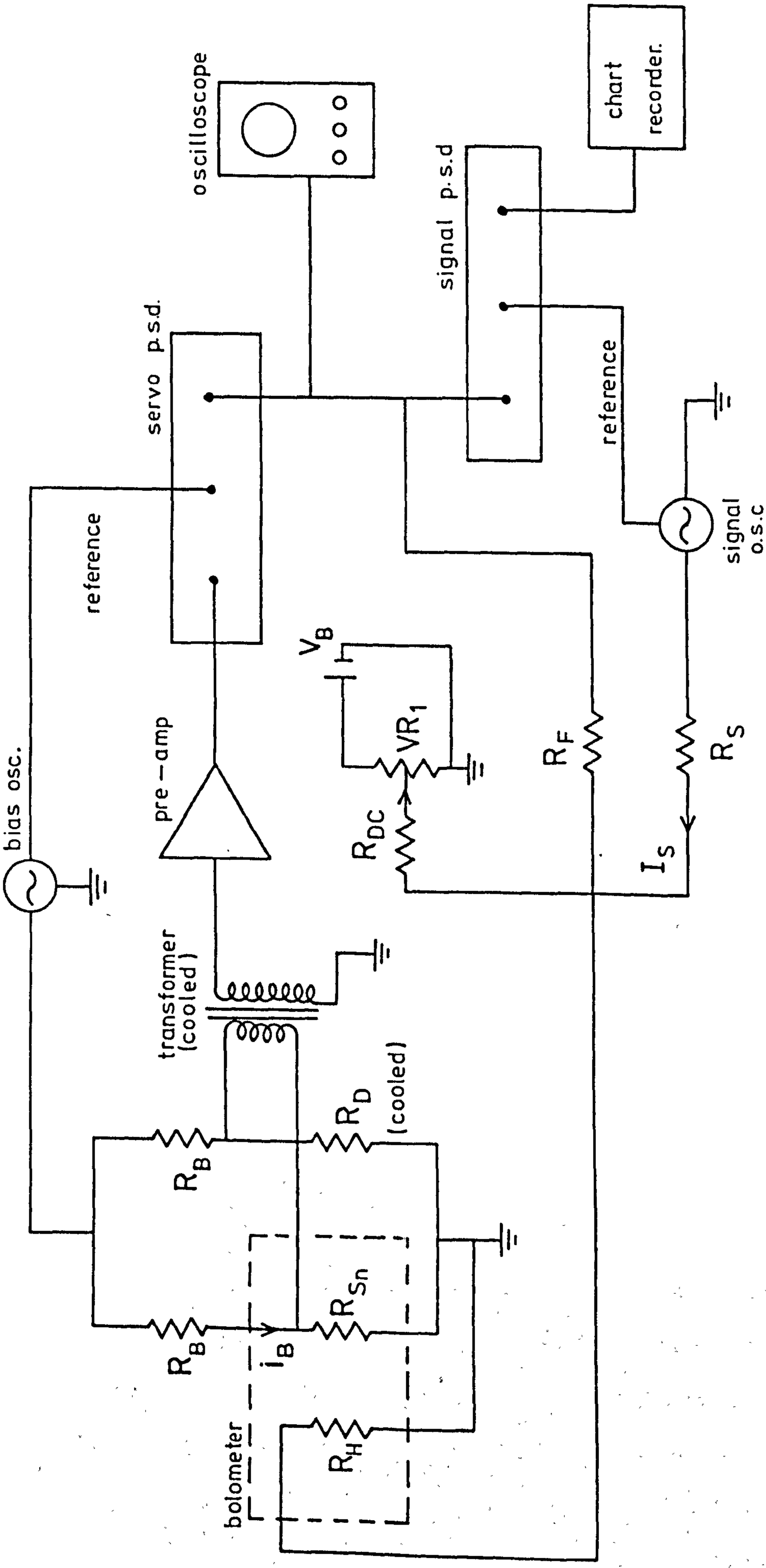

Figure 5.4. Detector electronics.

As the total power supplied to the element must remain constant

$$\Delta P + (I_F(O) - I_S)^2 R_H = I_F^2(O) R_H$$

where $I_F(O)$ is the no-signal feedback current. If $I_S << I_F(O)$

$$\Delta P + (I_F^2(O) - 2I_F(O) I_S) R_H = I_F^2(O) R_H$$

therefore $$\Delta P \simeq 2I_F(O) I_S R_H \quad \ldots (5.1)$$

and $$I_S \simeq \frac{\Delta P}{2I_F(O) R_H} \quad \ldots (5.2)$$

As the servo output is the voltage produced across R_F by I_S, i.e. $\Delta V_O = I_S R_F$

$$\Delta V_O \simeq \frac{\Delta P R_F}{2I_F(O) R_H} \quad \ldots (5.3)$$

showing that for small signals ΔV_O is a linear function of the power input to the detector. Therefore, provided the absorbed signal power is small compared with the standing bias power dissipated by R_H, the servo-system gives a linear output without the use of a square-rooting circuit, which could seriously limit the dynamic range of the detector. Note that ΔP is in fact a time-varying quantity (e.g. a modulated absorbed radiation power). Equation (5.3) also shows that the calibration of the detector is affected by drifts in $I_F(O)$. $I_F(O)$ is essentially the current which produces a power dissipation in R_H to raise the temperature of the element from the heat sink temperature to the bolometer operating temperature. The drift in $I_F(O)$ due to heat sink temperature fluctuations is equivalent to a fluctuation $\Delta I_F(O)$ in $I_F(O)$. The magnitude of $\Delta I_F(O)$ is such as to produce a change in power dissipated by R_H to compensate for the heat sink fluctuations. If the bolometer time constant τ_B is very much smaller than the

periodicity of the heat sink temperature drifts (as is the case - see section (3.4.3)), then from Equation (5.1), if $\Delta I_F(O) << \overline{I_F(O)}$, where $\overline{I_F(O)}$ is the average quiescent bias current through R_H,

$$\Delta I_F(O) \simeq \frac{\Delta P_H}{2\overline{I_F(O)}\ R_H}$$

Therefore the fractional drift in $I_F(O)$ will be

$$\frac{\Delta I_F(O)}{\overline{I_F(O)}} \simeq \frac{\Delta P_H}{2\overline{I_F(O)}^2\ R_H} = \frac{\Delta P_H}{2\overline{P_H}}$$

where $\overline{P_H}$ is the average power dissipated by R_H.

For $\overline{I_F(O)} - \frac{\Delta I_F(O)}{2} < I_F(O) < \overline{I_F(O)} + \frac{\Delta I_F(O)}{2}$ the limits of V_O due to drifts in $I_F(O)$ are given by

$$V_O \simeq \frac{\Delta P\ R_F}{2\left[\overline{I_F(O)} \pm \frac{\Delta I_F(O)}{2}\right] R_H}$$

$$\simeq \frac{\Delta P\ R_F}{2\overline{I_F(O)}\ R_H}\left[1 \pm \frac{\Delta I_F(O)}{2\overline{I_F(O)}}\right]$$

$$\simeq \frac{\Delta P\ R_F}{2\overline{I_F(O)}\ R_H}\left[1 \pm \frac{\Delta P_H}{4\overline{P_H(O)}}\right]$$

therefore the fractional change in V_O

$$= \pm \frac{\Delta P_H}{4\overline{P_H(O)}}$$

$$= \pm \frac{2^{\frac{1}{2}}\ \Delta T_{h.s.}}{4\,(T-T_{h.s.})}$$

where $\Delta T_{h.s.}$ represents the r.m.s. amplitude of the heat sink temperature drifts. From section (3.4.3), $\Delta T_{h.s.} \simeq .5$ m ^{o}K, therefore,

taking values for $T - T_{h.s.}$ from Table (5.1), the fractional change in V_O for detector No. 2 is $\pm$ 1% and for detector No. 3, $\pm$ 1.5%.

The S_n sensor bias current i_B is given by

$$i_B = \frac{\text{r.m.s. bias oscillator output}}{R_B}$$

i_B was set well below the critical current i_c (= $G/R_{Sn}\ \beta$) to ensure stable operation. The servo p.s.d. gain and time constant settings were then adjusted to give the best compromise between long term stability of the servo-system and good frequency response. The parameters of the No. 2 and No. 3 detectors are summarised in Table (5.1).

5.3.2 Calculation of K and G(s) parameters

K is the d.c. open loop gain of the servo-system and is given by Equation (2.3), i.e.

$$K = \frac{2\ A_1\ A_2\ i_B\ i_F\ \beta\ R_{Sn}\ R_H}{G_e\ R_F}$$

where A_1 = bridge gain x transformer effective turns ratio x pre-amp gain,

A_2 = p.s.d. conversion gain,

G_e = dynamic conductance of the bolometer element = $(G - i_B^2\ S)$,

G(s) is the frequency dependent closed loop gain and is given by equation (2.2), i.e.

$$G(s) = -\frac{K}{K+1} \cdot \frac{1}{1 + 2\ \xi\ \frac{s}{\omega_o} + \frac{s^2}{\omega_o^2}}$$

where $$\omega_o = \left[\frac{K + 1}{\tau_A\ \tau_B}\right]^{\frac{1}{2}}$$

TABLE 5.1

Parameter	Detector No. 2	Detector No. 3	Units
R_B - bridge bias resistor	10		kΩ
R_D - dummy load	5		Ω
R_{dc} - d.c. offset bias resistor	1		MΩ
R_F - p.s:d. feedback resistor	1		MΩ
R_S - signal osc. bias resistor	10		MΩ
n_d - transformer eff. turns ratio	37		
pre-amp gain	180		
p.s.d. conversion gain	300	10	
τ_A - p.s.d. time constant	4.0	.3	msec.
R_H - heater resistance	1.6	2.2	kΩ
τ_B - bolometer time constant	1.4	1.5	secs.
i_B - Sn sensor a.c. bias current	43	18	μA
i_c - critical current	228	43	μA
$I_F(O)$ - steady state heater bias current	4.0	3.0	μA
T - bolometer operating temperature	3.459	3.621	^oK
$T-T_{h.s.}$ - element - heat sink temperature difference	18	13	m ^oK
β - $1/R_{Sn}.dR_{Sn}/dT$ at op. pt.	27	210	$^oK^{-1}$
G - thermal conductance	1.4	1.6	$\mu W.^oK^{-1}$
P_B - quiescent bias power	2.6×10^{-8}	2.0×10^{-8}	W

and $$\xi = \frac{1}{2}\left[\frac{\tau_A + \tau_B}{(K+1)\ \tau_A\ \tau_B}\right]^{\frac{1}{2}}$$

Table (5.2) gives the calculated K and G(s) parameters with errors for the No. 2 and No. 3 detectors. The rather large errors are due to the combined effects of the errors in the measurement of G ($\pm$ 20%), β ($\pm$ 25%) and τ_B ($\pm$ 5%).

5.3.3 Frequency response

Frequency response measurements were made using the set-up shown in Figure (5.4). The signal oscillator was used to simulate an absorbed power input to the bolometer element as described in section (5.3.1). Care was taken to ensure that I_S was much smaller than $I_F(0)$ to preserve the linearity of the servo output. I_S was kept constant as the signal oscillator frequency was altered enabling a plot of relative servo response versus frequency to be obtained. For measurements ahove 10 Hz the signal p.s.d. could be used to measure the servo output and phase (relative to I_S). For measurements below 10 Hz, the servo output and phase response were determined using an oscilloscope.

Figures (5.6) and (5.7) show the measured servo output and phase response of the two detectors versus ω/ω_o (measured), where ω_o (measured) is taken to be the angular frequency at which the servo output is 90^o out of phase with I_S. Also shown are the best fitted calculated phase and amplitude response curves, where the amplitude response is represented by the magnitude of G(s) and the phase response by its argument. For the calculated frequency response, the experimentally measured value of ω_o is used, hence for $K \gg 1$, G(s) is a function of ω/ω_o and ξ only. Table (5.3) gives ω_o (measured) and the best fitted ξ for the two detectors. These values come within the error limits of the calculated values given in Table (5.2).

TABLE 5.2

Measured Parameters

Parameter	Detector	
	No. 2	No. 3
K	215 ± 50%	26 ± 50%
ω_o	196 Hz ± 30%	245 Hz ± 30%
ξ	.64 ± 30%	6.8 ± 30%

TABLE 5.3

Calculated Parameters

Parameter	Detector	
	No. 2	No. 3
ω_o	251 Hz ± 5	245 Hz ± 5
ξ (best fitted)	.5	6.8

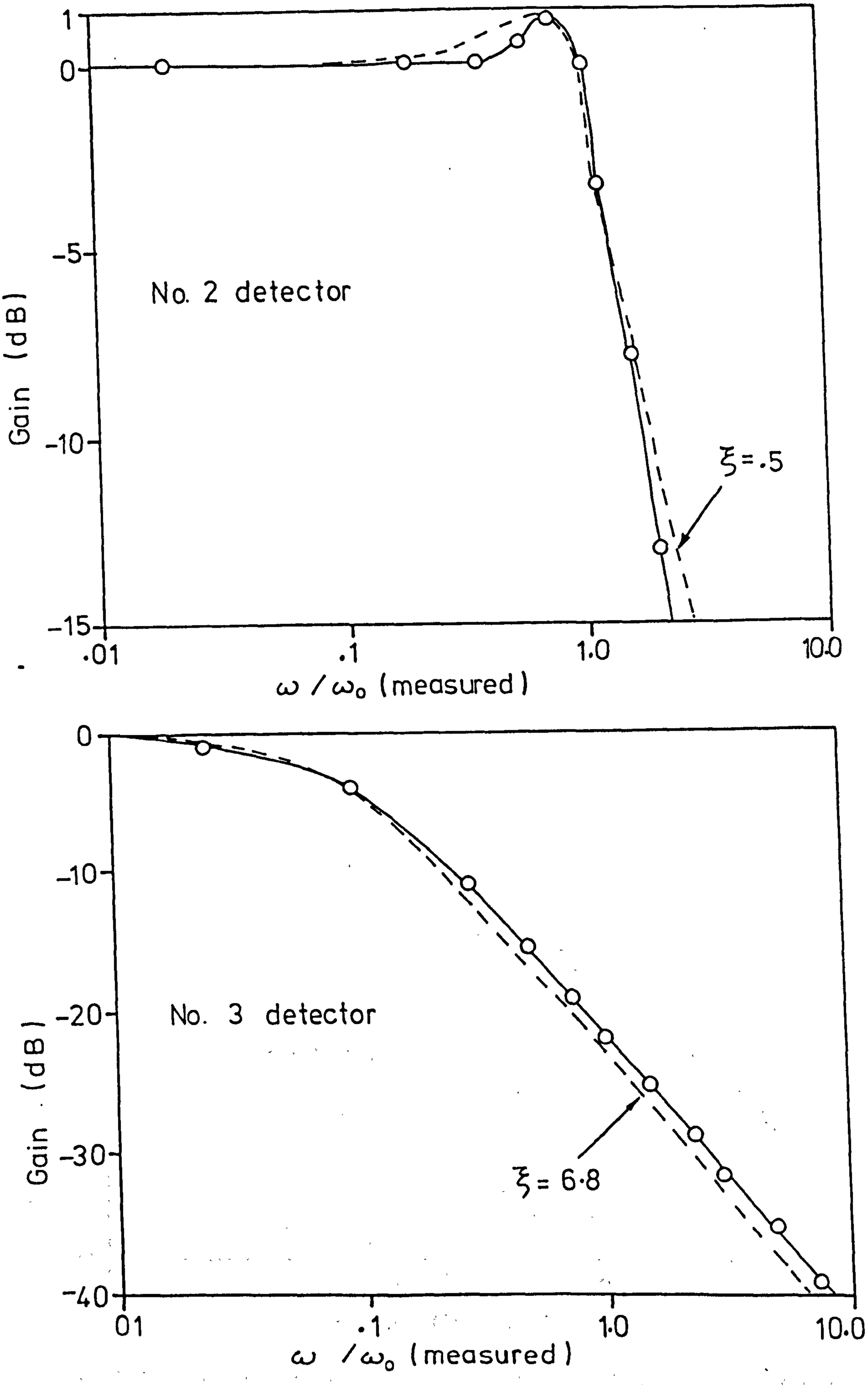

Figure 5.6. Frequency response of the No. 2 and No. 3 detectors showing measured (solid curves) and best fitted (dashed curves) response.

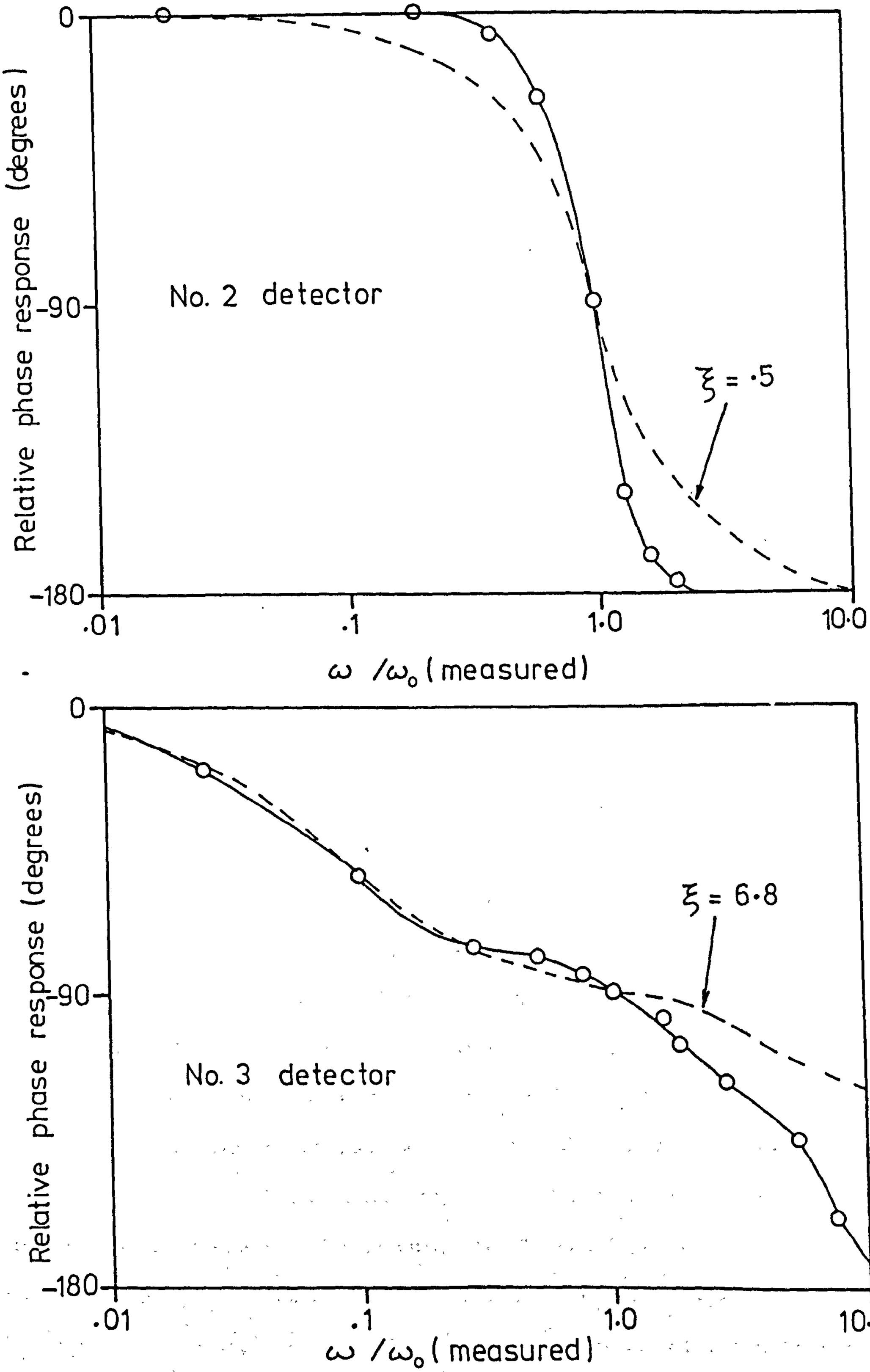

Figure 5.7. Measured (solid curves) and best-fitted (dashed curves) relative phase response for the No. 2 and No. 3 detectors.

5.3.4 Transient response

The transient response of the detectors was investigated by again using the set-up shown in Figure (5.4) with the signal oscillator set to give a low frequency square wave output large enough to give a clearly visible signal on the oscilloscope. Figure (5.8) shows the No. 2 detector servo output for a 1 Hz square wave input from the signal oscillator representing an input power to the bolometer of 2×10^{-9} W.

The step (transient) response of a second order unity gain feedback system is given by Equations (2.4), (2.5) and (2.6). The computed transient response of systems with $\xi = .5$ and 6.8 (i.e. calculated transient response of the No. 2 and No. 3 detectors) is shown in Figure (5.9).

5.3.5 Electrical noise tests

To measure electrical noise, the radiation filters mounted at the front of the radiation cone were replaced by a copper blank. The noise tests were performed using the experimental set-up shown in Figure (5.4). The method employed was as follows:

The servo output was calibrated using the method described in section (5.3.1). The servo output was detected by the signal p.s.d. (an Ithaco 391A lock-in amplifier operating in its normal mode setting). The signal oscillator was then set to zero output and the signal p.s.d. set to the noise measurement mode. The signal-to-noise ratio of the system could then be calculated. As the input power to the bolometer and bandwidth of the signal p.s.d. were known, it was then possible to compute the equivalent input noise power of the detector in a 1 Hz bandwidth, i.e. the electrical NEP. Figure (5.10) shows a plot of electrical NEP versus frequency for the No. 3 detector.

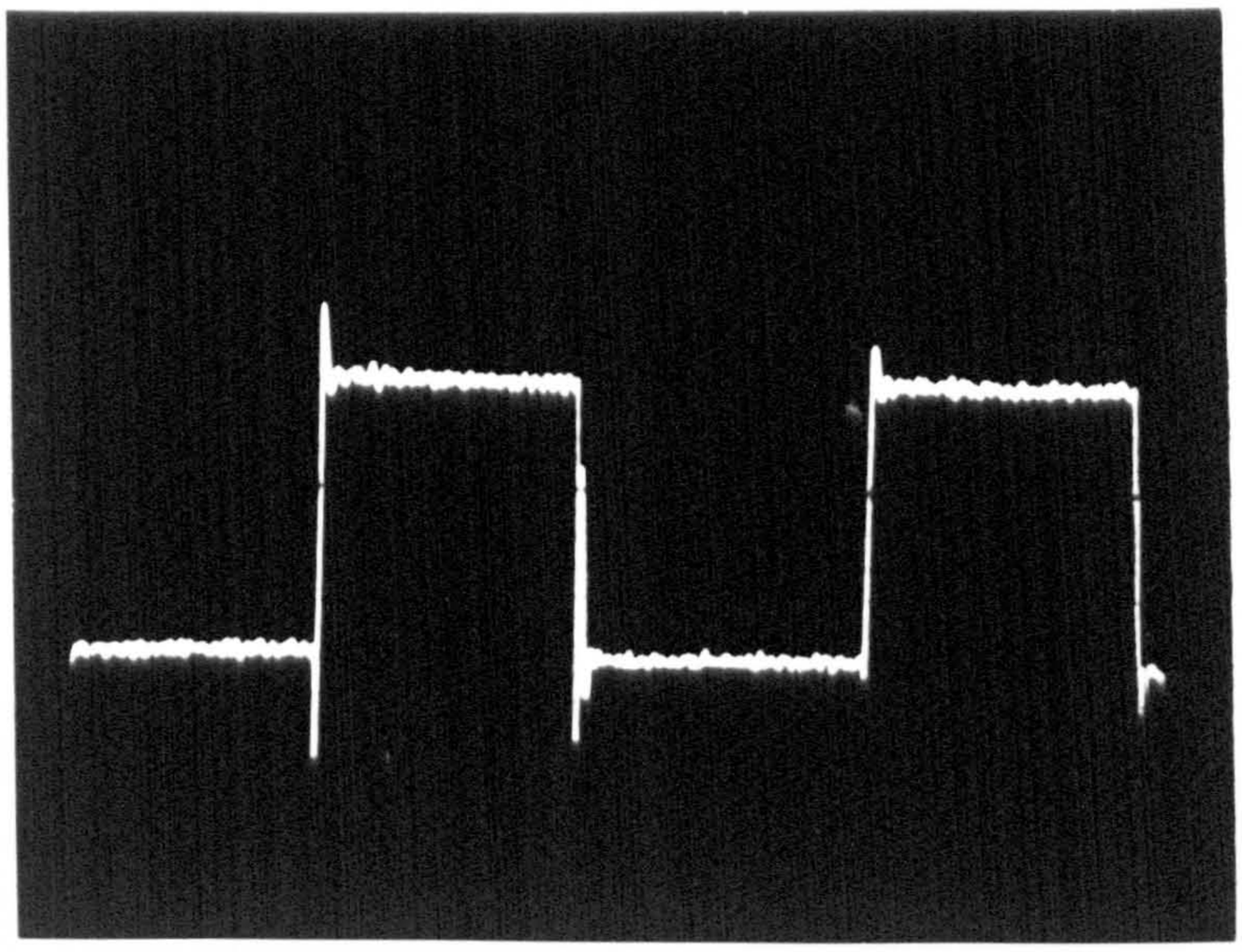

Figure 5.8. No. 2 detector servo output for a 1 Hz square wave input signal representing an input power to the detector element of 2×10^{-9} W.

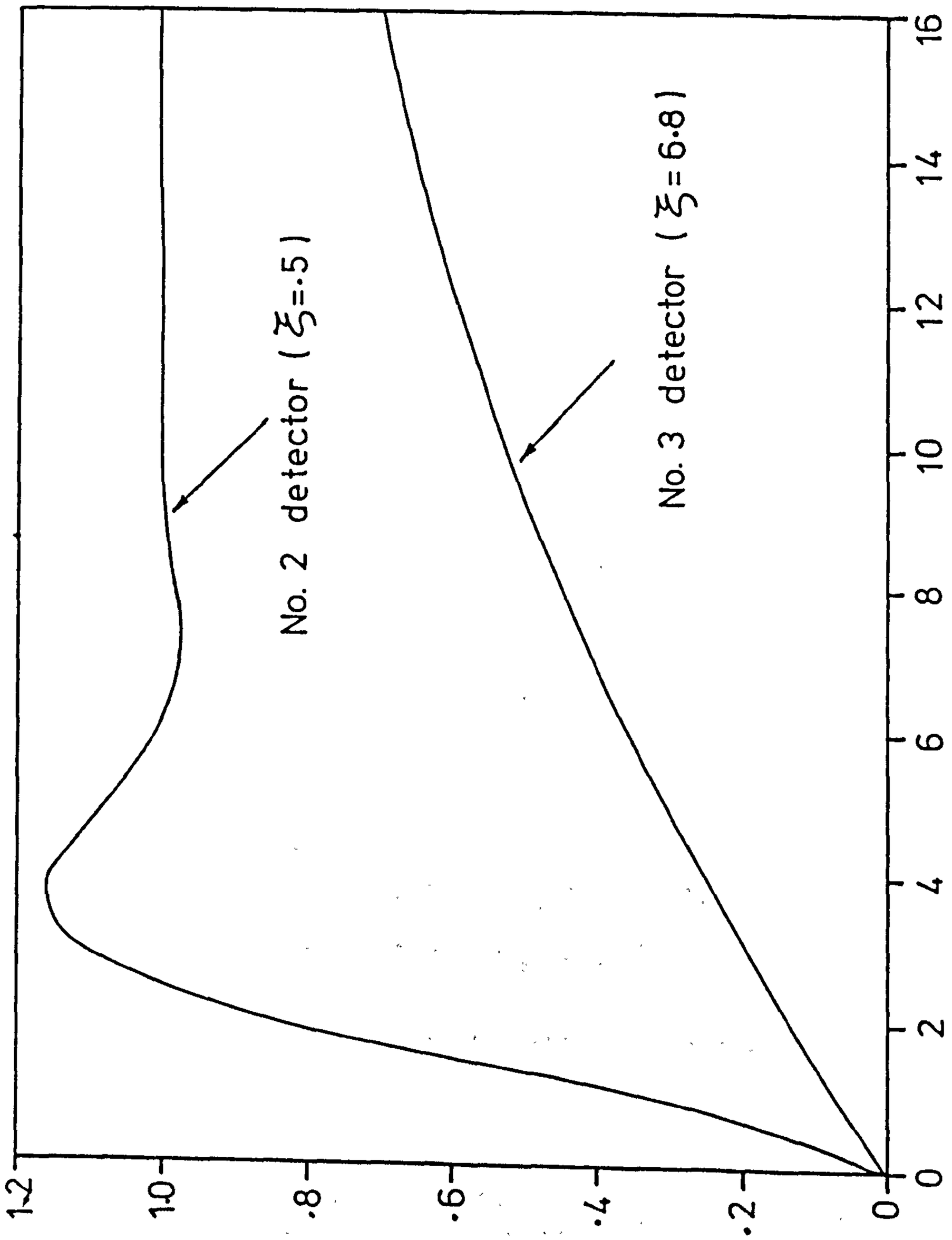

Figure 5.9. Calculated transient response of the No. 2 and No. 3 detectors.

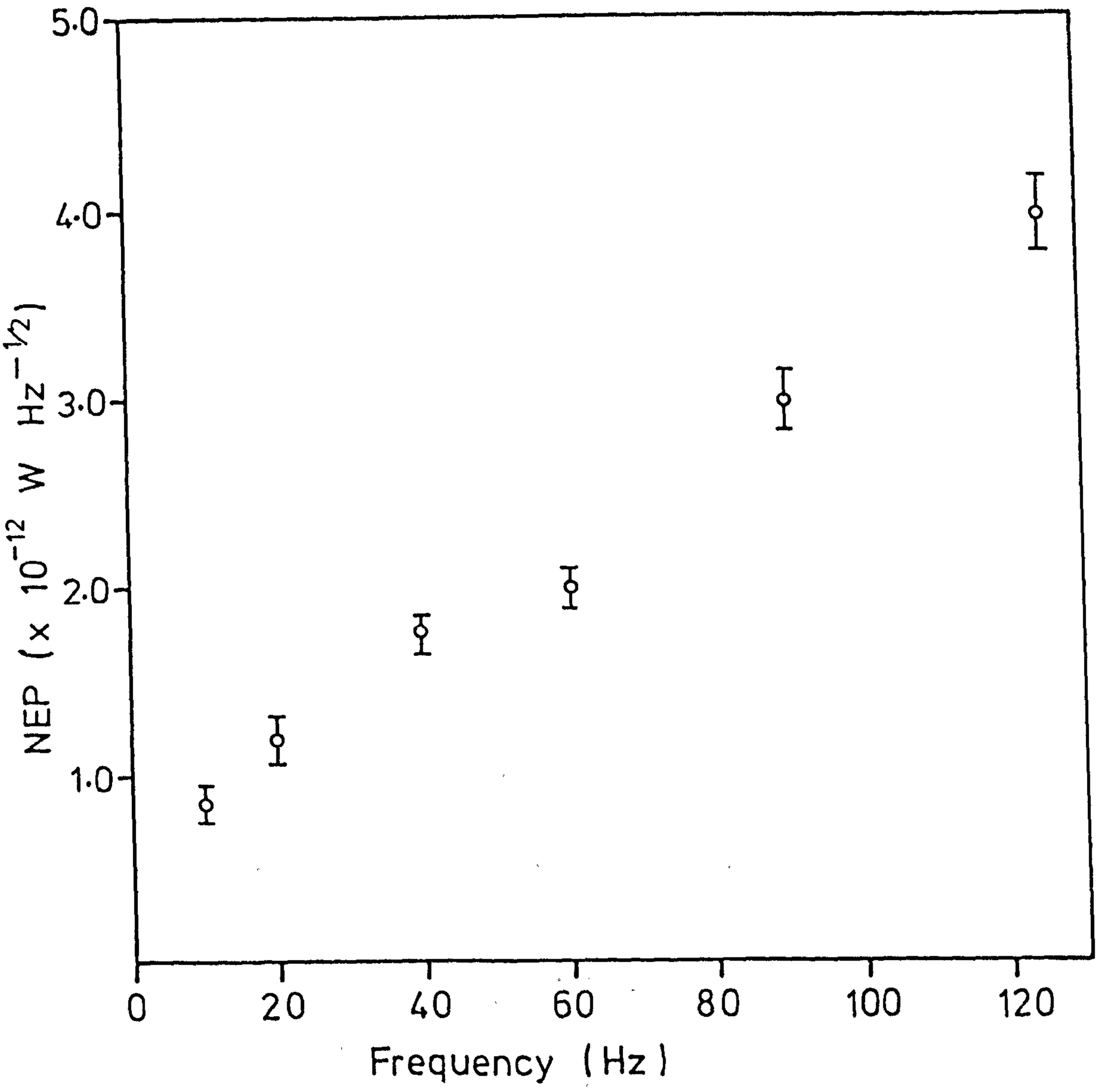

Figure 5.10. NEP versus frequency for the No. 3 detector.

5.3.6 Calculated noise spectral densities

In this section the experimentally measured equivalent input noise spectral density of the No. 3 detector will be compared with the components of the total calculated input noise spectral density, $S_i(f)$.

From Equation (2.17), the total input noise spectral density from the detector is

$$S_i'(f) = \sum_{n=1}^{3} S_n'(f)$$

$S_1'(f)$

$S_1'(f)$ is the equivalent input noise of the servo-system produced by the phonon noise, absorbed radiation noise power and heat sink temperature fluctuations, i.e.

$$S_1'(f) = S_{ph} + S_B + S_{h.s.}(f)$$

where S_{ph} and S_B are independent of f, the modulation frequency of the radiation signal.

From Equation (2.7), the phonon noise contribution S_{ph} is given by

$$S_{ph} = 2 \pi k T^2 G_e$$

For the No. 3 detector, $G_e = 1.3 \times 10^{-6}$ $\mu W.^oK^{-1}$ and $T = 3.62^oK$, therefore

$$S_{ph} = 1.6 \times 10^{-27} \quad W^2.Hz^{-1}$$

The photon noise contribution is given by

$$S_B = \frac{\alpha^2 \overline{P_B^2}}{2}$$

where, by Equation (2.13),

$$\overline{P_B^2} = \frac{4\,A(kT_B)^5}{c^2\,h^3}\,\Delta f\,\sin^2\frac{\theta}{2}\int_{x_1(T)}^{x_2(T)}\frac{x^4\,e^x}{(e^x-1)^2}\,f(x,T)\,dx \qquad \ldots\ (5.4)$$

A being the area of the radiation cone aperture,

T_B the background temperature,

Δf the post-detection system (i.e. signal p.s.d.) bandwidth,

θ the conical viewing angle of the detector optics

and $$x_i = \frac{h\,\nu_i(T)}{k\,T}$$

where $\nu_1(T)$ is the lower and $\nu_2(T)$ the upper temperature dependent cut-off frequency of the detector optics. T is the temperature of the detector optics (i.e. filters). If $x_i \ll 1$ and $f(x,T) \simeq 1$, from Equation (5.4)

$$\overline{\Delta P_B^2} = \int_{\nu_1(T)}^{\nu_2(T)}\left[\frac{4\,A(k\,T_B)^2}{c^2}\,\sin^2\frac{\theta}{2}\cdot\frac{\nu^3}{3}\,\Delta f\right] \qquad \ldots\ (5.5)$$

The upper frequency cut-off of the detector optics is approximately 15 cm^{-1} (from section (3.2.1)). The lower frequency cut-off corresponds to a wavelength of several millimetres and, because of the ν^3 dependence of Equation (5.5), the limits can be taken as $\nu_1(T) = 0$ and $\nu_2(T) = c \times 15\ cm^{-1}$. If $T_B \simeq 290^oK$, $\theta = 37^o$ and $A = 7.1 \times 10^{-6}\ m^2$ (see section (3.2)),

$$\overline{\Delta P_B^2} \simeq 1.6 \times 10^{-29}\ W^2.Hz^{-1}$$

Taking a value for α of $\simeq .5$ (from section (4.2.2)) gives

$$S_B = 2.0 \times 10^{-30}\ W^2.Hz^{-1}$$

The detector input noise due to heat sink temperature fluctuations is (by Equation (2.12))

$$S_{h.s.}(f) = \frac{\left(\Delta T_{h.s.}(f)\right)^2}{2\left|B(2\pi jf)\right|^2}$$

where $T_{h.s.}(f)$ is the heat sink temperature fluctuation spectrum.

Therefore

$$S_{h.s.}(f) = \frac{\left(\Delta T_{h.s.}(f)\right)^2 \cdot G_e^{\,2}}{2\left[1 + (2\pi f \tau_B)^2\right]} \qquad \ldots (5.6)$$

For $G_e = 1.3\ \mu W.^{o}K^{-1}$ and $\tau_B = 1.5$ secs, Equation (5.6) can be written as

$$S_{h.s.}(f) = \frac{\left(\Delta T_{h.s.}(f)\right)^2 \times 8.5 \times 10^{-13}}{\left[1 + 88.8\ f^2\right]}\ W^2.Hz^{-1}$$

The spectrum of $\Delta T_{h.s.}(f)$ is given in section (3.4.3).

$\underline{S_2'(f)}$

$S_2'(f)$ is the noise spectrum representing low frequency current noise in the Sn sensor. By Equation (2.16)

$$S_2'(f) = \frac{\overline{R_{Sn}^{\,2}}\ \beta^2\ k\ T^2}{2\left[3 + \ell n(f_2/f_1)\right] C_V\ f\ S^2\left|B(2\pi jf)\right|^2}$$

where C_V is the thermal capacity of the Sn sensor, i.e.

$$C_V = c_V \cdot \ell_1 \cdot \ell_2 \cdot \ell_3$$

where c_V is the specific heat of Sn at the bolometer operating temperature and ℓ_1, ℓ_2 and ℓ_3 are the dimensions of the Sn sensor such that $\ell_1 >> \ell_2 >> \ell_3$. Also

$$f_i = \frac{D_e}{\pi\ \ell_i^2}$$

where D_e is the effective thermal diffusivity of the Sn sensor. From

(1), D_e for Sn films at the superconducting transition evaporated onto glass is equal to 6 $cm^2.sec^{-1}$. The assumption will be made that D_e is the same for Sn films evaporated onto sapphire substrates.

Taking $\bar{V}$ as being equal to $i_B.\overline{R_{Sn}}$, and c_V as 1.5 x 10^{-3} $J.^oK^{-1}.cm^{-3}$, ℓ_1 as the total length of the zig-zag-shaped Sn film equal to 12.5 mm, ℓ_2 as the Sn track width, i.e. 150 μm, and ℓ_3 as the Sn thickness, i.e. 500 Å, gives

$$S_2'(f) = \frac{1.8 \times 10^{-25}}{f} (1 + 88.8\ f^2) \quad W^2.Hz^{-1}$$

$\underline{S_3'(f)}$

From Equation (2.14)

$$S_3'(f) = \frac{(2\ k\ T\ R_D + e_T^{\ 2})}{i_B^{\ 2}\ S^2\ |B(2\pi jf)|^2}$$

where $R_D = R_{Sn} + R_d = 10\ \Omega$. Therefore the Johnson noise produced by R_D is $2\ k\ T\ R_D = 1.0 \times 10^{-21}\ V^2.Hz^{-1}$. $e_T^{\ 2}$ is the voltage noise of the transformer/pre-amp combination referred to the transformer primary winding terminals. From section (3.3), in double-sided frequency space at the Sn sensor bias frequency (i.e. 1 K Hz)

$$e_T^{\ 2} = 9.9 \times 10^{-22}\ V^2.Hz^{-1}$$

showing that the Johnson noise and transformer/pre-amp noise are very nearly equal.

Therefore

$$S_3'(f) = 4.9 \times 10^{-30} (1 + 88.8\ f^2) \quad W^2.Hz^{-1}$$

Figure (5.11) shows the variation of S_{ph}, S_B, $S_2'(f)$ and $S_3'(f)$ together with the experimentally measured values (derived from the electrical NEP measurements) of the electrical equivalent input noise spectral density of the detector system. $S_{h.s.}(f)$ is not shown as measurements were only made at frequencies above 10 Hz where $S_{h.s.}(f)$ is negligibly small in comparison with the other noise spectra shown. However it seems likely that $S_{h.s.}(f)$ could become a significant source of noise at frequencies much less than 10 Hz.

Generally, the calculated noise spectrum is dominated by $S_2'(f)$, i.e. the low frequency noise in the Sn sensor. However it is seen that the measured values of the equivalent input noise spectral density for the detector system are considerably below the calculated values of $S_2'(f)$ at the same frequency, although still lying on approximately the same characteristic +3 dB/octave slope in the frequency range over which the noise measurements were taken. As the semi-empirical formula for noise spectral densities of Sn films on which $S_2(f)$ is based is derived from measurements of Sn films on glass[1], a possible reason for this discrepancy is that the noise of an Sn film at the superconducting transition evaporated onto sapphire is lower than that of an otherwise identical film evaporated onto glass. This indicates that the thermal coupling between the Sn film and the substrate is better for Sn films on sapphire substrates than for Sn films on glass. It therefore seems that a weakness of the expression for low frequency noise in Sn films at the superconducting transition quoted in [1] is that it contains no substrate parameters.

Other possible reasons for the discrepancy could be that Equation (2.10) applies only to d.c. biased films or just that evaporation conditions for Sn films produced for this thesis were different to

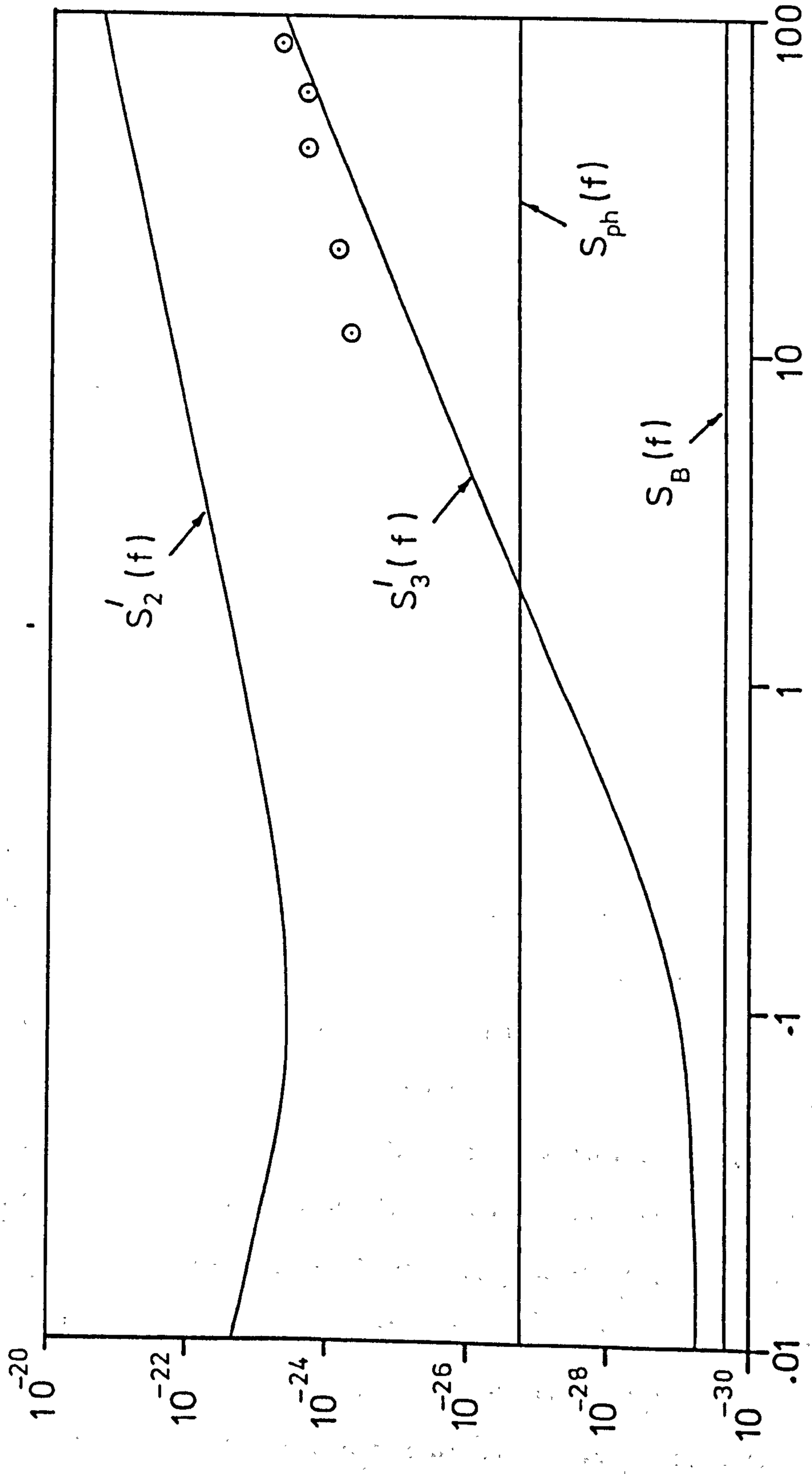

Figure 5.11. Double-sided noise spectral densities for the No. 3 detector. The curves show the calculated noise spectral densities and the circles indicate data points for the measured equivalent input noise of the detector.

those used in [1].

Figure (5.11) also indicates that the measured noise was much greater than the phonon and photon noise and that detector noise performance was dominated by $S_3'(f)$ at higher frequencies.

5.4 Radiation tests

For the radiation tests, an 11 c/s chopper, placed as close to the cryostat window as possible, was used to modulate the incoming radiation signal. The reference signal for the signal p.s.d. was provided by an optical switch consisting of an infrared source and sensor mounted opposite each other on either side of the rotating chopper blades. Figure (5.12) shows superimposed servo-system outputs for a cold source, i.e. colder than the room temperature surroundings, at approximately $77^{o}K$ (the large signal) and a warm source at approximately $310^{o}K$ (a hand). The lower trace is the modulation signal from the optical switch used to trigger the signal p.s.d.

5.4.1 Measurement of the radiation NEP

To obtain a very crude estimate of the radiation NEP of the No. 3 detector for a radiation power input, a known modulated radiation power was applied to the detector and the NEP calculated from the signal-to-noise ratio on the signal p.s.d. output. A hand placed close to the cryostat window was used as a source. Assuming that a hand has approximately black body radiation properties in the FIR, it is shown in section (3.2.2) that a modulated signal power of 4.8×10^{-11} W will fall onto the detector element.

Figure (5.13) shows the signal p.s.d. output for a hand signal using a chopping frequency of 11 c/s. The signal-to-r.m.s. noise ratio of $\simeq$ 30:1 in a 2 Hz bandwidth indicates a detector NEP of

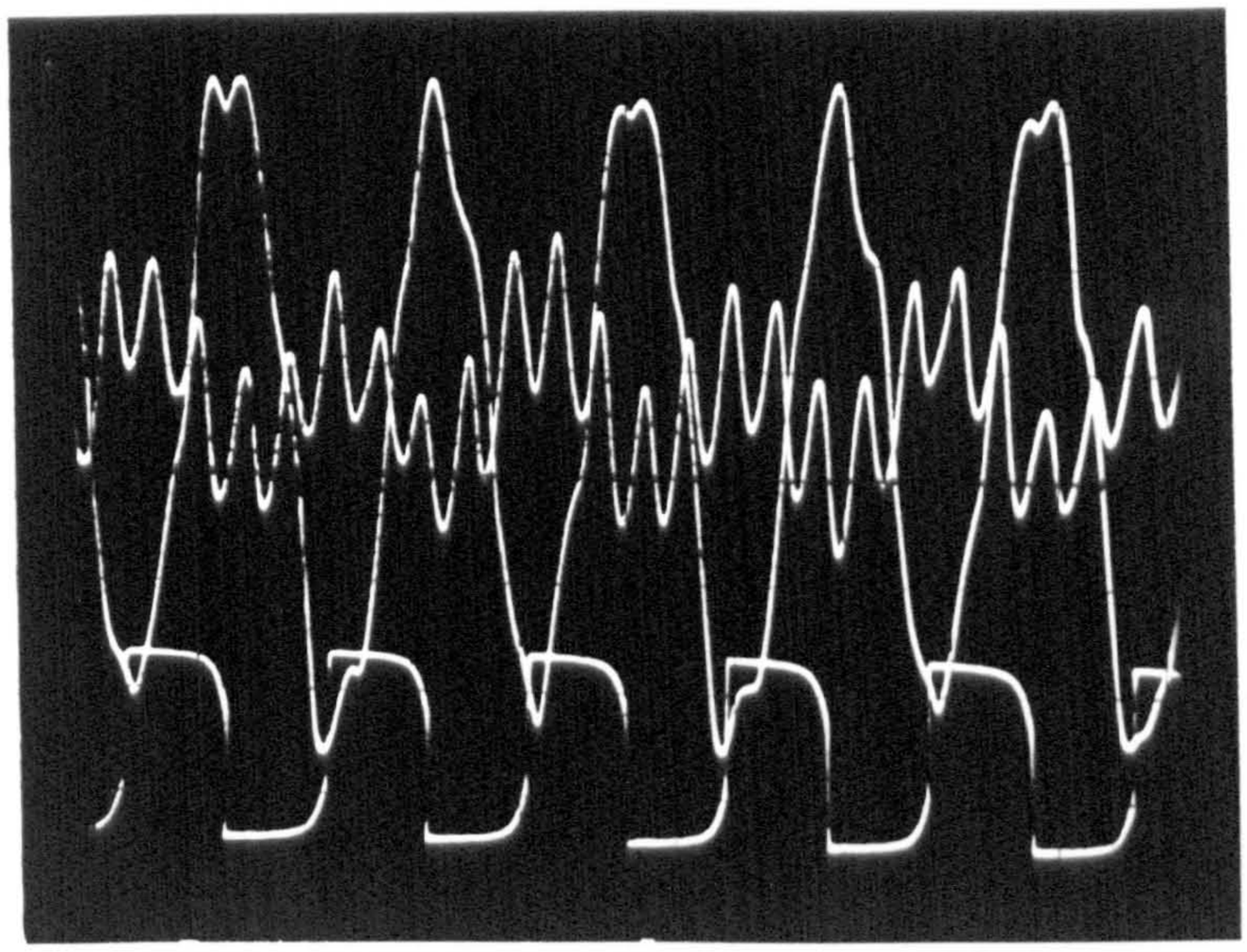

Figure 5.12. No. 3 detector servo output for a cold (77°K) source (the larger trace) and a warm source (≈310°K, the smaller trace). The lower trace represents the 11 c/s modulation of the radiation signal.

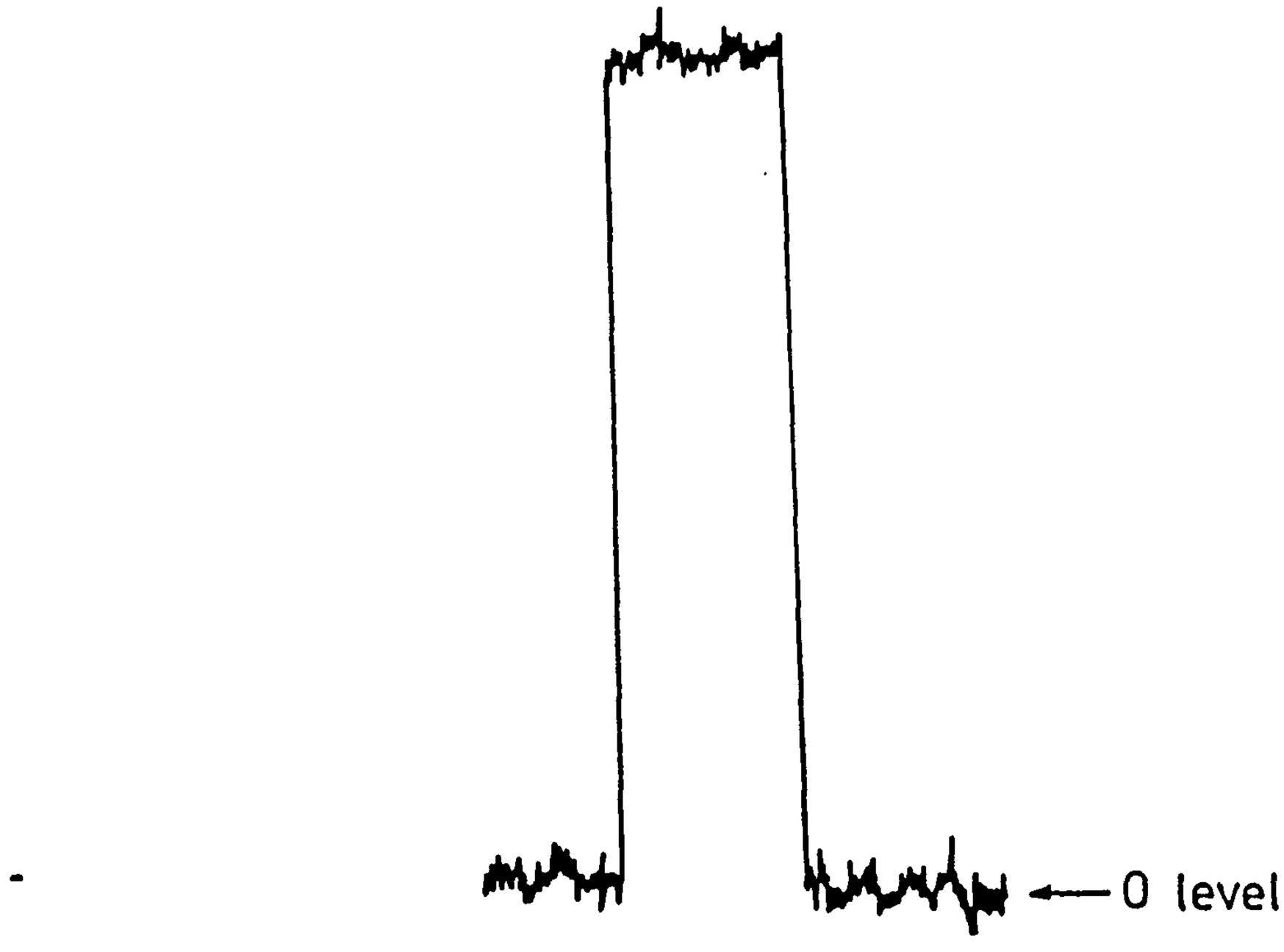

Figure 5.13. Signal p.s.d. output for a hand signal at a modulation frequency of 11 c/s. The equivalent noise bandwidth for the noise on the trace is 2 Hz.

$\simeq 1.1 \times 10^{-12}$ W.Hz$^{-\frac{1}{2}}$. From section (5.3.5), the measured <u>electrical</u> NEP for a modulated input signal at 11 Hz was 9×10^{-13} W.Hz$^{-\frac{1}{2}}$. An increased NEP for a radiation power input is expected as the detector element absorbs only a fraction of the incident radiation. As the photon noise (see section (5.3.6)) is negligible compared to the measured radiation NEP, the assumption will be made that the difference between the radiation and electrical NEP's is due entirely to the absorption coefficient of the element (i.e. α) being less than unity. In this case

$$\alpha = \frac{\text{radiation NEP}}{\text{electrical NEP}}$$

- The above values indicate that $\alpha \simeq .8$. The expected value for α is (from section (4.2.2)) about .5, giving a reasonable agreement between measured and predicted values considering the very approximate method used to calculate the radiation NEP.

CHAPTER V

REFERENCES

(1) Clarke, J. and T. Y. Hsiang, Phys. Rev. Letts. 34, No. 19, 1217 (1975).

CHAPTER VI

DISCUSSION

6.1 Summary

A STEB has been produced using a servo-controlled stabilisation of the operating temperature resulting in greater stability, better frequency response and dynamic range than would be obtained otherwise. Agreement between experimentally measured parameters (with the exception of the noise performance) and the theoretical response is close enough to fall within the experimental error limits.

The measured detector NEP was substantially below the calculated value at all measured frequencies, apparently due to the invalidity of the semi-empirical formula derived by Clarke and Voss (see section (2.3.1) used to predict low frequency noise in the Sn sensor. The character of the measured electrical noise appears to indicate that low frequency noise in the Sn sensor is still the dominant source of detector noise.

The measured electrical and radiation NEP's are reasonably consistent especially when considering the very approximate method used to measure the radiation NEP. This indicates that α is at least approximately the value predicted by the transmission line analogue model developed in Chapter IV.

The electrical and radiation NEP's were 9.0×10^{-13} $W.Hz^{-\frac{1}{2}}$ and 1.1×10^{-12} $W.Hz^{-\frac{1}{2}}$ respectively at 11 Hz. Comparison between these values and the best values achieved for Germanium (Ge) bolometers is not a straightforward matter. [1] claims measured <u>electrical</u> NEP's for Ga-doped Ge composite bolometers operating at $1.2^{o}K$ of 3.0×10^{-15} $W.Hz^{-\frac{1}{2}}$ and 6×10^{-16} $W.Hz^{-\frac{1}{2}}$ for ^{3}He-cooled In/Sb doped Ge bolometers

operating at .35°K. However, as is pointed out in [2] and [3], the electrical NEP of a composite Ge bolometer bears no fixed relationship to the true (i.e. radiation) NEP. In this respect the values quoted above can only represent an absolute lower limit for the radiation NEP's of the detectors. It can be said, however, that the optical NEP of the detector produced for this thesis is comparable with the radiation NEP's of composite Ge bolometers currently employed for FIR observations[2].

[4] gives an electrical NEP of 1.7×10^{-15} $W.Hz^{-\frac{1}{2}}$ for a STEB operating at 1.2°K using an Al film as the temperature sensor. The three orders of magnitude improvement in noise performance in comparison with the STEB produced for this thesis is accounted for by the strong dependence of the noise performance of a STEB on operating temperature and the fact that low frequency current noise for the Al-based STEB was greatly reduced due to the better thermal coupling to the substrate[5].

6.2 Future developments

Reduction of low frequency noise in the Sn sensor

As mentioned in Chapter V, it appears that, at least at low frequencies, the noise performance of the detector is limited by the low frequency current noise in the Sn sensor. A logical first step towards improving the bolometer performance would therefore be to reduce this noise if possible.

[5] claims that if a 50 Å thick Al film is used as an underlay between the Sn film and the substrate, the noise spectrum of the film flattens off below a frequency $f_1 = D_e/\pi \ell_1^2$ where ℓ_1 is the longest dimension of the film. For the STEB's produced for this thesis, ℓ_1 (the length of the Sn sensor track) was 12.5 mm. With a 50 Å thick

Al underlay, the low frequency noise spectrum would, by [5], be expected to flatten off below .6 Hz, giving no reduction in detector noise at the lowest usable modulation frequency of 11 c/s. Reduction of the track length to, say, 1 mm would give a value for f_1 of 173 Hz, i.e. the current noise in the Sn sensor would flatten off at frequencies less than 173 Hz, reducing the low frequency current noise spectral density at 11 Hz by a factor of 8. This reduction in Sn sensor track length would however reduce the responsivity of the detector element and therefore noise from the transformer/pre-amp could become dominant. Use of a transformer with a higher turns ratio would probably solve the problem.

Reduction of the thermal capacity of the bolometer element

For a given bolometer time constant τ_B, the smaller the thermal capacity C and the thermal conductance G, the lower the phonon noise and low frequency current noise. Also the bolometer responsivity is increased. Section (3.1) shows the contribution to the thermal capacity of the bolometer by each of its individual components. There is some uncertainty over the exact value of the thermal capacity of the G.E. 7031 varnish used to reinforce the mechanical strength of the cold-welded contacts. However as the mechanical strength of the contacts of the bolometers used in tests was obviously much greater than was absolutely necessary, it should be possible to substantially reduce the amount of varnish deposited on the substrate by using a solution of varnish more heavily diluted with Toluene/Alcohol.

Further worthwhile reductions in the thermal capacity of the element would be gained by using diamond substrates, smaller area In contacts and 15 μm thick nylon leads.

Reduction of the thermal conductance G

The main advantages of reducing the thermal conductance G of the element are that for a given τ_B the element responsivity is increased and the phonon noise contribution is decreased. A reduction in G could be achieved by using longer, 15 μm leads or reducing the thickness of the films deposited on the leads.

Reduction of the bolometer operating temperature

It is advantageous to operate the bolometer at as low a temperature as possible for the following reasons:

As thermal capacity is approximately proportional to T^3 and thermal conductivity to T^2, a reduction in bolometer operating temperature will, for the same τ_B, result in a lower G giving higher responsivity, lower phonon noise, thermal (Johnson) noise and low frequency current noise in the Sn sensor.

The bolometer operating temperature is determined by the transition temperature T_c of the Sn sensor. Use of Rhenum ($T_{cb} = 1.70^oK$ where T_{cb} is the transition temperature of the bulk material) or possibly Aluminium ($T_{cb} = 1.19^oK$ but in the range $1.3 \rightarrow 3.7^oK$ for thin films) would result in a significantly decreased bolometer operating temperature while still being able to use ^4He cooling.

The use of ^3He cooling with heat sink temperatures of less than $.3^oK$ would enable superconductors of even lower T_c to be used, e.g. Cadmium ($T_{cb} = .55^oK$) or Titanium ($T_{cb} = .39^oK$) resulting in a potential increase in noise performance of at least an order of magnitude compared to ^4He-cooled STEB's.

CHAPTER VI

REFERENCES

(1) Nishioka, N.S., P. L. Richards, and D. P. Woody, 2nd International Conference and Winter School on Submillimetre Waves and their Applications, San Juan, Puerto Rico (New York, U.S.A.; I.E.E.E. 1976), pp. 66-7.

(2) El-Atawy, S.A. and P. A. R. Ade, Infrared Physics, 18, 683 (1978).

(3) El-Atawy, S.A., P. A. R. Ade, I. G. Nott and J. V. Radostitz, submitted for publication in Journal of Infrared and Millimetre Waves, March 7 (1980).

(4) Clarke, J., Third International Conference on Submillimetre Waves and their Applications, 29th March - 1st April (1978).

(5) Clarke, J. and T. Y. Hsiang, Phys. Rev. Letts. 34, No. 19, 1217 (1975).

(6) Martin, D.H. and D. Bloor, Cryogenics 1, 159 (1961).

APPENDIX I

A1.1 Effective product of m(t) and d(t) in the servo loop

Figure (A1.1) shows a simplified version of the functional servo circuit shown in Figure (2.2a). B'(s) represents the combined transfer function of B(s) and S in Figure (2.2a) and A(s) represents the combination of $A_1(s)$ and $A_2(s)$. f(s) represents the effect of the feedback resistors R_{F_1} and R_{F_2}. The functions m(t) and d(t) are the modulation and demodulation functions of Figure (2.2a) where

$$m(t) = 2^{\frac{1}{2}} i_B \cos 2\pi f_o t$$

$$d(t) = 2^{\frac{1}{2}} \cos 2\pi f_o t$$

giving

$$m(t).d(t) = i_B(1 + 2\cos 4\pi f_o t)$$

Therefore provided the bandwidth of the product of B'(s), A(s) and f(s) is small compared to $2f_o$, the product of m(t) and d(t) in the servo loop is effectively equal to i_B. The reason for including the factor $2^{\frac{1}{2}}$ in the expressions for m(t) and d(t) was to ensure that m(t).d(t) was just i_B so that $A_2(s)$ is just the a.c. to d.c. conversion gain of the p.s.d. The overall closed loop transfer function will be

$$Y(s) = \frac{A(s)\ B'(s)}{1 + f(s)\ A(s)\ B'(s)}$$

A1.2 Effective servo-system input noise from $S_3(f)$

Consider stoichastic process z(t) injected as indicated in Figure (A1.1) The resulting open loop spectral density at the output is

$$|A(f)|^2\ (S_d(f) * S_z)$$

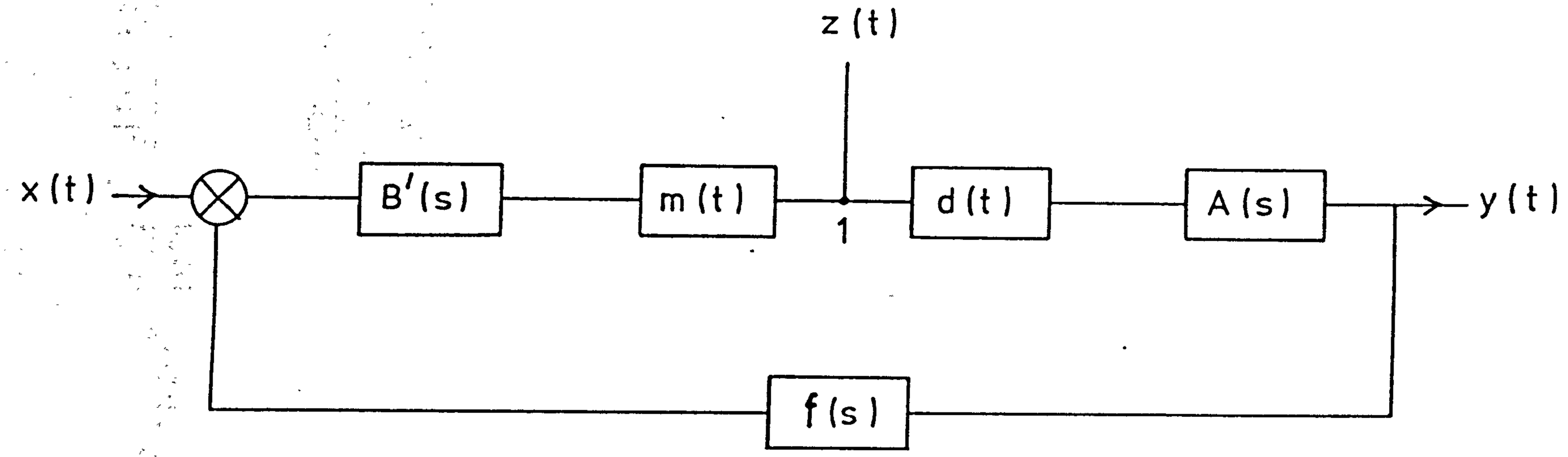

Figure A1.1. Simplified functional servo circuit.

where $S_d(f)$ is the spectral density of the demodulating function d(t) in frequency space. On open loop, however, the spectral density at point 1 produced by a spectral density $S_{in}(f)$ at the input is

$$S_m(f) * \left[\left| B'(2 \pi j f) \right|^2 S_{in}(f) \right]$$

where $S_m(f)$ is the spectral density of the modulating function. It is necessary to find that $S_{in}(f)$ which is a solution of

$$S_m(f) * \left[\left| B'(2 \pi j f) \right|^2 S_{in}(f) \right] = S_z(f) \qquad \ldots(A1.1)$$

$$\left[\text{i.e.} \quad \int_{-\infty}^{+\infty} S_m(f - f') \left| B'(2 \pi j f') \right|^2 S_{in}(f') \, df' = S_z(f) \right]$$

$$\text{let } \left| B'(2\pi j f) \right|^2 S_{in}(f) = S_{in}'(f)$$

Note that for a function g(t)

$$R_g(\tau) = \underset{T \to \infty}{Lt} \frac{1}{T} \int_{-T/2}^{+T/2} g(t) \, g(t + \tau) \, dt$$

$$S_g(f) = F.T.\left[R_g(\tau) \right]$$

Therefore

$$R_m(\tau) \, R_{in}'(\tau) = R_z(\tau)$$

$$R_{in}'(\tau) = \frac{R_z(\tau)}{R_m(\tau)}$$

and

$$S_{in}(f) = \frac{1}{\left| B'(2 \pi j f) \right|^2} \int_{-\infty}^{+\infty} \frac{R_z(\tau)}{R_m(\tau)} \, e^{-j2\pi f \tau} \, d\tau \qquad \ldots(A1.2)$$

$$R_m(\tau) = \underset{T\to\infty}{Lt} \frac{2}{T} \int_{-T/2}^{+T/2} \cos \omega_o t \cos \omega_o (t + \tau)\, dt$$

$$= \underset{T\to\infty}{Lt} \frac{1}{T} \int_{-T/2}^{+T/2} \left[\cos(2 \omega_o \overline{t + \tau}) + \cos \omega_o \tau\right] dt$$

therefore

$$R_m(\tau) = \cos 2 \pi f_o \tau \qquad \ldots(A1.3)$$

Suppose the noise is white in a bandwidth Δf corresponding to the bandwidth of $B'(s)$ around the modulating frequency, then

$$S_z(f) = S_z(\text{a constant}) \begin{cases} -f_o - \frac{\Delta f}{2} \leq f \leq -f_o + \frac{\Delta f}{2} \\ f_o - \frac{\Delta f}{2} \leq f \leq f_o + \frac{\Delta f}{2} \end{cases}$$

$$= 0 \qquad \text{otherwise}$$

then

$$\frac{R_z(\tau)}{S_z(f)} = \int_{-f_o-\frac{\Delta f}{2}}^{-f_o+\frac{\Delta f}{2}} e^{j2\pi f\tau}\, df + \int_{f_o-\frac{\Delta f}{2}}^{f_o+\frac{\Delta f}{2}} e^{j2\pi f\tau}\, df$$

$$= e^{-j2\pi f_o\tau} \cdot \frac{\sin 2\pi \frac{\Delta f}{2} \tau}{\pi \tau} + e^{j2\pi f_o\tau} \cdot \frac{\sin 2\pi \frac{\Delta f}{2} \tau}{\pi \tau}$$

$$= 2 \left[\frac{\sin \pi \Delta f \tau}{\pi \tau}\right] \cos 2 \pi f_o \tau$$

so that from Equations (A1.2) and (A1.3)

$$S_{in}(f) = \frac{S_z}{|B'(2 \pi j f)|^2} \int_{-\infty}^{+\infty} 2\left[\frac{\sin \pi \Delta f \tau}{\pi \tau}\right] e^{-j2\pi f\tau}\, d\tau$$

$$= \frac{2 S_z}{|B'(2 \pi j f)|^2} \quad -\frac{\Delta f}{2} \leq f \leq \frac{\Delta f}{2}$$

$$= 0 \qquad \text{otherwise}$$

APPENDIX II

TP-1 low noise pre-amplifier

The pre-amp used in the STEB servo-system (see Chapter III) to amplify the signal produced across the transformer secondary terminals was required to be a wideband amplifier with as low an equivalent input voltage noise as possible at 1 K Hz (the STEB bias frequency) and negligible current noise. The pre-amp selected was based on a design by T. G. Philips of Bell Labs. and is shown in Figure (A2.1).

The pre-amp input stage uses four JFET's biased in the CS configuration and connected in parallel to reduce the input noise by a factor of two compared with a single transistor stage. The JFET's used were selected 2N6453's biased at 10 mA drain current for optimum noise performance. The pre-amp was powered by two external 12 V accumulators, hence the need for the r.f. filters to reduce r.f. pick-up in the power supply leads. The relevant pre-amp specifications are listed in Table (A2.1).

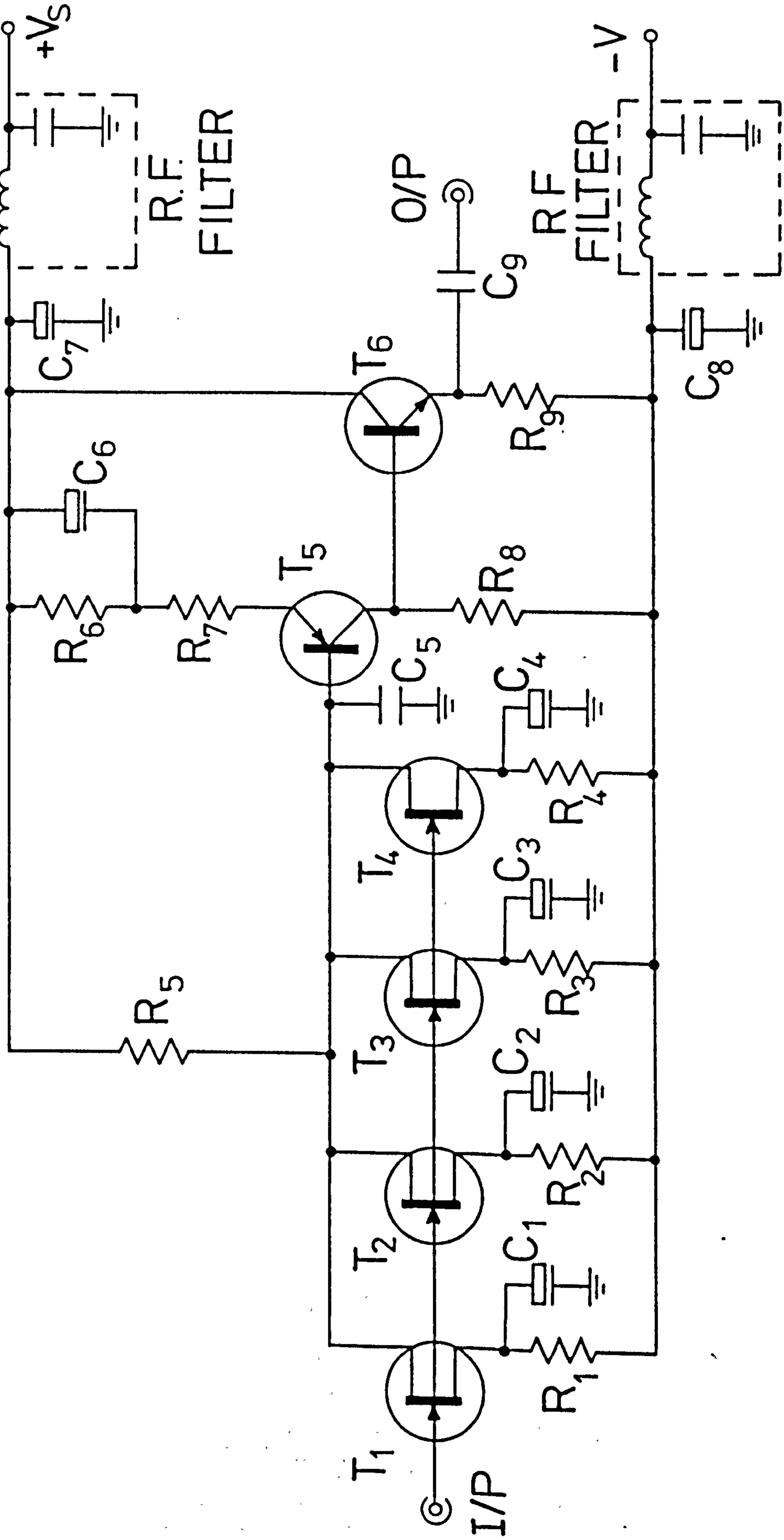

Figure A2.1. TP-1 pre-amp.

TP-1 Components

R_1	Carbon film resistor	¼ W	5%	1.5 k
R_2	"			
R_3	"			
R_4	"			
R_5	"			82 Ω
R_6	"			1 k
R_7	"			56 Ω
R_8	"			3.3 k
R_9	"			1.5 k
C_1	Tantalum electrolytic	330 µF		6.3 V
C_2	"			
C_3	"			
C_4	"			
C_5	Polystyrene	470 pF		160 V
C_6	Tantalum electrolytic	22 µF		16 V
C_7	"			
C_8	"			
T_1	2N6453	selected		
T_2	"			
T_3	"			
T_4	"			

TABLE A2.1

Voltage gain	-	180
frequency response (-3 dB)	-	40 Hz → 2 M Hz
input impedance	-	$> 10^9\ \Omega$
equivalent input noise voltage	-	.6 $nV.Hz^{-\frac{1}{2}}$ @ 1 K Hz
equivalent input noise current	-	4×10^{-15} $A.Hz^{-\frac{1}{2}}$ @ 30 Hz
quiescent current consumption	-	45 mA
power supply	-	± 12 V

APPENDIX III

Low noise pre-amplifier developed for use with QMC Instruments Ltd. In Sb detectors

As mentioned in Chapter I, the work for this thesis was financed by an SRC CASE award, with QMC Instruments Ltd. acting as the industrial co-sponsor. The following describes a low noise pre-amplifier (designated the ULN-10) developed for use with QMC Instruments Ltd. In Sb infrared detectors.

An In Sb detector consists basically of a ^{4}He-cooled In Sb crystal biased with a constant d.c. current. Radiation incident on the crystal produces a small change in crystal resistance and therefore voltage across the crystal. In the ideal case, the signal-to-noise ratio of the signal produced across the crystal is dominated by the thermal noise (e_{TX}) produced by the crystal resistance i.e.

$$e_{TX} = (4\ k\ T_X\ R_X\ \Delta f)^{\frac{1}{2}} \quad \text{Volts} \qquad \ldots(A3.1)$$

where T_X is the crystal temperature and R_X is the crystal resistance.

In Sb crystal resistances depend on the operating temperature T_X but typically range from 2 kΩ at 4.2°K to 10 kΩ at 1.5°K. By Equation (A3.1), the crystal noise will be approximately .7 nV.Hz$^{-\frac{1}{2}}$ at 4.2°K and .9 nV.Hz$^{-\frac{1}{2}}$ at 1.5°K. Ideally then, the equivalent input noise of the pre-amp used to amplify the signal produced across the crystal should be of the order of a few tenths of a nanovolt or less. The lowest noise transistors available are not capable of producing noise levels of much less than about 1 nV.Hz$^{-\frac{1}{2}}$. Hence it would not be possible to produce an In Sb pre-amp which fulfils this condition using a single transistor input stage. It would be possible to reduce

the pre-amp input noise by connecting a number of transistors in parallel. However, one of the requirements of the In Sb pre-amp was that it could be run off small re-chargeable batteries and the additional current drain when using more than one input transistor (each transistor needing approximately 10 mA drain current) was not regarded as being worthwhile compared with the resulting improvement in pre-amp input noise (note that for n transistors connected in parallel, the noise is reduced by a factor of $n^{\frac{1}{2}}$ compared with a single transistor stage).

Transformer coupling of the input was ruled out because of the wide frequency range of operation of the crystal i.e. a few hertz to approximately 500 k Hz. Hence the design aim was to limit the input noise of the pre-amp to the inherent noise of the input transistor while maintaining an adequate frequency response and low current consumption.

The resulting design is shown in Figure (A3.1). It was decided to use a JFET rather than a bipolar input transistor as with the source impedances (i.e. R_X) used, there would be insignificant low frequency current noise. The transistor selected for the input stage was the 2N6550 JFET. The input stage of the pre-amp uses this transistor (T_1) in a CS configuration with d.c. coupling to the crystal. To produce an adequate frequency response and near optimum noise levels, i_D for T_1 is set at 7 mA. The first stage is followed by a cascode stage formed by bipolar transistors T_2 and T_3, giving good frequency response and low current consumption, with noise levels the same as for a CE stage. The current noise performance of T_2 is very important as the source resistance for the cascade stage is the output impedance of the input stage. Hence the choice of the 2N4250

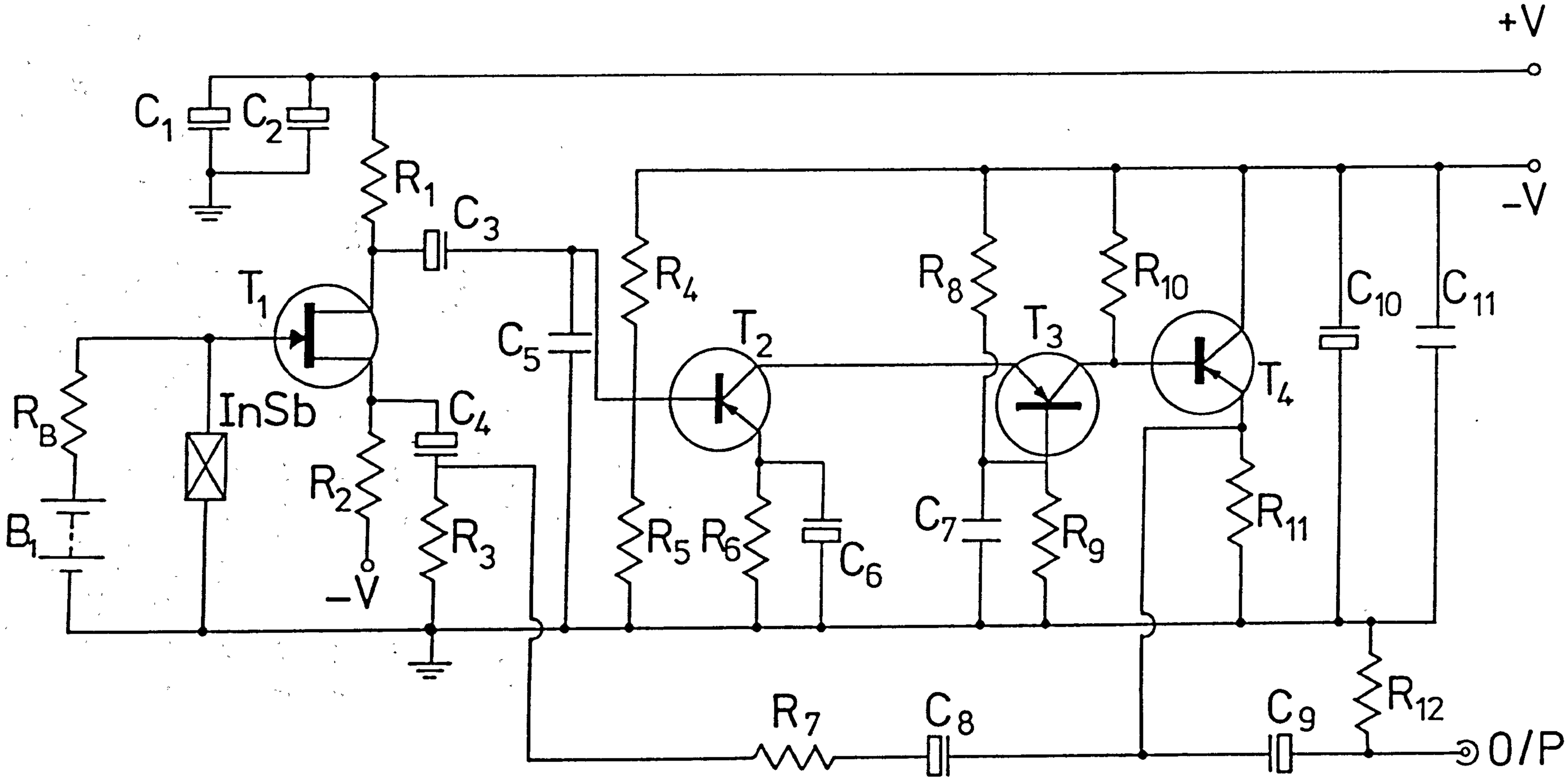

Figure A3.1. ULN-10 pre-amp.

ULN-10 components

R_1	metal oxide film resistor	½ W	2%	1 k
R_2	"			1 k 8
R_3	"			10 R
R_4	"			330 k
R_5	"			150 k
R_6	"			3 k 3
R_7	"			1 k 2
R_8	"			33 k
R_9	"			43 k
R_{10}	"			1 k 2
R_{11}	"			10 k
R_{12}	"			100 k
C_1	tantalum electrolytic	47 µF	16 V	
C_2	disc ceramic	.1 µF	100 V	
C_3	tantalum electrolytic	22 µF	16 V	
C_4	"	680 µF	6.3 V	
C_5	miniature ceramic	2 n 2	100 V	
C_6	tantalum electrolytic	100 µF	6.3 V	
C_7	polyester	2.2 µF	63 V	
C_8	tantalum electrolytic	330 µF	6.3 V	
C_9	"	22 µF	16 V	
C_{10}	"	47 µF	16 V	
C_{11}	disc ceramic	.1 µF	100 V	
T_1	2N6550			
T_2	2N4250			
T_3	"			
T_4	"			

B_1 4.1 V Duracell bias battery

R_B In Sb bias resistor

pnp transistor, as it exhibits very low current noise. T_4 is used as a buffer to drive the feedback resistor network formed by R_7 and R_3. It is important that R_3 noise is lower than the pre-amp input noise as it adds directly to the pre-amp input. Hence the value of 10 Ω chosen for R_3. C_5 gives a smooth 6 dB/octave open loop roll-off to the pre-amp to stop closed loop oscillation or high frequency instabilities. Table (A3.1) gives a summary of the ULN-10 specifications and Figure (A3.2) the phase and amplitude frequency response.

TABLE A3.1

Voltage gain	-	100
Frequency response (-3 dB)	-	5 Hz → 400 k Hz
Equivalent input noise		
Voltage (typically)	-	1.0 $nV.Hz^{-\frac{1}{2}}$ @ 1 K Hz 4.0 $nV.Hz^{-\frac{1}{2}}$ @ 10 Hz
Equivalent input noise		
Current (typically)	-	10^{-14} $A.Hz^{-\frac{1}{2}}$ @ 100 Hz
Input impedance	-	> 10^{9} Ω
Output impedance @ 1 K Hz	-	50 Ω
Output voltage swing	-	1.0 V
Power supply	-	± 10.6 V
Quiescent current consumption	-	9 mA

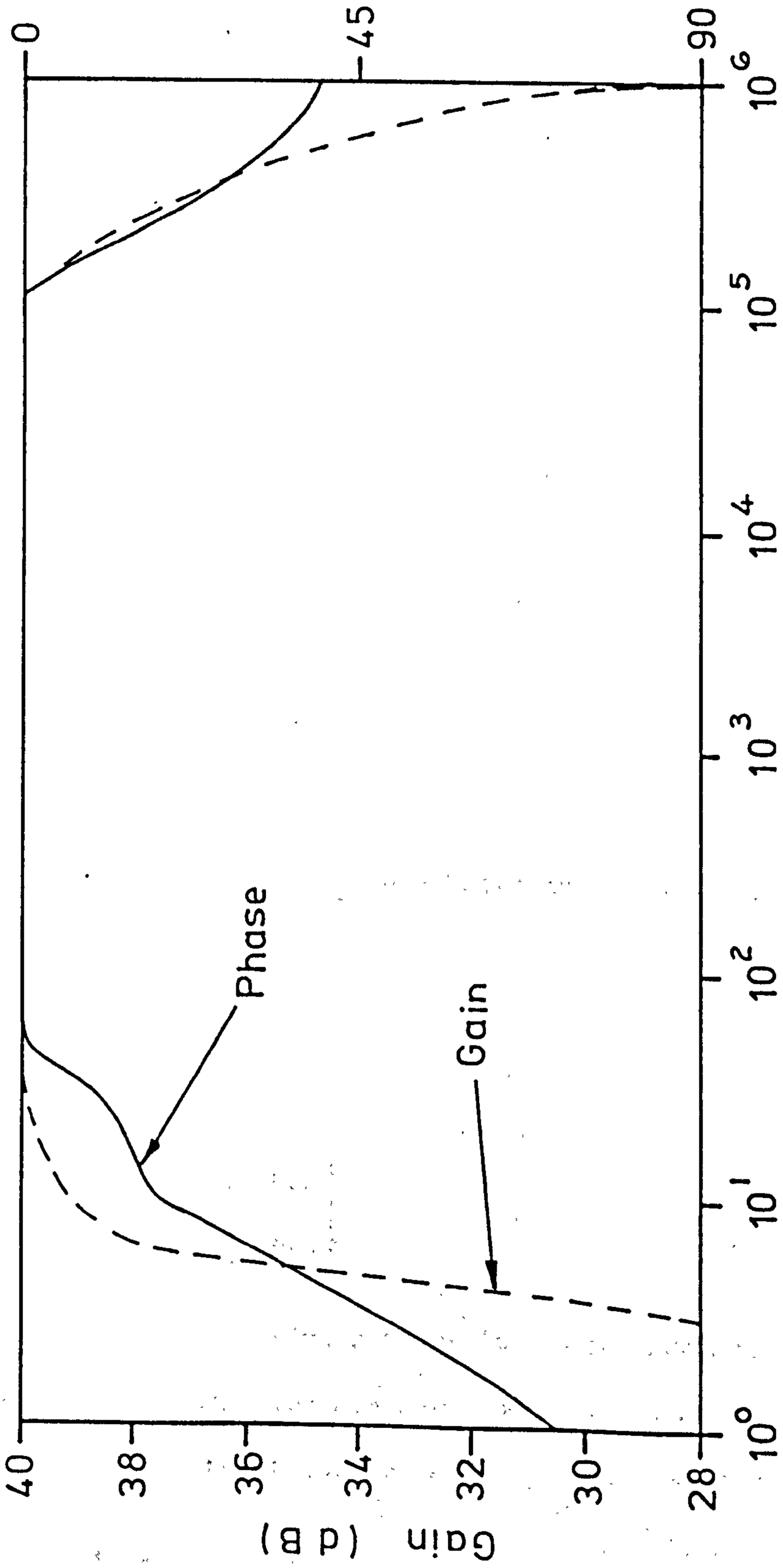

Figure A3.2. ULN-10 frequency response.

APPENDIX IV

SCATTERING COEFFICIENTS FOR TWO CASCADED TWO-PORT NETWORKS REPRESENTING AN ABSORBING BOLOMETER SUBSTRATE

A4.1 Scattering representation of a two-port network

Figure (A4.1) shows a two-port network with incident voltages V_a and V_b at the network terminals (i.e. the reference planes, which are in this case the dielectric interfaces). The characteristic impedance of the transmission line connected to port 1 is Z_1, and of the line connected to port 2, Z_2. The quantities a and b are such that a.a* is the power in the incident wave and b.b* the power in the reflected wave. Define

$$b_1 = S_{11}\, a_1 + S_{12}\, a_2 \qquad \ldots(A4.1)$$

$$b_2 = S_{21}\, a_1 + S_{22}\, a_2 \qquad \ldots(A4.2)$$

where S_{11}, S_{22}, S_{12} and S_{21} are known as the scattering coefficients. In matrix form we have:

$$\underline{b} = \underline{S}.\underline{a} \qquad \ldots(A4.3)$$

where

$$\underline{S} = \begin{bmatrix} S_{11} & S_{12} \\ S_{21} & S_{22} \end{bmatrix}$$

For a linear passive network it may be shown that, by reciprocity, $S_{12} = S_{21}$. If the interface between port 1 and port 2 is taken as the reference plane, the total normalised voltage at port 1 is

$$v_1 = a_1 + b_1 \qquad \ldots(A4.4)$$

By definition, the power in the incident wave is $a_1\, a_1^* = |a_1|^2$, and

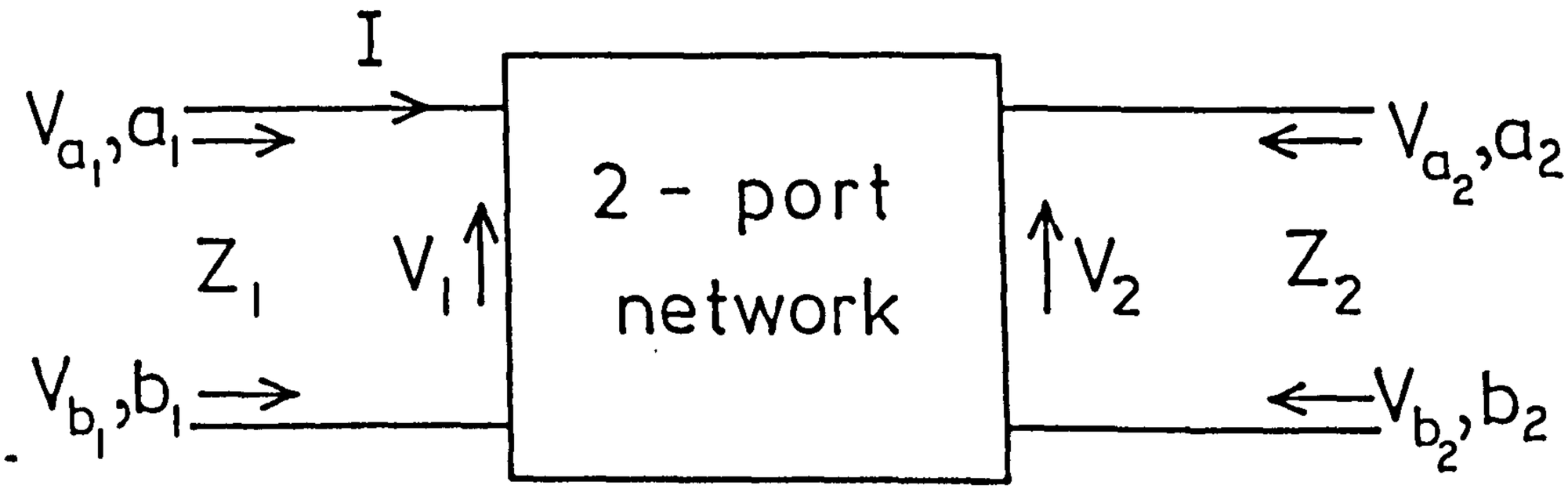

Figure A4.1. Scattering representation of a two-port network.

similarly the power in the reflected wave = $|b_1|^2$. In terms of the actual voltages, the power is $V_a \; V_a^*/Re(Z_1)$, where the voltages are r.m.s. values. Equating the two powers gives

$$a_1 \; a_1^* = \frac{V_{a_1}}{[Re(Z_1)]^{\frac{1}{2}}} \cdot \frac{V_{a_1}}{[Re(Z_1)]^{\frac{1}{2}}}$$

$$\text{or} \qquad a_1 = a_1^* = \frac{V_{a_1}}{[Re(Z_1)]^{\frac{1}{2}}} \qquad \ldots(A4.5)$$

Similarly

$$b_1 = b_1^* = \frac{V_{b_1}}{[Re(Z_1)]^{\frac{1}{2}}} \qquad \ldots(A4.6)$$

From Equation (A4.4)

$$v_1 = \frac{V_1}{[Re(Z_1)]^{\frac{1}{2}}}$$

$$= a_1 + b_1 \qquad \ldots(A4.7)$$

From standard transmission line theory it can be shown that

$$I = Y_o(V_a \; e^{-j\beta z} - V_b \; e^{j\beta z})$$

where Y_o is the transmission line admittance = $1/Z_o$, I is the current and β is the phase change coefficient. Substituting for V_a and V_b and using Equations (A4.5), (A4.6) and (A4.7) gives

$$\frac{I_1 \; Z_1}{[Re(Z_1)]^{\frac{1}{2}}} = a_1 - b_1 \qquad \ldots(A4.8)$$

where I_1 is an r.m.s. value. Eliminating b_1 between Equations (A4.7) and (A4.8) gives

$$a_1 = \frac{V_1 + I_1 Z_1}{2[\mathrm{Re}(Z_1)]^{\frac{1}{2}}}$$

Similarly eliminating a_1 gives

$$b_1 = \frac{V_1 - I_1 Z_1}{2[\mathrm{Re}(Z_1)]^{\frac{1}{2}}}$$

Using similar arguments at port 2 we have:

$$a_2 = \frac{V_2 + I_2 Z_2}{2[\mathrm{Re}(Z_1)]^{\frac{1}{2}}}$$

and $$b_2 = \frac{V_2 - I_2 Z_2}{2[\mathrm{Re}(Z_2)]^{\frac{1}{2}}}$$

at the reference plane.

It is now necessary to relate the a and b terms in Equations (A4.1) and (A4.2) to the actual voltages and currents at the network ports.

If port 2 is terminated by a matched load (i.e. an impedance Z_2) b_2 will not be reflected. Also $a_2 = 0$. Then Equations (A4.1) and (A4.2) give

$$b_1 = S_{11} a_1 \quad \text{or} \quad \frac{b_1}{a_1} = S_{11}$$

From Equations (A4.5) and (A4.6) we have:

$$\frac{b_1}{a_1} = \frac{V_b}{V_a} = S_{11} = R_{12} \qquad \ldots(A4.9)$$

i.e. S_{11} = reflection coefficient at port 1 when port 2 is terminated by its characteristic impedance. From Equations (A4.1) and (A4.2) also

$$\frac{b_2}{a_1} = S_{12} \qquad ..(A4.10)$$

For waves travelling in the positive z direction, τ_{12}, the voltage transmission coefficient, can be expressed as

$$\tau_{12} = \frac{V_{b_2}}{V_{a_1}}$$

$$= \frac{b_2}{a_1} \cdot \frac{\left[\mathrm{Re}(Z_2)\right]^{\frac{1}{2}}}{\left[\mathrm{Re}(Z_1)\right]^{\frac{1}{2}}}$$

$$= S_{12} \left[\frac{Z_2}{Z_1}\right]^{\frac{1}{2}}$$

if the impedances are real. Similarly

$$S_{22} = \frac{b_2}{a_2} = R_{21} \qquad \text{..(A4.11)}$$

and

$$S_{21} = \tau_{21} \left[\frac{Z_1}{Z_2}\right]^{\frac{1}{2}} \qquad \text{..(A4.12)}$$

for real impedances.

A4.2 Calculation of overall parameters of two two-port networks connected by a length of transmission line

Figure (A4.2a) shows two two-port networks connected together by a length of transmission line ℓ. The overall scattering coefficients S_{11}', $S_{12}' = S_{21}'$ and S_{22}' are to be found.

The equations for each two-port are

$$b_1 = S_{11}\, a_1 + S_{12}\, a_2 \qquad \text{..(A4.13a)}$$

$$b_2 = S_{21}\, a_1 + S_{22}\, a_2 \qquad \text{..(A4.13b)}$$

$$b_3 = S_{33}\, a_3 + S_{34}\, a_4 \qquad \text{..(A4.13c)}$$

$$b_4 = S_{43}\, a_3 + S_{44}\, a_4 \qquad \text{..(A4.13d)}$$

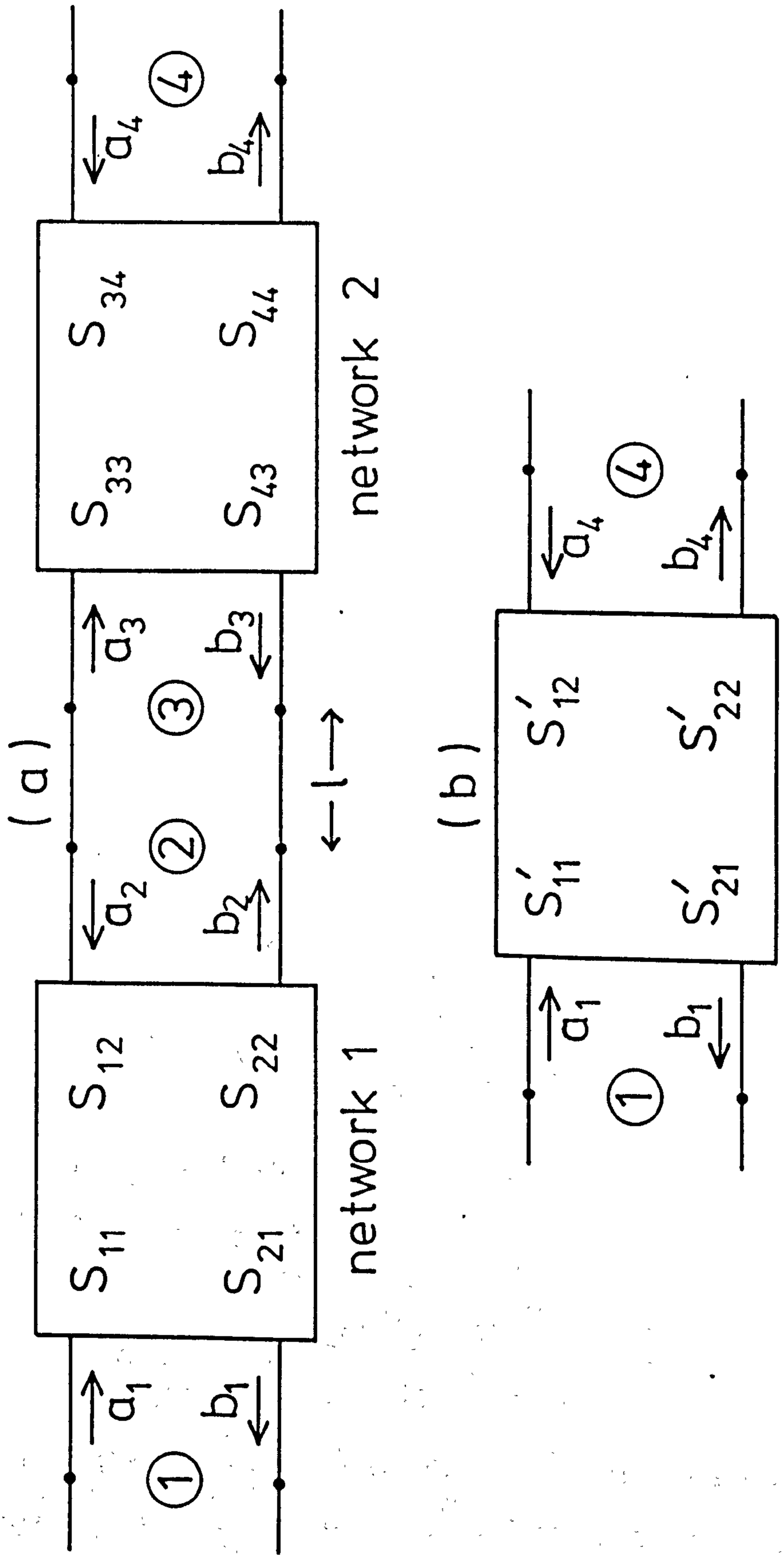

Cascaded two-port networks connected by a length, l, of transmission line:
(a) actual system; (b) overall system.

Figure A4.2.

and for the overall system

$$b_1 = S_{11}' a_1 + S_{12}' a_4$$

$$b_4 = S_{21}' a_1 + S_{22}' a_4$$

Since ports 2 and 3 are connected together we have:

$$a_3 = b_2 e^{-j\beta\ell} \quad \text{..(A4.14a)}$$

$$a_2 = b_3 e^{-j\beta\ell} \quad \text{..(A4.14b)}$$

where β is the phase change coefficient of the connecting transmission line = $2\pi/\lambda_{line}$. S_{11}' and S_{21}' are found by terminating port 4 by its characteristic impedance, so that $a_4 = 0$; then $S_{11}' = b_1/a_1$ and $S_{21}' = b_4/a_1$. Putting Equations (A4.14) in Equations (A4.13) and re-arranging gives

$$S_{21}' = S_{12}' = \frac{S_{21} S_{43} e^{-j\beta\ell}}{1 - S_{22} S_{33} e^{-2j\beta\ell}}$$

and

$$S_{11}' = S_{11} + \frac{S_{21} S_{12} S_{33} e^{-2j\beta\ell}}{1 - S_{22} S_{33} e^{-2j\beta\ell}}$$

Similarly S_{22}' is found by terminating port 1 by its characteristic impedance so that $a_1 = 0$ giving

$$S_{22} = S_{44} + \frac{S_{43} S_{34} S_{22} e^{-2j\beta\ell}}{1 - S_{22} S_{33} e^{-2j\beta\ell}}$$

Note that the above equations assume that the interconnecting line between the two networks is lossless. If the line is in fact lossy (corresponding to some absorption by the substrate) then the phase change term $j\beta$ should be replaced by $\alpha + j\beta$ where α is an attentuation coefficient.

A4.3 Scattering coefficients of the two-port networks

It is necessary to find the scattering coefficients of the two types of two-port networks which form the overall transmission line system representing the absorbing substrate. Referring back to Figure (A4.2a), network 1 consists of the interface between two transmission lines. From standard transmission line theory

$$R_{12} = \frac{Z_2 - Z_1}{Z_2 + Z_1}$$

$$\tau_{12} = \frac{2\,Z_2}{Z_1 + Z_2}$$

where R_{12} is the voltage reflection coefficient and τ_{12} is the voltage transmission coefficient of a wave travelling from medium 1 to medium 2. By Equations (A4.9), (A4.10), (A4.11) and (A4.12), the scattering coefficients for the network are:

$$S_{11} = \frac{Z_2 - Z_1}{Z_2 + Z_1}$$

$$S_{12} = \left[\frac{\text{Re } Z_1}{\text{Re } Z_2}\right]^{\frac{1}{2}} \cdot \frac{2\,Z_2}{Z_1 + Z_2}$$

$$S_{21} = S_{12}$$

$$S_{22} = \frac{Z_1 - Z_2}{Z_1 + Z_2}$$

The second network (network 2 in Figure (A4.2a)) is formed by the shunt impedance Z_F of an absorbing film between two transmission lines. Figure (A4.3) shows the equivalent circuit where Y_1, Y and Y_2 are the admittances of medium 1, the absorbing film and medium 2 respectively. S_{11} is equal to the reflection coefficient ρ at port 1.

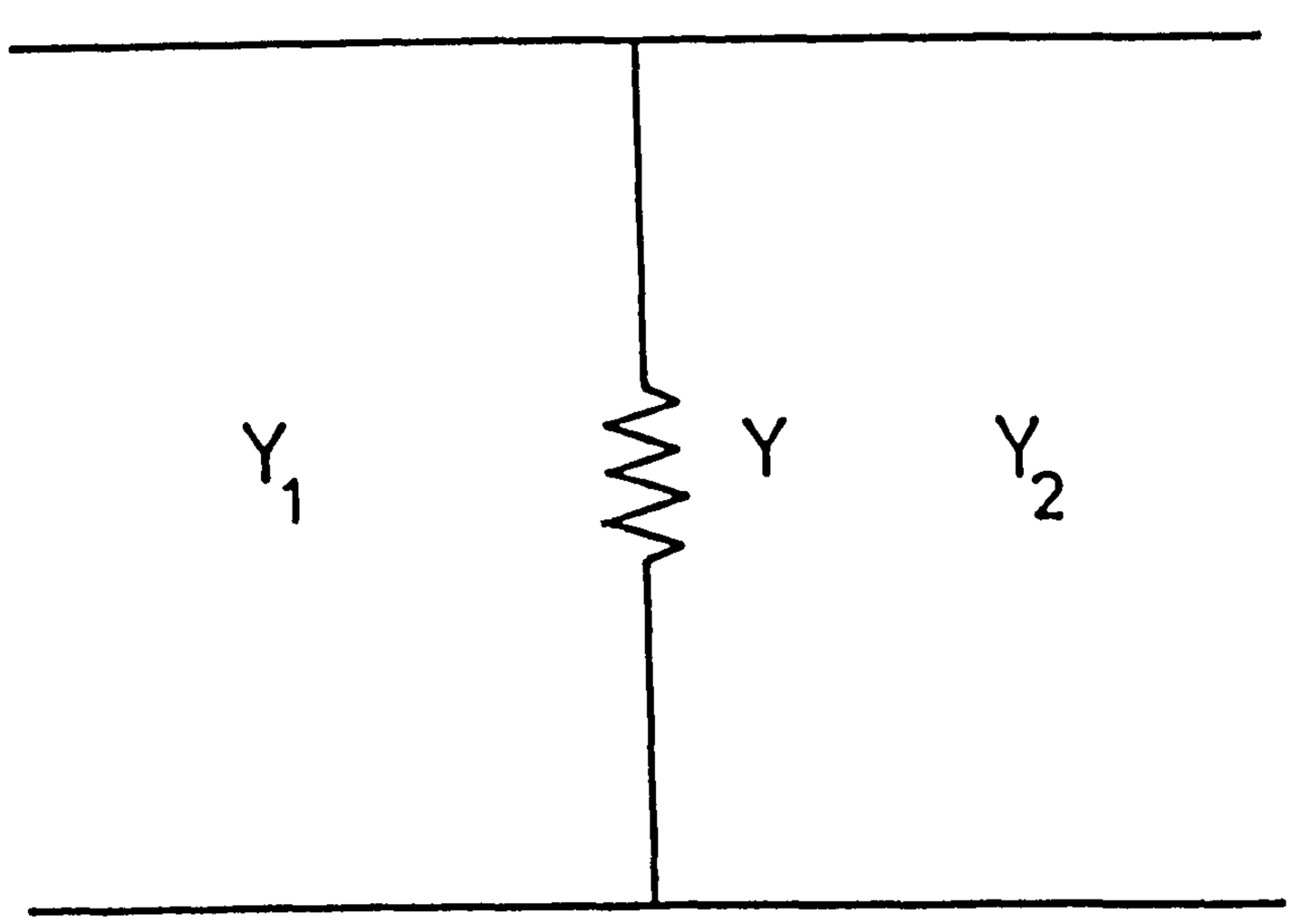

Figure A4.3. Equivalent circuit of medium 1, absorbing film and medium 2 interface.

Thus

$$\rho = S_{11} = \frac{Y_1 - (Y+Y_2)}{Y_1 + (Y+Y_2)}$$

Assume Y_1 and Y_2 to be real. As the voltage on either side of the admittance Y must be real,

$$V_1 = V_2$$

or $$V_{a_1} + V_{b_1} = V_{b_2} \qquad ..(A4.15)$$

From Equations (A4.5) etc., Equation (A4.15) becomes

$$(a_1 + b_1) \left[\frac{Y_2}{Y_1}\right]^{\frac{1}{2}} = b_2$$

Dividing through by a_1 and re-arranging yields

$$\frac{b_2}{a_1} = S_{21} = (1 + \rho) \left[\frac{Y_2}{Y_1}\right]^{\frac{1}{2}}$$

$$= \frac{2\ (Y_1\ Y_2)^{\frac{1}{2}}}{Y_1 + Y_2 + Y}$$

Similarly

$$S_{22} = \frac{Y_2 - (Y+Y_1)}{Y_2 + (Y+Y_1)}$$

and $$S_{12} = \frac{2\ (Y_2\ Y_1)^{\frac{1}{2}}}{Y_1 + Y_2 + Y} = S_{21}$$

A4.4 Effects of non-perpendicular incidence

The effect of non-perpendicular incidence depends on the polarisation of the incident wave. With the plane of incidence as the reference plane, the incident wave (or its appropriate component) is perpendicularly polarised when the incident electric field is

perpendicular to the reference plane and of parallel polarisation when the incident electric field is parallel to the plane of incidence (see Figures (A4.4a) and (A4.4b)). Note that for both cases, by Schnell's law

$$\frac{\sin \theta_i}{\sin \theta_t} = \frac{n_2}{n_1}$$

where n_1 and n_2 are the refractive indices of medium 1 and medium 2 respectively.

The transmission line analogue is concerned only with propagation in the z-direction. The wave impedance in the z-direction for a perpendicularly polarised wave is[1] $Z \sec \theta$ where θ is the angle between the actual direction of the wave and the z-direction. For a wave of parallel polarisation the wave impedance in the z-direction is $Z \cos \theta$.

For both parallel and perpendicular polarisation, the effective phase change coefficient for the component travelling in the z-direction will be $\beta \cos \theta$ and the attenuation coefficient $\alpha/\cos \theta$ where β and α are the phase change and attenuation coefficients of the plane wave in the medium.

A4.5 Calculation of wave impedance from the refractive index

It can be shown[1] that for both parallel and perpendicularly polarised electromagnetic waves that, provided the refractive index is real,

$$\varepsilon^{\frac{1}{2}} = n \qquad \ldots(A4.16)$$

where ε is the relative permeability of the medium and n the refractive index. For a non-magnetic material

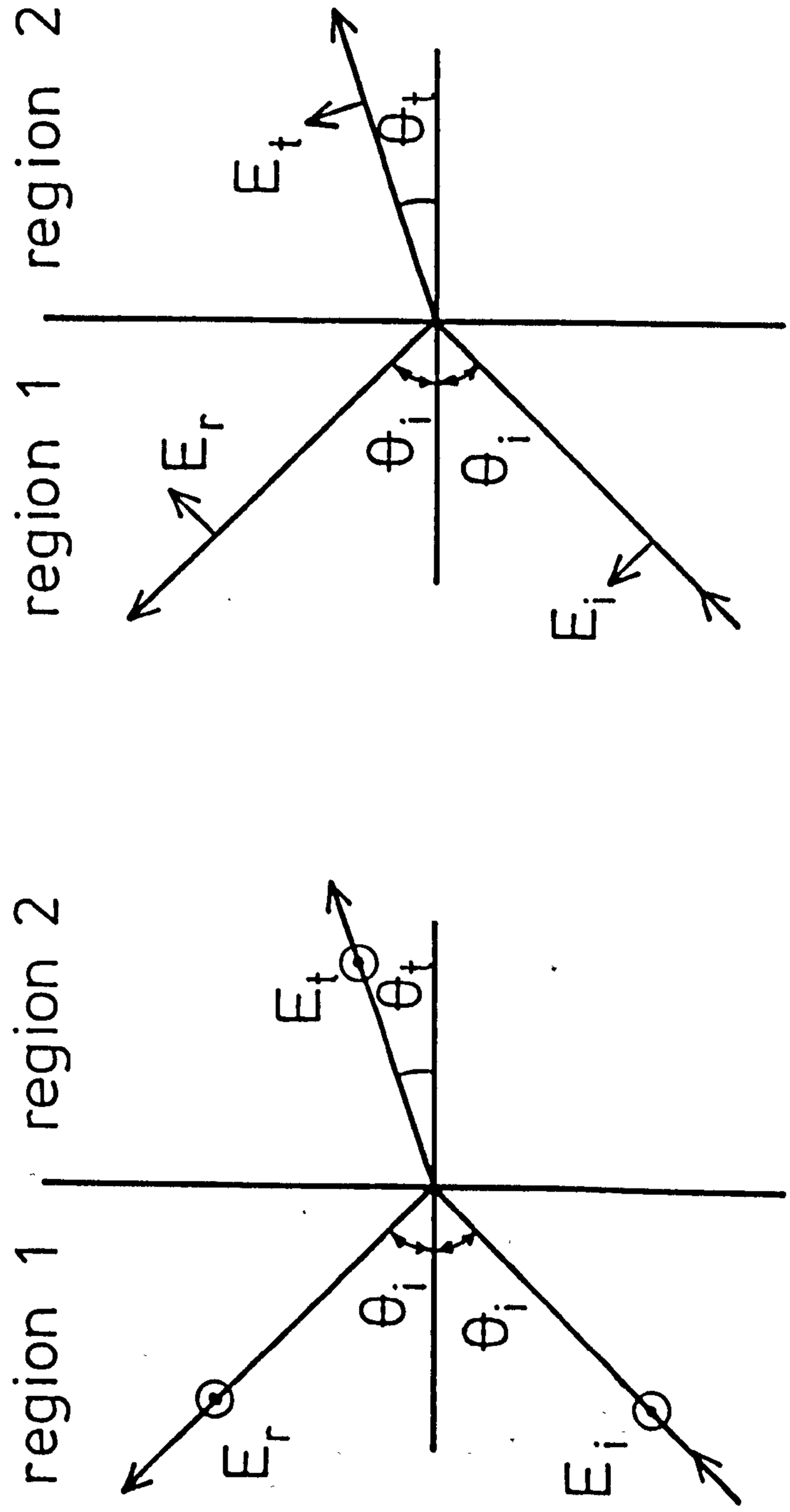

Figure A4.4. Plane wave reflection and transmission for (a) perpendicular polarisation and (b) parallel polarisation.

$$Z = \left[\frac{\mu_o}{\varepsilon\ \varepsilon_o}\right]^{\frac{1}{2}} = \frac{Z_o}{\varepsilon^{\frac{1}{2}}}$$

where Z_o is the impedance of free space. Therefore by Equation (A4.16)

$$Z = \frac{Z_o}{n}\ .$$

APPENDIX IV

REFERENCES

(1) Staniforth, J.A. "Microwave Transmission" published by the English Universities Press Ltd., pp. 64 (1972).

APPENDIX V

Computer program (SUB) used to compute theoretical transmission line analogue spectra

Program SUB calculates the fractional transmission T, reflection R, and absorption A in the FIR in 1 cm^{-1} intervals for a dielectric substrate with plane parallel surfaces coated on one surface with an absorbing metal film. The program can be used for radiation incident on either the coated or uncoated surface of the substrate. The program is written in FORTRAN.

The first twenty four spaces of the first line of the data input is read in using A-format and can be used to give information on the output of the type of substrate, the substrate temperature and whether data values for an ordinary or extra-ordinary ray are being used. The second line is read in in integer format and if equal to 1 will result in the program calculating values for the radiation incident on the uncoated surface of the substrate. If set to any other integer value, the program will calculate T, R and A for radiation incident on the coated surface of the substrate. Line three gives the substrate thickness in metres in E-format, the film impedance/square and the angle of incidence of the incident radiation in radians (note: the program assumes the incident plane wave is a transverse electric wave. However for perpendicular incidence, the spectra will be identical for transverse electric and transverse magnetic waves). Line five is read in in floating-point format and gives the frequency limits for the output listing of R, T and A. Line six gives the number of data points to be read in, i.e. the number of values of refractive index (n) and absorption coefficient (α) given in line seven onwards. With line

four set to 1, the program requires a value of n and α for every 10 cm^{-1} covered by the frequency limits given in line five. The reason for this is that the program only changes the value of n and α every 10 cm^{-1} as, generally, n and α are slowly varying quantities with frequency[1]. However, if values are being calculated for a quartz substrate, α is not always a slowly varying quantity with frequency[1], having a sharp feature centred at 128 cm^{-1} which is particularly pronounced at room temperature. Therefore the program has provision for changing the values of n and α more rapidly between 120 cm^{-1} and 140 cm^{-1} and if line four is set to an integer other than 1, the program requires values of n and α every 2.5 cm^{-1} between 120 cm^{-1} and 140 cm^{-1}.

```
      PROGRAM(SUB)
C PROGRAM CALCULATES TRANSMISSION,REFLECTION AND ABSORPTION
C OF SUBSTRATE WITH FILM FACING LAMP IF L=O OR WITH
C SUBSTRATE FACING LAMP IF L=1
      COMPLEX D,SS11,SS12,G,CAL
      DIMENSION B(500),W(500),AN(500),ABS(500),ABS1(50)
     C,AN1(50),NAME(6)
      READ(6,13)NAME
      READ(6,14)L
14    FORMAT(I1)
13    FORMAT(6A4)
      READ(6,6)AL,Z,AINC
      READ(6,22)MN
22    FORMAT(I1)
6     FORMAT(E10.2,2F0.0)
39    FORMAT(1H ,E8.2,5X,F5.1,5X,F5.2)
      READ(6,17)W1,W2
      W1=W1+.000001
      W2=W2+.000001
17    FORMAT(2F0.0)
      IW1=IFIX(W1)
      IW2=IFIX(W2)
      W(IW1)=W1
      DO 32 I=IW1,IW2-1
32    W(I+1)=W(I)+1
1     FORMAT(1H ,F10.5)
      READ(6,102)M
102   FORMAT(I2)
      DO 101 I=1,M
      READ(6,2)AN1(I),ABS1(I)
      ABS1(I)=ABS1(I)*100.0
2     FORMAT(2F0.0)
101   CONTINUE
      I=0
      DO 64 J=IW1,IW2
      IF(MN.EQ.1)GO TO 61
      IF(J.LE.120)GO TO 61
      IF(J.GE.140)GO TO 61
      IF(J.EQ.123)I=I+1
      IF(J.EQ.125)I=I+1
      IF(J.EQ.128)I=I+1
      IF(J.EQ.130)I=I+1
      IF(J.EQ.133)I=I+1
      IF(J.EQ.135)I=I+1
      IF(J.EQ.138)I=I+1
      GO TO 63
61    IF((J/10)*10.EQ.J)I=I+1
63    AN(J)=AN1(I)
      ABS(J)=ABS1(I)/2.
64    CONTINUE
      ZO=377.*COS(AINC)
      IF(L.EQ.1)WRITE(2,69)
      IF(L.EQ.2)WRITE(2,70)
70    FORMAT(17H FILM FACING LAMP)
      WRITE(2,5)
5     FORMAT(1H )
```

```
69      FORMAT(22H SUBSTRATE FACING LAMP)
4       FORMAT(32H THICKNESS IMPEDANCE INC ANGLE)
        WRITE(2,7)NAME
        WRITE(2,5)
7       FORMAT(1H ,6A4)
        WRITE(2,4)
        WRITE(2,39)AL,Z,AINC
        WRITE(2,5)
        WRITE(2,9)
9       FORMAT(27H INITIAL FREQ     FINAL FREQ)
        WRITE(2,20)W1,W2
20      FORMAT(1H ,F7.1,10X,F7.1)
        WRITE(2,5)
        WRITE(2,8)
8       FORMAT(31H WAVE NO     REFL     TRANS     ABS)
        DO 37 I=IW1,IW2
        IF(L.EQ.1)GO TO 100
        CALL FRONT(AINC,AN(I),ZO,Z,W(I),ABS(I),B(I),AL,A,R,T)
        GO TO 103
100     CALL BACK(AINC,AN(I),ZO,Z,W(I),ABS(I),B(I),AL,A,R,T)
103     WRITE(2,37)W(I),R,T,A
37      FORMAT(1H ,F5.1,3X,3F8.3)
        STOP
        END
        SUBROUTINE FRONT(AINC,AN,ZO,Z,W,ABS,B,AL,A,R,T)
        COMPLEX D,SS11,SS12,G,CAL
        AINCS=ASIN(SIN(AINC)/AN)
        ZS=(377./AN)*COS(AINCS)
        YS=1./ZS
        YO=1./ZO
        Y=1./Z
        X=YS+Y+YO
        S11=(YO-Y-YS)/X
        S21=2.*SQRT(YO*YS)/X
        S12=S21
        S22=(YS-Y-YO)/X
        ZX=ZO+ZS
        S33=(ZO-ZS)/ZX
        S44=-S33
        S34=2.*ZO*SQRT(ZS/ZO)/ZX
        S43=S34
        B=200.*3.142*AN*COS(AINCS)*W
        G=CMPLX(ABS,B)
        CAL=CMPLX(AL,0.)
        D=CEXP(-2.*G*CAL)
        SS11=CMPLX(S11,0.)+CMPLX(S21*S12*S33,0.)*D/
      C(1.-CMPLX(S22*S33,0.)*D)
        SS12=CMPLX(S21*S43,0.)*CEXP(-G*CAL)/
      C(1.-CMPLX(S22*S33,0.)*D)
        SS11=SS11*CONJG(SS11)
        SS12=SS12*CONJG(SS12)
        R=REAL(SS11)
        T=REAL(SS12)
        A=1.-R-T
        RETURN
        END
```

```
      SUBROUTINE BACK(AINC,AN,ZO,Z,W,ABS,B,AL,A,R,T)
      COMPLEX D,SS11,SS12,G,CAL
      AINCS=ASIN(SIN(AINC)/AN)
      ZS=(377./AN)*COS(AINCS)
      S11=(ZS-ZO)/(ZS+ZO)
      S22=-S11
      S12=2.*(ZS/(ZS+ZO))*SQRT(ZO/ZS)
      S21=2.*(ZO/(ZS+ZO))*SQRT(ZS/ZO)
      YS=1./ZS
      YO=1./ZO
      Y=1./Z
      X=YS+Y+YO
      S33=(YS-Y-YO)/X
      S44=(YO-Y-YS)/X
      S43=2.*SQRT(YS*YO)/X
      S34=S43
      B=200.*3.142*AN*COS(AINCS)*W
      G=CMPLX(ABS,B)
      CAL=CMPLX(AL,0.)
      D=CEXP(-2.*G*CAL)
      SS11=CMPLX(S11,0.)+CMPLX(S21*S12*S33,0.)*D/
     C(1.-CMPLX(S22*S33,0.)*D)
      SS12=CMPLX(S21*S43,0.)*CEXP(-G*CAL)/
     C(1.-CMPLX(S22*S33,0.)*D)
      SS11=SS11*CONJG(SS11)
      SS12=SS12*CONJG(SS12)
      R=REAL(SS11)
      T=REAL(SS12)
      A=1.-R-T
      RETURN
      END
      FINISH
```

Sample data input:

```
SAPPHIRE 1.5K O-RAY
1
0.60E-4     210.     0.
1
10. 200.
18
3.052 .1
3.052 .1
3.052 .1
3.055 .1

etc.
```

Sample output listing:

FILM FACING LAMP

SAPPHIRE 1.5K O-RAY

THICKNESS	IMPEDANCE	INC ANGLE
0.60E-04	210.0	0.00

INITIAL FREQ	FINAL FREQ
10.0	200.0

WAVE NO	REFL	TRANS	ABS
10.0	0.624	0.258	0.119
11.0	0.657	0.256	0.087
12.0	0.681	0.255	0.064
13.0	0.694	0.254	0.052

etc.

APPENDIX V

REFERENCES

(1) Loewenstein, E.V., D. R. Smith and R. L. Morgan, Appl. Optics, 12, No. 2, 398 (1972).

ACKNOWLEDGEMENTS

I wish to acknowledge my indebtedness to all the academic and technical staff in the Department of Physics, Queen Mary College, particularly Dr. P. E. Clegg, my supervisor, for his encouragement and advice throughout this work, especially with regard to the development of the theoretical understanding of the detectors produced for this thesis.

I should also like to thank Professor J. A. Bastin for enabling me to use the excellent facilities in the Physics Department; Dr. P. A. R. Ade for his advice and assistance in many experiments performed for this work; Mr. D. G. Vickers for his excellent technical assistance and encouragement; Mr. S. Shyllon for allowing me to use the evaporating facilities under his charge; the low-temperature services department headed by Mr. A. Marston for the supply of cryogenic liquids; Mr. S. Adams and Miss A. Boswell for their assistance in preparing many of the figures and Mrs. M. Puplett for her typing of this thesis.

FABRICATION OF Q.M.C. SUPERCONDUCTING TRANSITION-EDGE BOLOMETERS

by

M. S. F. DUNN

Department of Physics
Queen Mary College

March 1980

Introduction

This report describes the fabrication of a Q.M.C. superconducting transition-edge bolometer using a sapphire substrate and a Tin (Sn) film on it's superconducting transition as a temperature sensor. The bolometer is shown in Figure 1. The bolometer was held on the superconducting transition of the Sn film using a servo-regulating mechanism to control the temperature of the bolometer element by adjusting the bias current through a Bismuth (Bi) film deposited between an additional pair of Indium (In) contacts on the substrate. A Bi film with an impedance of approximately 180 Ω/square was deposited on the other surface of the substrate to act as an absorber for incident signal radiation (60 μm thick sapphire at ^{4}He temperatures is almost transparent to millimetre wavelength radiation).

Electrical contact to the films on the substrate was made through Copper (Cu)/Lead (Pb)-coated 60 μm thick nylon leads stretched across an anodised Aluminium (Al) mount. Electrical and mechanical contact between the leads and the Sn and Bi films on the substrate was made using Indium cold-welding reinforced by G.E.7031 varnish.

Evaporation onto the sapphire substrate

The 5.0 mm diameter by 60 μm thick sapphire substrate was cleaned as follows:

It was first washed in a dilute solution of Teepol using a fine brush. The substrate was then held with a pair of No. 5 tweezers (thoroughly cleaned) and rinsed by agitating in distilled water. Still held with the tweezers, the substrate was then immersed and agitated in trichloroethylene, acetone and then chloroform for several minutes in each. It was then placed on the substrate support of the substrate

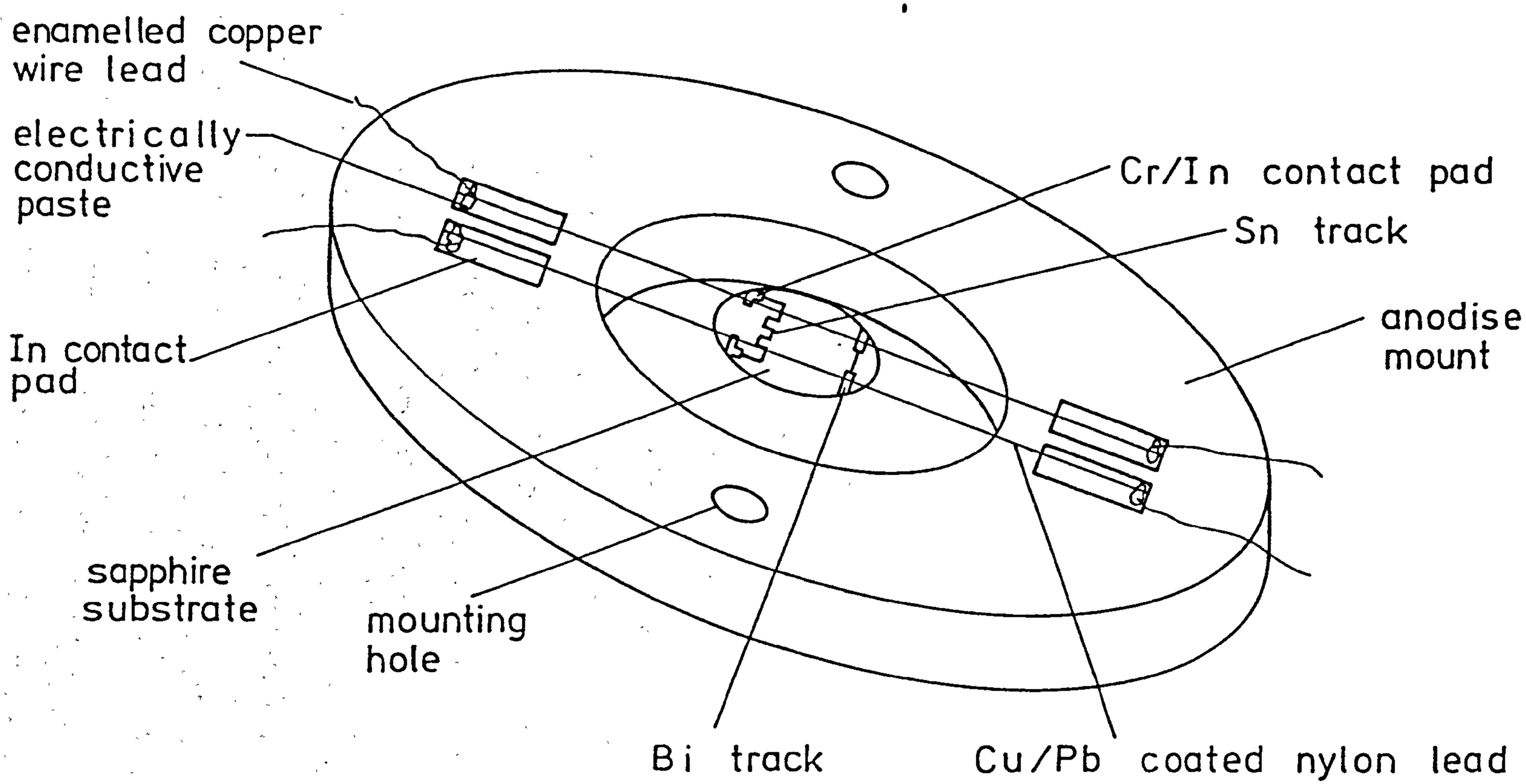

Figure 1. The bolometer.

holder illustrated in Figure 2. Note that the support had to be thoroughly cleaned (with chloroform) before the substrate was placed on it because the surface of the substrate lying against the support would eventually be coated with a Bi film. The height adjustment screw for the substrate support was adjusted so that the surface of the substrate was just below the upper surface of the holder. The substrate locating clamp adjustment screw was then screwed in until the substrate was firmly held in place. After being thoroughly cleaned in trichloroethylene, acetone and chloroform, the mask for evaporating the Chromium (Cr)/In contacts (see Figure 3(a)) was placed over the locating pins on the substrate holder and clamped in place.

The masks used for evaporation onto the sapphire substrate were produced using photo-etching techniques and were all made from 1 thou brass shim. This thickness was necessary to be able to produce masks with track widths down to 100 μm. It is possible to produce masks with narrower track widths but it was found that below 100 μm width the tracks tended to become clogged with dust before they could be mounted on the substrate holder and pumped down in the evaporator.

The substrate holder was then mounted in the evaporator and pumped down to a pressure of $< 10^{-5}$ Torr. Two sources were used for this evaporation; one for the 1000 Å thick Cr film (the first film evaporated) and one for the 2 μm thick In film. The source used for the Cr evaporation was a coiled tungsten basket holding a bead of Cr. In this and all subsequent evaporations the evaporants were of spectrographically pure grade. The source used for the In evaporation was a molybdenum boat holding the required quantity of In wire.

Prior to actually mounting the substrate holder and pumping down

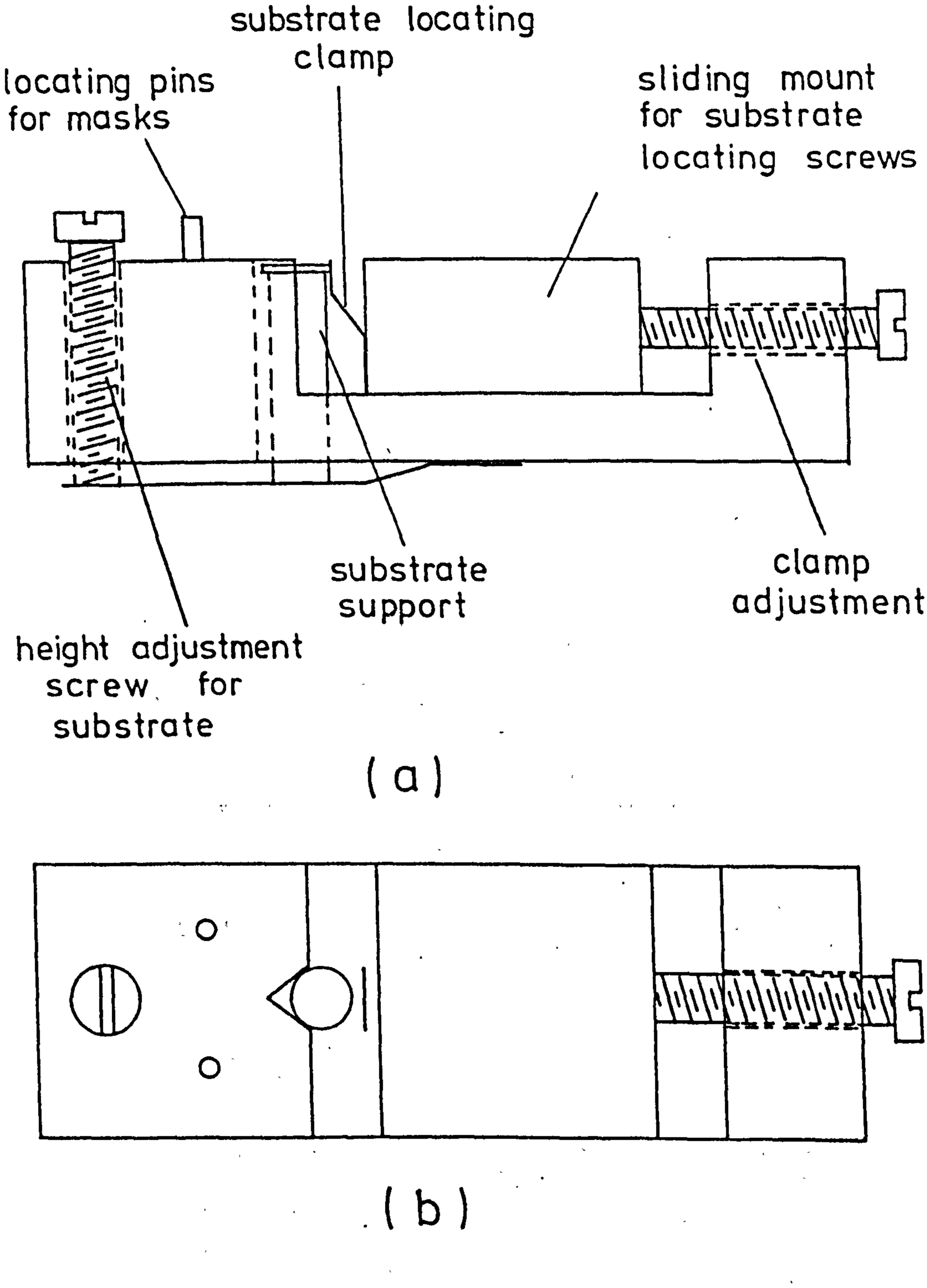

Figure 2. (a) side view and (b) plan view of substrate holder used for evaporating onto the substrate.

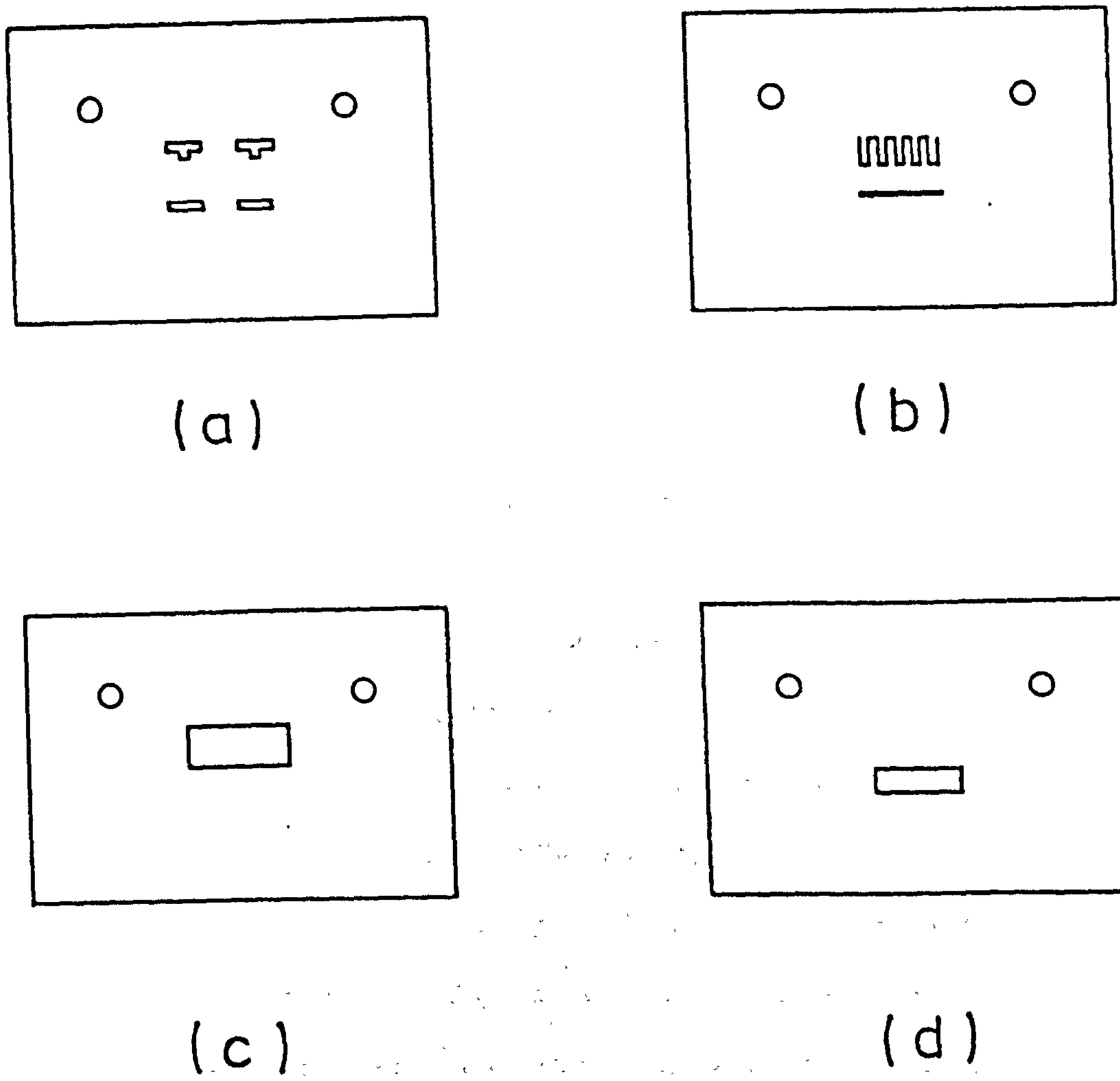

Figure 3. Masks used for evaporating onto substrates.

to evaporate these films onto the substrate, the evaporator had been pumped down to a pressure of 10^{-5} Torr and the sources outgassed by heating them up to red heat for a few seconds.

Using the source described above the Cr evaporation was very slow (≃ 1 Å/sec.) resulting in an evaporation lasting nearly twenty minutes. The large amount of heat produced by the source during this period caused a great deal of outgassing from the evaporation chamber, and therefore most of the evaporation was made at the relatively high pressure of ≃ 10^{-4} Torr. This was the best pressure that could be maintained by the evaporator pumping system for this rate of evaporation even though it used a six inch diameter LN_2-cooled diffusion pump. Nevertheless, similar thickness Cr films evaporated onto glass slides cleaned in the same way as the bolometer substrates had the required property of very good adhesion to the glass. Adhesion tests were performed by firmly pressing a piece of masking tape onto the film and then peeling it off. If none of the evaporated film peeled off with the tape the film was said to have good adhesion. If all the film peeled off with the masking tape the film was said to have poor adhesion.

After the Cr evaporation had been completed the evaporator was allowed to pump down again to 10^{-5} Torr and then the In film was deposited at a rate of ≃ 1000 Å/sec. and at an average pressure of 3×10^{-5} Torr.

The evaporator was then vented and mask (a) (see Figure 3) was replaced by (cleaned) masks (b) and (c) with (b) next to the substrate ready for the Sn evaporation. The source used for Sn films was a molybdenum boat holding the required quantity of Sn. The Sn evaporation was started at a pressure of ≃ 3×10^{-6} Torr and, at an evaporation

rate of ≃ 100 Å/sec., took place at an average pressure of 10^{-5} Torr.

It was then necessary to evaporate the Bi heater using masks (b) and (d). As the relevant parameter in Bi film evaporations was the resistance/square of the film, Bi films were evaporated to a given resistance/square rather than thickness. To produce a Bi track with a resistance of ≃ 2kΩ at ^{4}He temperatures required a Bi evaporation of ≃ 40 Ω/square. The glass slide used to measure the resistance/square of the film was cleaned in the same way as the sapphire substrates and coated with a 1000 Å thick Al film (using a coiled tungsten boat) on either end leaving a square-shaped region in the middle with no film evaporated. As the film was being deposited, the resistance between the Al contacts could be monitored directly using a digital voltmeter (D.V.M.)

Bolometer mount fabrication

The bolometer mount was fabricated from 16 s.w.g. Al sheet as sheet Aluminium is relatively free from impurities making it well suited to anodising. The mount was ring-shaped with an outside diameter of 25 mm and an inside diameter of 10 mm. Two 2 mm diameter holes in the ring were used to attach the mount to the cryostat heat sink fittings. Care had to be taken in the preparation of the mount before anodising and in the choice of the method of anodising to make sure there were no pinholes in the anodised layer which could short out films evaporated onto the mount. The preparation procedure used was as follows:

The inside edges of the mount were cut away using a clean knife to remove any impurities which had become embedded in the surface of the mount during machining. All edges on the mount were then rounded

off using a clean needle file. The surfaces of the mount were lapped first with grade 0 emery cloth followed by progressively finer grades of polishing paper down to 3/0 grade.

The mount was then thoroughly washed in parafin. From this point on the mount was only handled with clean tweezers. Next it was cleaned and left to soak for several minutes in trichloroethylene and then rinsed in acetone and chloroform, followed by immersion in a boiling NaOH bath for 30 seconds. The concentration used for the bath was 10 pellets of NaOH per 100 ml of water. Leaving the mount in the NaOH bath for this length of time resulted in a negligible reduction in the dimensions of the mount (e.g. less than 25 μm off the outside diameter). After etching in the NaOH bath, the mount was rinsed in distilled water and kept in pure alcohol until required for anodising.

Chromic acid anodising was used as it was found to give much less of a problem with pinholes in the oxide film than sulphuric acid processes. The chromic acid was produced by mixing the following materials in the same relative quantities: 1 ℓ conc. H_2SO_4; 1 kg potassium dichromate; 8 ℓ distilled water. The electrolyte actually used was the above chromic acid solution diluted by 2 parts distilled water to 1 part acid. The mount was connected to the positive terminal of a d.c. constant current supply and a steel electrode to the negative terminal. Electrical connection to the mount and steel electrode was made using steel crocodile clips *above* the surface of the electrolyte leaving a small area of the mount around one of the fixing holes unanodised.

The voltage across the power supply terminals was built up steadily from zero at a rate of 1 Volt/minute until the current flowing was 50 mA (≃ 20 Volts across the power supply terminals). The

anodising process was allowed to continue for approximately 1 hour by which time the voltage across the power supply terminals had risen to about 24 Volts. The mount was then removed from the bath and rinsed in distilled water and then alcohol. The above process gave the mount a smooth, very durable finish with no pinholes in the anodised layer.

Evaporation onto the nylon leads

It was necessary first of all to soak the nylon leads in a diluted Teepol solution for at least one day to remove the 0.3% TiO_2 de-lustrant. Before attaching the threads to the mount they were thoroughly rinsed in distilled water.

The jigs illustrated in Figure 4 were used to make sure that the nylon threads were correctly positioned while being glued to the mount. The leads were stretched across the frame shown in Figure 4(a) to a tension of 5 grms weight. Lines were scribed on the frame to make sure the leads were symmetrically positioned and 3.0 mm apart. The leads were attached to this frame with G.E. 7031 varnish.

The bolometer mount was placed in the centre hole of the lead support frame jig shown in Figure 4(b) with it's alignment marks opposite the appropriate scribed lines on the jig. Note that the surface of the bolometer mount was just proud of the surface of the jig. The lead support frame was then placed on the jig, orientated so that the nylon leads were aligned with the 3.0 mm apart scribed lines as shown in Figure 4(b). The leads could now be glued to the mount with G.E. 7031 varnish. After approximately 5 minutes the nylon leads were cut about 2 mm inside the outside diameter of the mount and the extraneous lengths pulled away. The leads were now ready for evaporation.

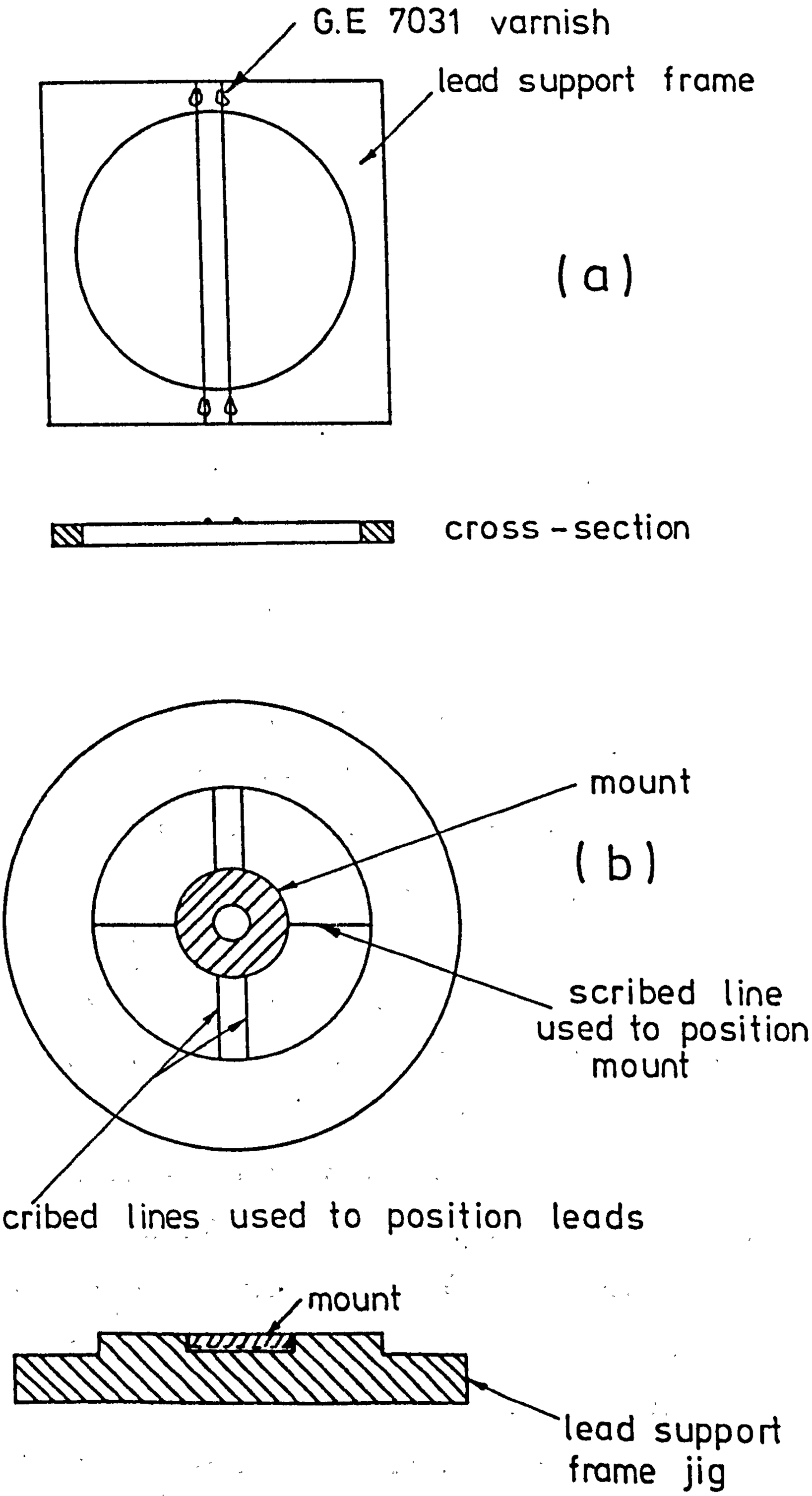

Figure 4. Jigs used to attach nylon leads to mount.

The tool shown in Figures 5 and 6 was used to hold the masks and mount in alignment for evaporation onto the leads. The plug was necessary to stop evaporation onto the inside surface of the mount thereby shorting out the contacts. Spacing washers 200 μm thick were used to ensure that the masks did not touch the nylon leads. The masks were produced using photo-etching techniques from 4 thou copper shim and are shown in Figure 7.

The first evaporation onto the nylon leads was the 400 Å Cu/ 1500 Å Pb deposition between the cold-welding contact areas and the mount. The masks used were those shown in Figures 7(a) and (b). Note that no Pb film was deposited on the areas where the In contacts were to be made as a Pb film under In resulted in a very poor In adhesion. A thorough cleaning of the masks before use was not necessary as they would not touch the leads. Molybdenum boats were used for both the Cu and Pb evaporations. The Cu evaporation was performed first at an average pressure of $\simeq 10^{-5}$ Torr and evaporation rate of $\simeq$ 50 Å/sec. The evaporator was then allowed to pump down again to 10^{-5} Torr and the Pb evaporated at an average pressure of $\simeq 3 \times 10^{-5}$ Torr and rate of $\simeq$ 100 Å/sec.

The evaporator was then vented and the Cu/Pb masks replaced by the masks used to evaporate the 400 Å Cu/2 μm In films on the contact areas (Figures 7(a) and (c)). The design of the masks ensured that there was a slight overlap of $\simeq$ 200 μm between the Cu/Pb and Cu/In deposition to make sure that there would be a continuous layer of conducting film along the leads between the cold-welded contacts and the Cu/In depositions on the mount. Molybdenum boats were used for both the Cu and In evaporations. The Cu evaporation was performed at an average pressure of $\simeq 10^{-5}$ Torr and rate of $\simeq$ 50 Å/sec. and the In evaporation at

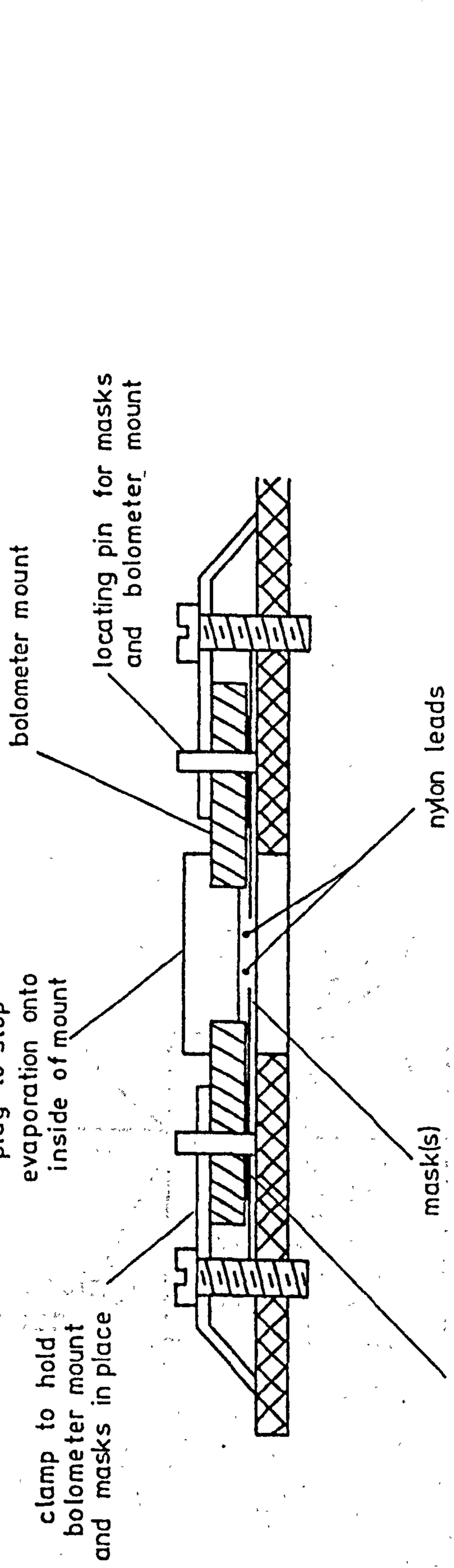

Figure 5. Sectional view of jig used for evaporations onto nylon leads

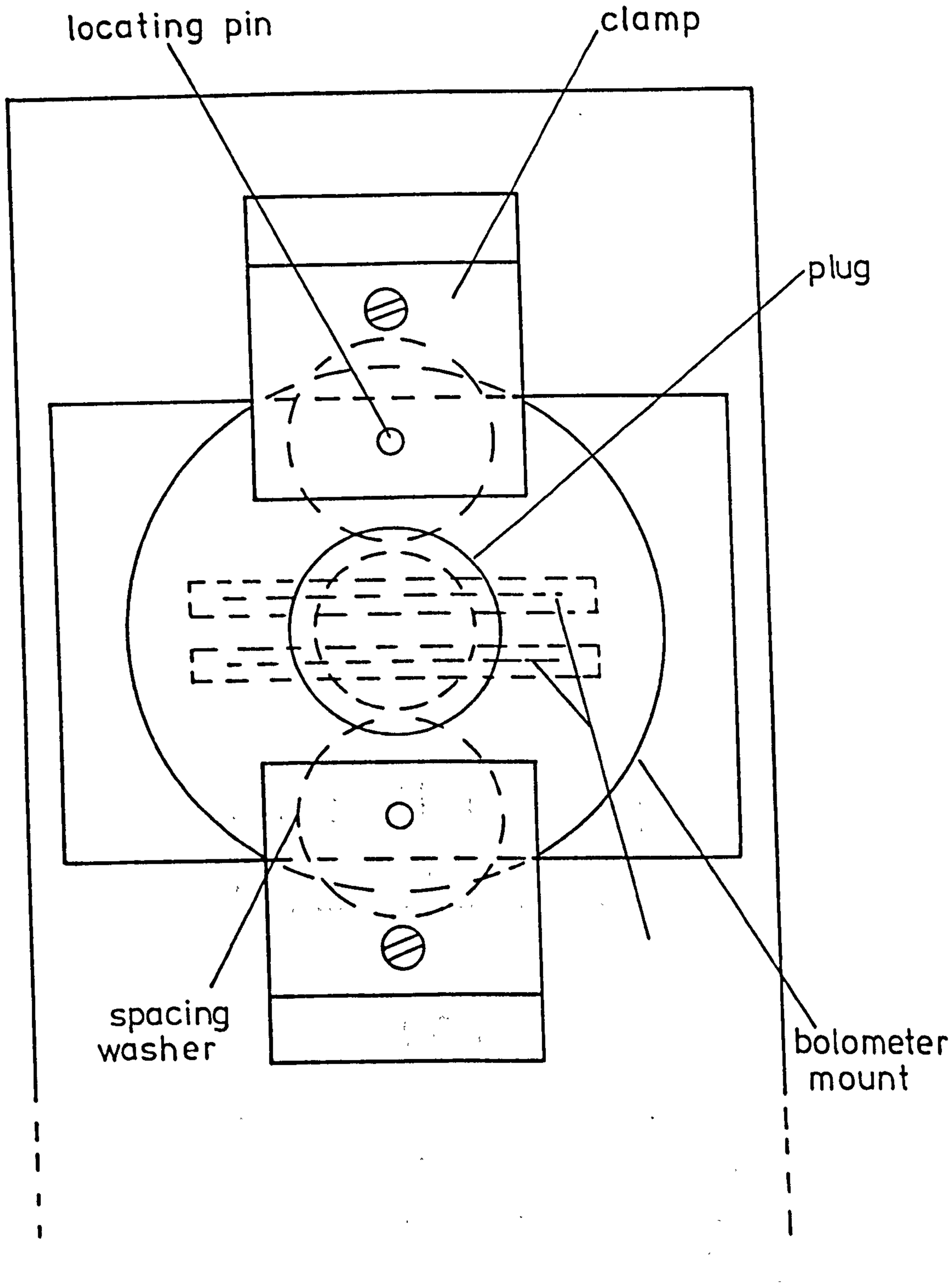

Figure 6. Plan view of jig used for evaporations onto nylon leads.

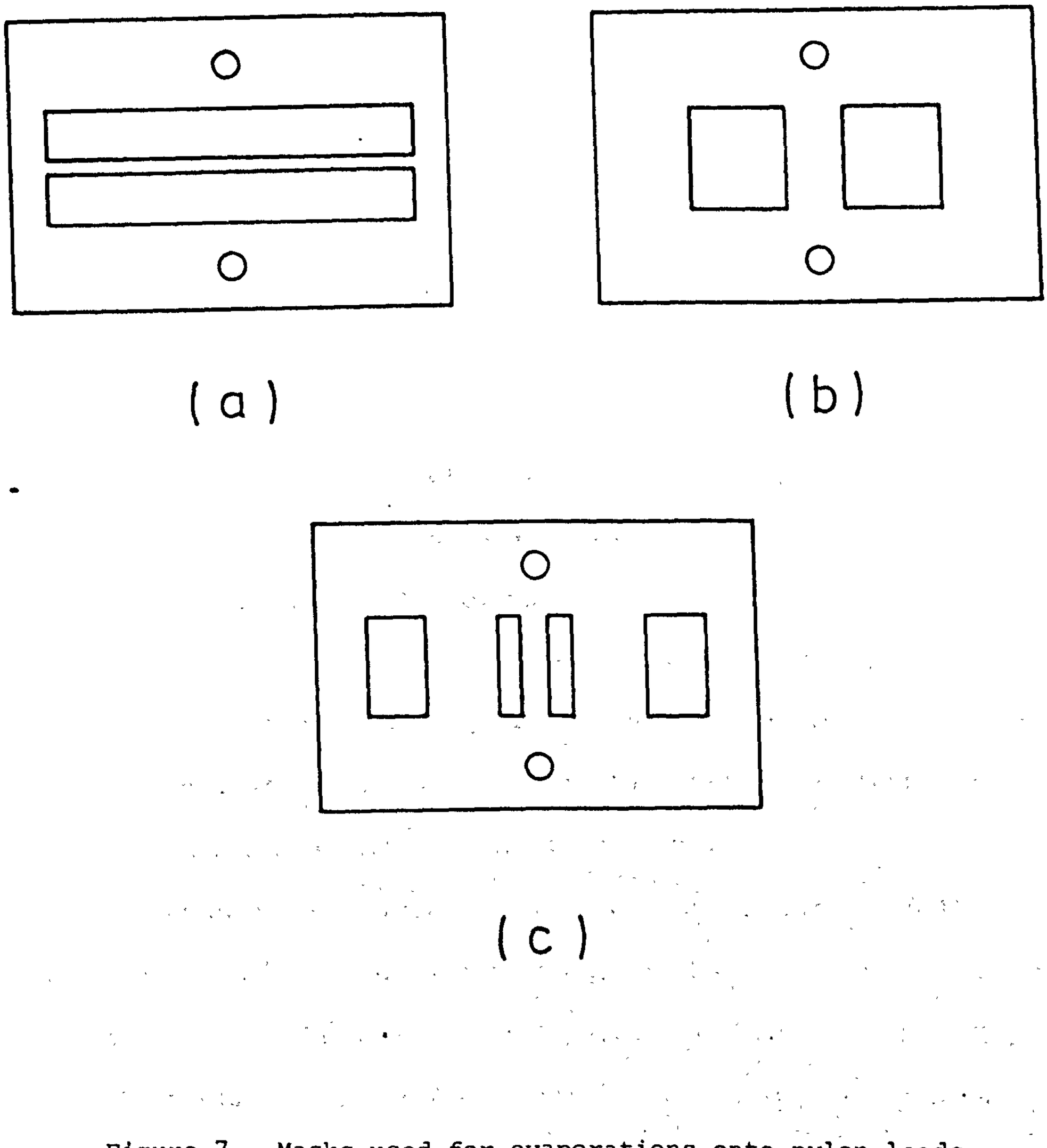

(a)

(b)

(c)

Figure 7. Masks used for evaporations onto nylon leads.

$\simeq 3 \times 10^{-5}$ Torr and $\simeq$ 1000 Å/sec.

Attachment of the nylon leads to the bolometer substrate

Electrical and mechanical contact between the nylon leads and the substrate was made by cold-welding the In films on the substrate and leads and glueing with G.E. 7031 varnish for extra mechanical strength. The following describes the method used:

The sapphire substrate was mounted in the jig shown in Figure 8. The surface of the jig supporting the substrate had previously been well cleaned with methylated spirits to prevent dirtying of the as yet uncoated surface of the substrate. It was important to align the sapphire substrate correctly with respect to the clamps (see Figure 9) to ensure that the leads could be placed across the substrate without being fouled or touched by the clamps.

The clamps were all made from phosphor bronze. Clamps 1 and 2 were made thick enough to be regarded as completely rigid. Clamp 3 was made thin enough to provide a spring loaded pressure against the substrate to reduce the chances of it breaking.

The bolometer mount (with leads attached) was placed in the mount holder shown in Figure 10. The slot across the surface supporting the mount ensured that the mount did not rest on the nylon leads. The mount holder was then lowered onto the substrate jig as shown in Figure 11. These tools were designed so that with the mount holder in position, the nylon leads were just touching the substrate. The leads and substrate were now in position for cold-welding. The entire process of attachment of the leads to the substrate was observed using a low power binocular microscope.

The cold-welding tool is illustrated in Figure 12. The holder for

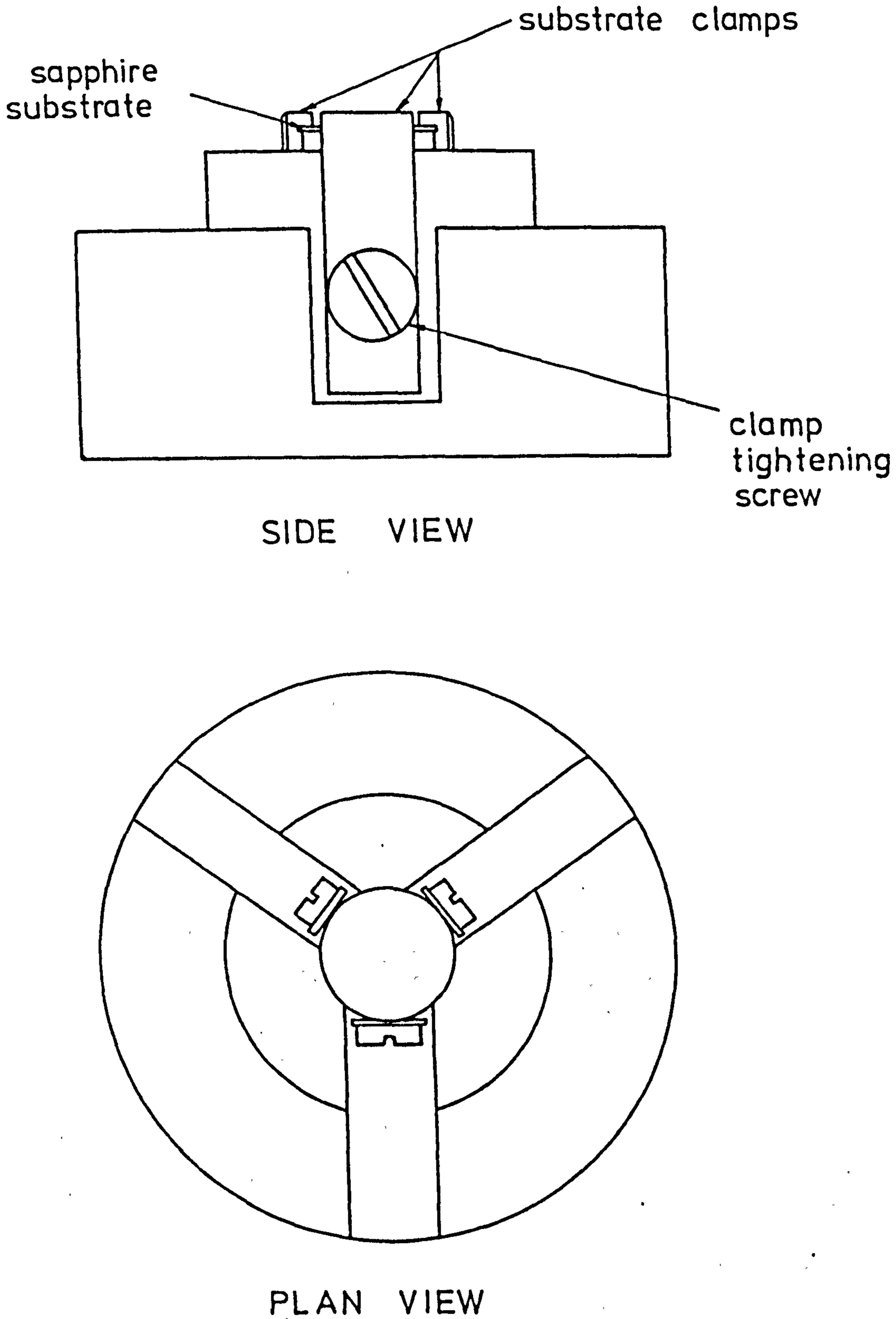

Figure 8. Side and plan views of jig used to hold sapphire substrate while nylon leads were being attached.

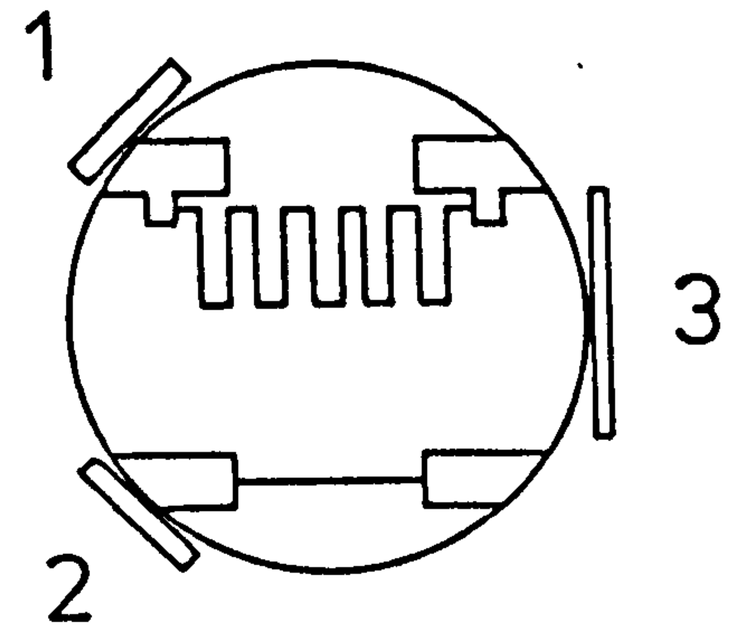

Figure 9. Alignment of substrate with respect to the locating clamps.

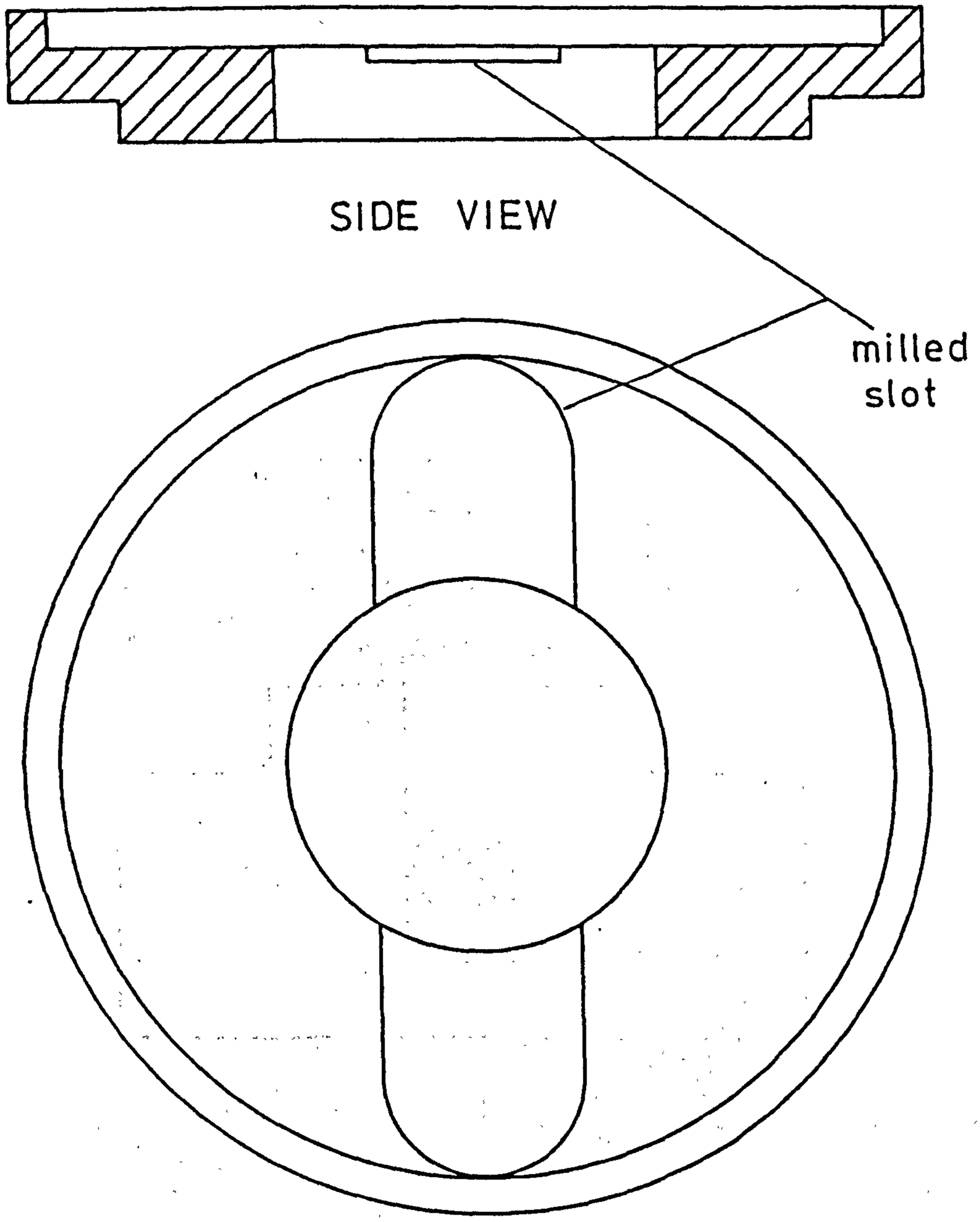

Figure 10. Bolometer mount holder used for cold-welding leads to the substrate.

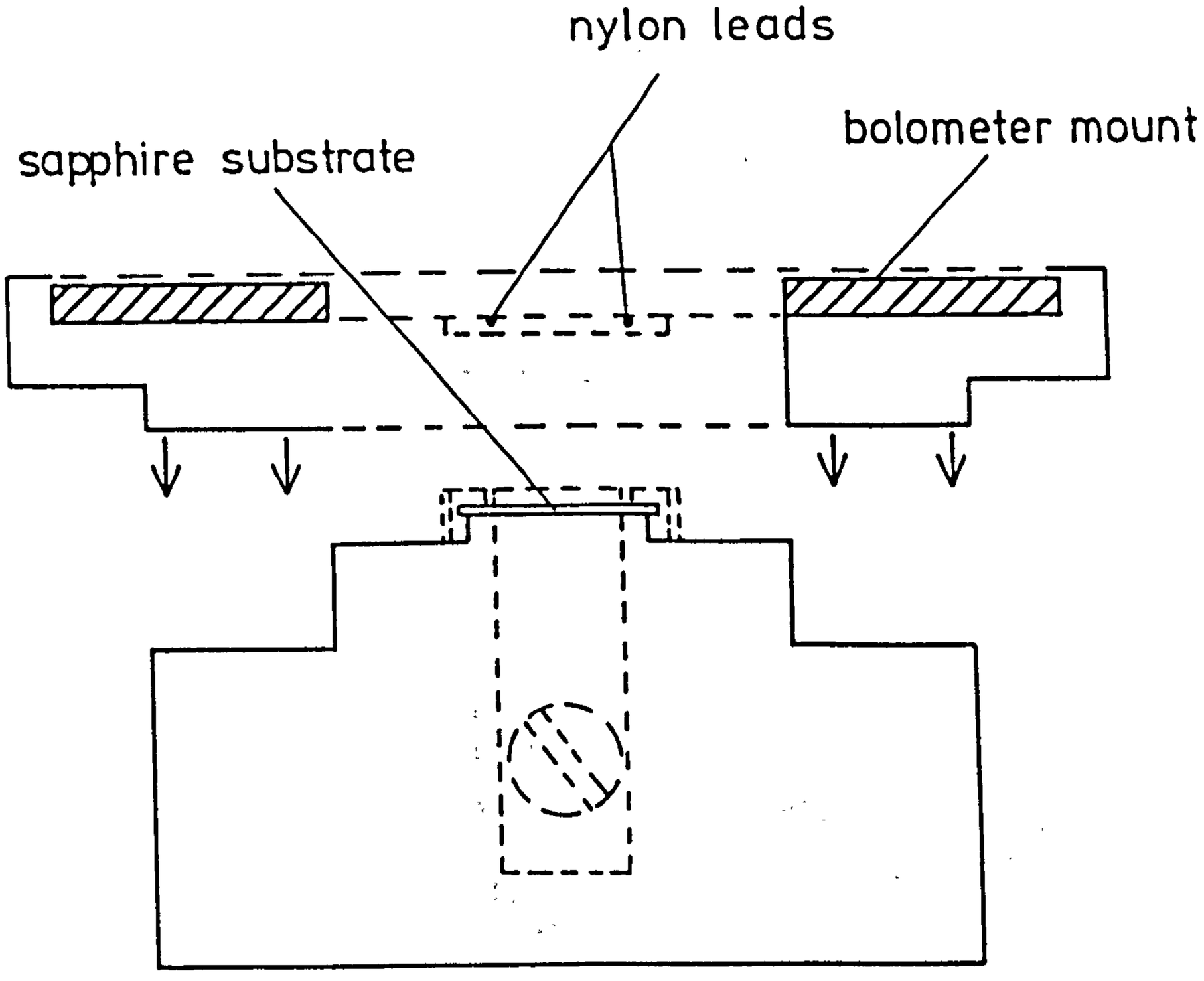

Figure 11. Method used to lower nylon leads onto substrate for cold-welding.

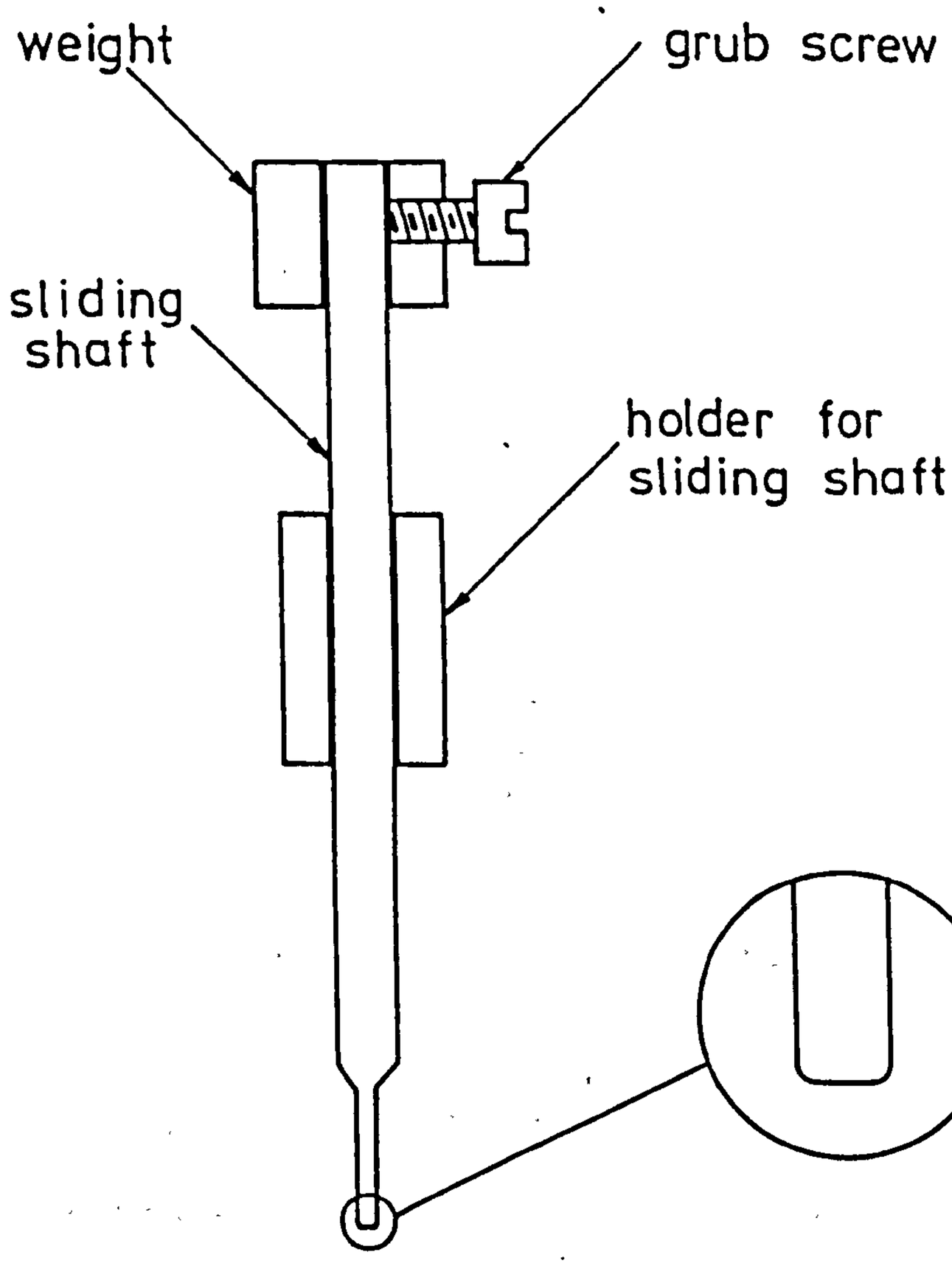

Figure 12. Tool used for cold-welding.

the sliding shaft was mounted on a micro-manipulator. To produce the cold-weld, the tip of the cold-welding tool was moved into position using the micro-manipulator just above an area on one of the nylon leads where a contact was to be made. The micro-manipulator was then steadily lowered a few millimetres beyond the point where the tip of the tool was actually in contact with the lead. At this point, therefore, the weight of the tool was entirely supported by the lead and this pressure caused a fusion between the thick In films on the substrate and lead thereby forming an electrical and mechanical contact. The weight of the sliding part of the tool could be changed by using different detachable weights (see Figure 12). The total weight actually used was 16 grms. The micro-manipulator was then raised and the same process repeated for the other three contacts.

The next step was to glue the contacts with G.E. 7031 varnish. It was important to make sure that the amount of varnish deposited on the substrate was as small as possible to avoid significantly raising the thermal capacity of the element. The varnish used for the glueing was heavily diluted with a 50% solution of toluene and alcohol until it was a pale yellow colour. A very fine brush, made by cutting off all but a dozen or so bristles of a small brush, was used to deposit the diluted G.E. varnish solution on the substrate. Care had to be taken not to damage the cold-welds while doing this and the following technique was used:

The brush was dipped in the diluted varnish and then held just above a cold-welded contact. The tip of the brush was then dabbed onto the substrate just next to the contact. The varnish flowed underneath the lead along the entire length in contact with the substrate in the manner shown in Figure 13. When dry the thickness of the G.E. varnish

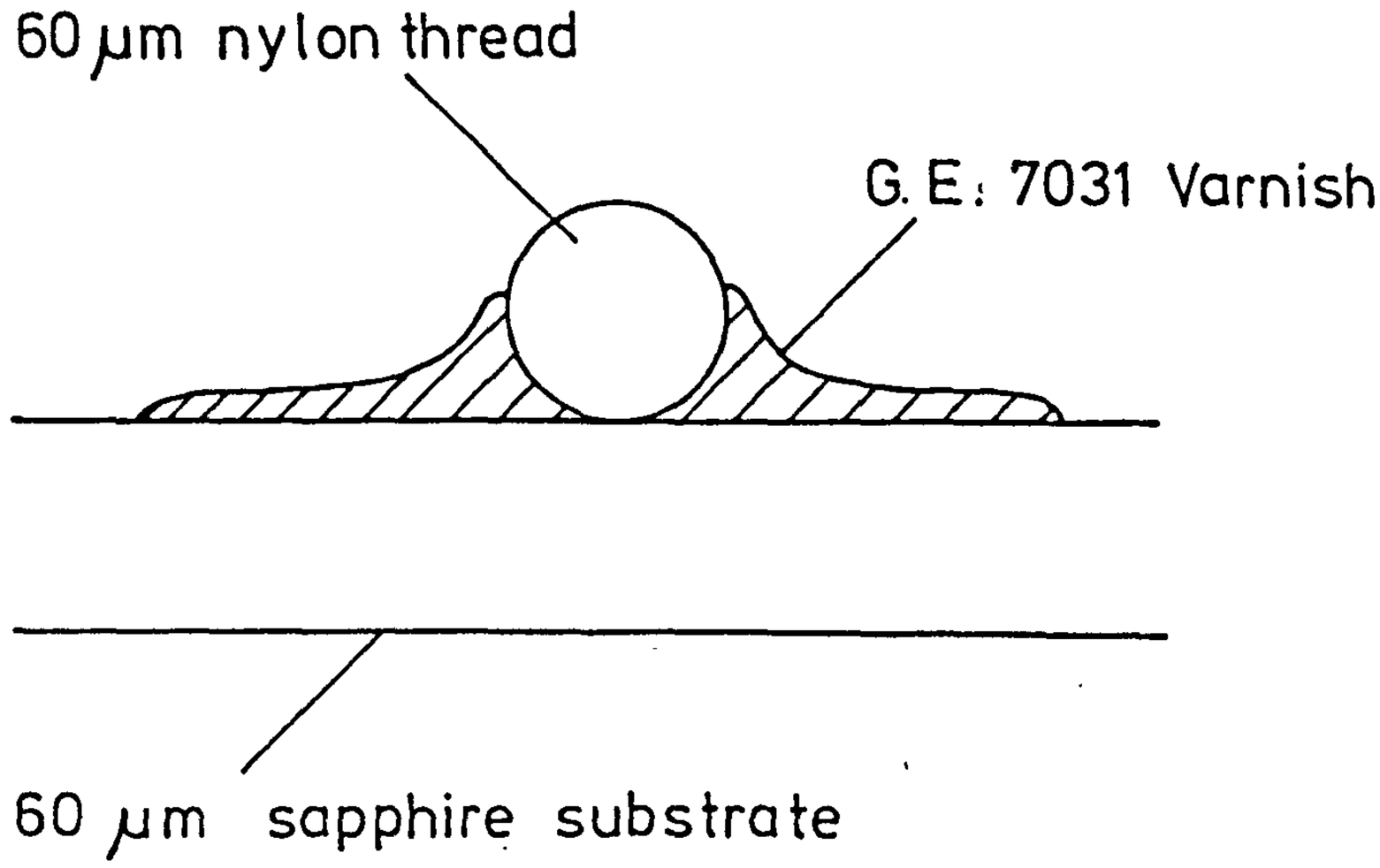

Figure 13. Cross-section through bolometer showing how the G.E. 7031 varnish collects around the area of contact between a nylon lead and the sapphire substrate.

was estimated to be 5 - 10 μm. Using this method, then, two contacts were glued at the same time. The brush was then cleaned in a 50% toluene/alcohol solution and the procedure repeated for the other pair of contacts.

After a few minutes when the varnish had dried, it was necessary to loosen and move the substrate clamps away before the bolometer element could be moved. To make sure that the bolometer contacts were not stressed while loosening the clamps, the following procedure was adopted:

Clamp 3 (as shown in Figure 9) was pushed aside using the cold-welding tool (still mounted in the micro-manipulator) before unscrewing. Then clamps 1 and 2 were unscrewed and also pushed aside with the cold-welding tool. The mount holder could then be lifted off the substrate locating jig without damaging the contacts. The element was now ready to have the Bi absorber deposited on the uncoated surface of the substrate. The required film impedance of ≃ 80Ω/square at room temperature was obtained by monitoring the impedance across a glass test slide mounted next to the jig during the evaporation.

The final stage in the construction of the bolometer was to attach four lead-out wires to the bolometer mount. The lead-out wires were 25 mm long, 40 s.w.g. enamelled copper wire with ≃ 2 mm of enamel bared from each end. The electrical connection between the bared ends of the leads and the evaporated film on the nylon leads was made using R.S. electrically conductive paint applied with a fine brush. Extra mechanical strength was obtained by also glueing the wires down with G.E. varnish. The electrically conductive paint and G.E. varnish had to be allowed to dry for about half an hour before the element could be stored in a vacuum to prevent bubbling. It should also be noted that

the lead-out wires had to be positioned and the paint and varnish applied so that they fitted into the 8 mm slot on the fitting used to hold the bolometer mount while performing ^{4}He tests.